EUROPEAN ORGANIZATION FOR NUCLEAR RESEARCH

March 29, 2018

Letter of Intent: Fixed-Target Experiment at M2 Beamline beyond 2020

Contents

1 Executive Summary

2 Introduction

We present for your consideration the Letter of Intent (LoI) for CERN SPS-based universal QCD facility by using which different research programs in QCD will be carried out.

We underline that we will discuss in the LoI a number of experiments (or research programs) which will share the experimental hall EHN2, SPS M2 extracted beam line and some general-purpose parts of a universal spectrometer which will be constructed in EHN2 area.

The uniqueness of this QCD facility is granted by the unique parameters of the secondary SPS beams (muons, hadrons, electrons) produced in the collision of the primary SPS beam (450 GeV protons) with secondary beam production target.

Secondary muon and hadron beams existing already now would allow to run unique experiments dedicated to the:

- measurement of the proton radius in μ-scattering experiment;
- study of 3-dimensional proton structure study via Deep Virtual Compton Scattering (DVCS) process;
- study light meson structure study using Drell-Yan process;
- search for heavy XYZ exotic states produced in proton-antiproton collisions;
- measurement of the absolute cross section of various anti-particle production in proton He^3 interactions.

Even wider opportunities would be open once the Radio-Frequency (RF) separated high intensity and high energy kaon and antiproton beam will became available. Such a beam would allow to perform:

- high statistics study of strange meson sector using kaon beam diffractive scattering on a liquid hydrogen target;
- unique measurements of kaon structure using Drell-Yan process and Direct Photon Production (DPP);
- model independent access to 3-dimensional structure of nucleon (TMDs);
- high precision measurement of kaon polarisability.

This LoI structured in the following way:

- it is opened with executive summary;
- after short Introduction Physics Case is discussed experiment by experiment;
- first block of experiments can be carried out with currently available M2 secondary beams;
- second block of experiments require newly designed RF-separated kaon and antiproton beam;
- the last part of the LoI is dedicated to the Instrumentation, i.e. it contain the list of upgrades which; has to be performed on order to fulfil experimental requirements for all discussed measurements.

3 Hadron Physics with Standard Muon Beams

3.1 Proton radius measurement using $\mu - p$ elastic scattering

The physics of the proton as the charged nuclear building block of matter is at the core of interest in the quest for understanding nature. As consequence of its inner structure, the electromagnetic form factors G_E and G_M encode the response of the proton to outer electric and magnetic fields, respectively. As worked out in the following chapter, the squares G_E^2 and G_M^2 can be measured in non-polarized elastic lepton scattering off the proton, which has been done extensively since the 1950's with the pioneering work of R. Hofstadter [7]. The gross feature of the form factors is a dependence on the squared momentum transfer Q^2 given by

$$G_E(Q^2) = G_M(Q^2)/\mu_p = \frac{1}{(1+Q^2/a^2)^2} \tag{1}$$

called the dipole approximation, which can be motivated by a substructure of the proton consisting of three constituent quarks. The constant a has been determined in electron scattering to be about $a^2 \approx 0.71\,\mathrm{GeV}^2/c^2$. The functional behavior with $a^2 = 0.71\,\mathrm{GeV}^2/c^2$ is used as the standard reference dipole form $G_D(Q^2)$.

The respective charge and magnetic moment distributions in space are obtained by Fourier transformation of the form factors, and specifically the electric mean-square charge radius is related to form factor by

$$\langle r_E^2 \rangle = -6\hbar^2 \left. \frac{dG_E(Q^2)}{dQ^2} \right|_{Q^2 \to 0} \overset{dipole}{=} \frac{12}{a^2} \approx (0.81\mathrm{fm})^2 \tag{2}$$

More refined fits to the measured shape of the form factors are often given as polynomials or other analytic functions of Q^2 multiplying the dipole approximation of 1. The so far most elaborate measurement of the proton form factors by elastic electron scattering have been carried out at the Mainz university accelerator MAMI [8, 9], and a parameterization of the results at small values $Q^2 < 0.2\,\mathrm{GeV}^2/c^2$ is shown in the upper plot of Fig. 1. Compared to earlier electron scattering data, the G_M^2 shows a positive deviation with respect to G_D^2, while G_E^2 starts with a steeper slope, corresponding to a charge radius, with the systematic uncertainties summed up linearly, $r_E^{rms} = \sqrt{\langle r_E^2 \rangle} = (0.879 \pm 0.011)\,\mathrm{fm}$. It is at variance with the value found in laser spectroscopy of muonic hydrogen, which is a different way to measure the proton radius. The result is $r_{E,\mu H}^{rms} = (0.841 \pm 0.001)\,\mathrm{fm}$ [10, 11], and this discrepancy of more than three standard deviations triggered many efforts to clarify its origin [12–18].

3.1.1 Experiments targeting the proton radius puzzle: the M2 beamline case

It is suggested here to measure **elastic muon-proton scattering** with a high-energetic muon beam on a hydrogen gas target over a momentum transfer range particularly sensitive to the proton charge radius. This means, on the one hand, to measure the cross-section to come as close as possible to $Q^2 = 0$ as required by 2, and on the other hand, to cover a sufficient range in momentum transfer in order to constrain the slope of the cross-section on the desired level of precision. As illustrated in Fig. 1, this range is approximately $0.001 < Q^2/(\mathrm{GeV}^2/c^2) < 0.02$: At smaller values of Q^2, the deviation from a point-like proton is on the 10^{-3} level and thus smaller than unavoidable systematic effects, as the variation of the detector efficiencies with Q^2 that cannot be controlled more accurately with the currently available methods. At higher $Q^2 > 0.02\,\mathrm{GeV}^2/c^2$, the non-linearity of the Q^2 dependence becomes the predominant source of uncertainty, and cannot be used to determine the proton radius, unless more elaborate theory input is assumed.

For reaching the required precision at small momentum transfers, it is relevant to observe the recoil protons. Due to their small energy, this implies the target to be the detector volume at the same time. This can be realized by a Time Projection Chamber (TPC) operated with pure hydrogen gas. Such a

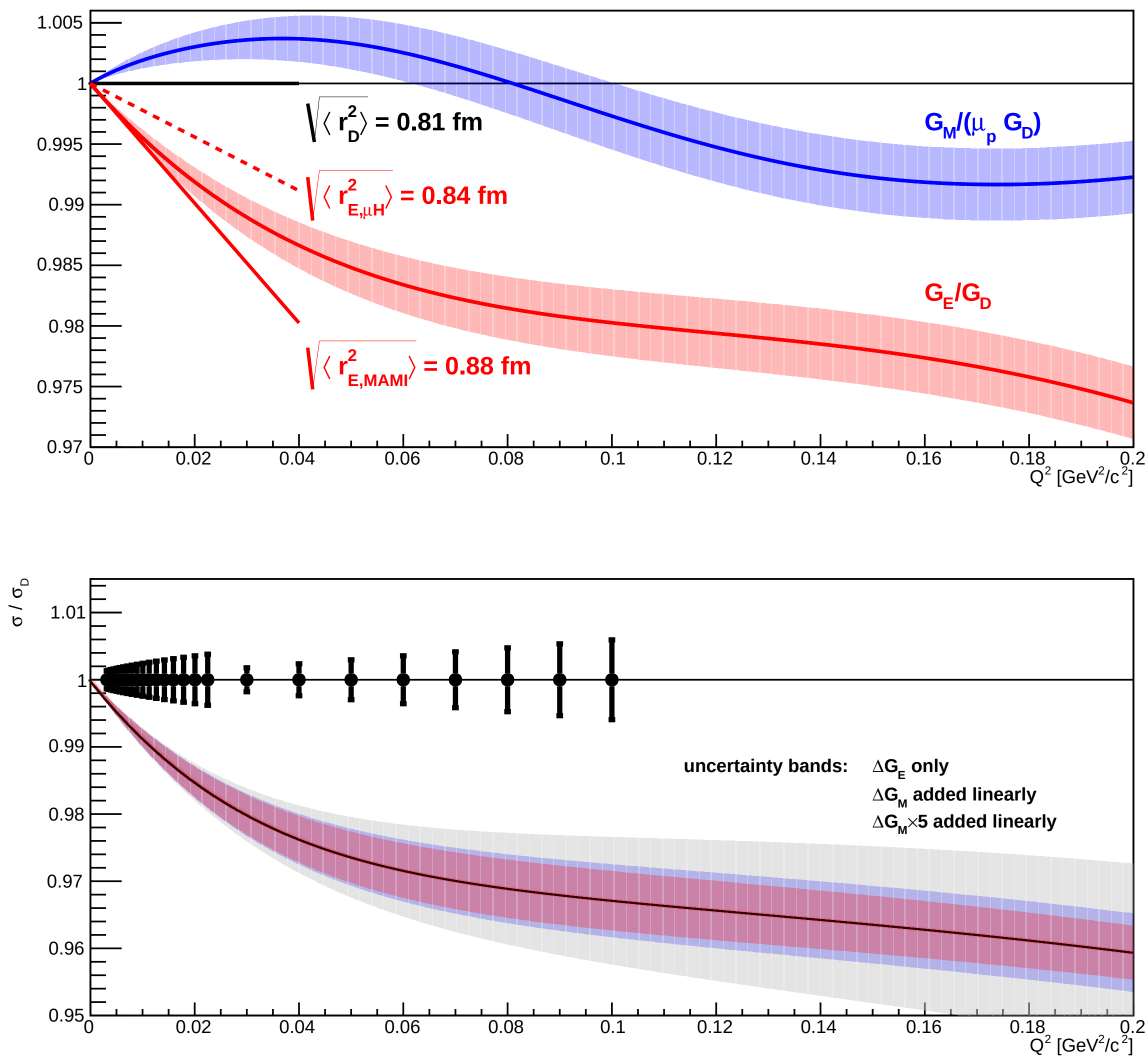

Figure 1: Upper plot: proton form factors G_E and G_M as measured at MAMI, presented relative to the dipole form G_D as given in the text. Lower plot: corresponding cross-section behavior, relative to the standard dipole form. The innermost uncertainty band corresponds to the effect of the uncertainty of G_E only, while for the (blue) middle band the uncertainty from G_M has been added linearly, and for the outer (gray) band the contribution from ΔG_M has been increased by a factor of five. The dots with error bars, arbitarily placed at 1, represent the achievable statistical precision of the proposed measurement, down to Q^2=0.003 GeV$^2/c^2$, where the statistical uncertainties are expected to dominate the systematic point-to-point uncertainty. There will be data from the proposed experiment down to $Q^2 \leq 0.001$, with the statistical uncertainty further shrinking according to the increasing cross-section with $Q^2 \rightarrow 0$, *cf.* Eq. 3, which are omitted here for conciseness. For a discussion of the uncertainty contributions at different Q^2 regions, see the text.

target has been developed by PNPI [19, 20] and is in the testing phase for an analogous experiment using electron scattering at Mainz.

Several experiments are currently ongoing or proposed for refining the knowledge on **electron-proton** elastic scattering [12, 13, 21, 22]. This includes the mentioned TPC experiment at MAMI [21], but also the inital-state radiation experiment of the A1 collaboration [22]. All experiments of electron scattering are challenged by the required QED radiative corrections, which are as large as 20% due to the small electron mass. Currently, it is unclear how the precision of those corrections can be controlled on the desired below-1% level. Hence, independent of the outcome of any measurements done with electrons, those with muons will test systematic effects related to radiative corrections, since they are substantially smaller for muons due to their much larger mass.

Despite this obvious benefit, there are still significant systematic effects expected for measurements for **muon-proton** elastic scattering at **low muon beam energies**, *e.g.* discussed for the proposed MUSE experiment [16]. Apart from corrections for the pion component in the beam and muon decays, there is a substantial correction for the Coulomb distortion of the low-velocity muon wave function. The latter is estimated to be on the level of one percent for larger scattering angles, however with an unclear relation to the other radiative corrections, which introduces a systematic uncertainty for which an experimental test is most convincing. Such a test is best realized with scattering at very high energies, where the Feshbach correction reduces to a negligible level.

The highest precision on the proton radius is claimed by the the investigation of atomic level splittings [10, 11, 14, 15] that are very accurately measured by laser spectroscopy. From 1S transitions in **muonic hydrogen**, the above-mentioned value 0.841 fm has been determined, by correcting the measured frequency for all known QED effects and attributing the remaining effect to the proton finite size. By starting with the measurement of the single number, this approach is clearly less detailed than a measurement of the form factor behaviour over an extended range in Q^2, which allows for checking *e.g.* the assumption made for the linear behaviour of the form factor in the studied Q^2 range.

In summary, the proposed muon-proton scattering using a high-energy muon beam for the determination of the proton radius we regard as an important and unique cornerstone in the quest for solving the proton radius puzzle. It is seen very timely in view of the highly competitive and dynamic ongoing research in the field, to realize the measurement at the CERN M2 beamline as soon as the scheduling and the required preparatory steps will allow.

3.1.2 Elastic lepton-proton scattering

The cross-section for elastic muon-proton scattering to first order is

$$\frac{d\sigma}{dQ^2} = \frac{\pi\alpha^2}{Q^4 m_p^2 \vec{p}_\mu^{\,2}} \cdot \left[\left(G_E^2 + \tau G_M^2\right) \frac{4E_\mu^2 m_p^2 - Q^2(s - m_\mu^2)}{1+\tau} - G_M^2 \frac{2m_\mu^2 Q^2 - Q^4}{2} \right] \tag{3}$$

where $Q^2 = -t = -(p_\mu - p_{\mu'})^2$, $\tau = Q^2/(4m_p^2)$ and $s = (p_\mu + p_p)^2$. The squared centre-of-momentum energy s is given, in the laboratory system, by $s = 2E_\mu m_p + m_p^2 + m_\mu^2$ with E_μ the energy, and $\vec{p}_\mu$ the three-momentum of the incoming muon colliding with a proton at rest.

The different dependence on the beam energy E_μ of the two terms in 3 that are proportional to G_M^2 allows, in principle, for the "Rosenbluth separation" of the two form factor contributions G_E^2 and G_M^2, by measuring the cross-section at constant Q^2 and, at least, two different beam energies (or correspondingly at different muon scattering angles). For small $Q^2 < m_\mu^2$, the relative contribution of the second term is approximately m_μ^2/E_μ^2, and for beam energies $E_\mu > 50\,\text{GeV}$ it is an effect of less than 10^{-5}, which is unmeasurably small and thus can be neglected.

Consequently, with the proposed high-energy muon beam, one effectively determines the combination $(G_E + \tau G_M)$, and at small Q^2 (*i.e.* small τ) this amounts to a measurement of G_E when the small expected contribution from G_M is corrected for. Even with a conservative estimate of the uncertainty from G_M, a factor of five larger than the one claimed in the MAMI analysis, the uncertainty on G_E and thus on the charge radius stay well below 0.1%, which is about a factor of 10 smaller than the precision of 1% that the measurement aims at.

3.1.3 Measurement at CERN M2 beamline

We propose to measure elastic muon-proton scattering employing a 100 GeV muon beam on a pressurized hydrogen gas target. For the core of the measurement aiming at a precise measurement of the proton radius, the relevant momentum transfers $0.001 < Q^2/(\mathrm{GeV}^2/c^2) < 0.02$ are measured by operating the target as a TPC for detecting the proton recoil tracks. The pressure of the gas is optimized for having on the one hand sufficiently low stopping power such that the proton recoil tracks are detectable, and on the other hand they still fit in the TPC volume. The pressure ranges from 4 to 20 bar. The respective gas system has been developed and is in the test phase at MAMI. The details of the readout are to be adapted to the COMPASS environment and are currently under study. For higher recoil energies and thus the possibility to access a broader range of the form factor evolution in Q^2 a similar hydrogen cell is envisaged, with a cylindric array of scintillating fiber (SciFi) rings surrounding the interaction region.

The muon scattering kinematics are measured with the COMPASS spectrometer in its standard muon setup. To allow for the detection of the elastic, *i.e.* almost unscattered, tracks the beam killer components are excluded from the trigger. The central parts of the tracking detectors are activated, and the silicon telescopes surrounding the TPC are used for measuring with high accuracy the muon scattering angle. In addition, the electromagnetic calorimeters serve to control the (rare) radiative events.

Since triggering solely on the proton recoil implies Q^2-dependent efficiency variations that cannot be controlled from the data themselves, a trigger component from the muon trajectory is foreseen. The beam rate is too high to record all events. Therefore, the beam trigger is extended by a new component that allows to veto muons with a scattering angle below about 5 μrad. This suppresses muons that have experienced multiple (small-angle) scattering only, which amounts to 99% of the incoming muons. In contrast muons are efficiently selected with a scattering angle in the target larger than 100μrad, corresponding to momentum transfers larger than $10^{-4}\,\mathrm{GeV}^2/c^2$. A scenario could be realized with SciFi components sandwiching the silicon detectors, however solutions with thinner detectors, such as silicon pixel detectors with a readout sufficiently fast for the trigger would be desirable for minimizing the multiple scattering as a source of systematic uncertainty. The respective topological trigger component is referred to as "kink trigger". For the longer-range future, a triggerless readout is aimed for (Sec. 6.1.1), which can solve current issues of rate capability and allows for realizing the described event selection in an elegant and efficient manner for the proposed measurement. Regarding the higher-Q^2 region, the full beam rate has to be used, in order to compensate for the $1/Q^4$ behaviour of the Mott cross-section.

The statistical uncertainties that can be achieved in the sketched experiment are shown in Fig. 1 in a suitable segmentation of the data in Q^2 bins. The data set is sufficient to constrain the proton radius to better than 0.01 fm precision.

The experimental set-up uses the standard muon beam set-up of COMPASS but the target region will be modified as to accommodate an active hydrogen target, possibly an active SciFi target, and two silicon telescopes. Proton recoil measurement, muon measurement, and the trigger of this experiment are detailed in Sec. 6.2.2.

3.2 Exclusive reactions with muon beams and transversely polarized target

3.2.1 Motivations for the GPD E measurement

One of the major goals of the forthcoming worldwide GPD physics programs will be the precise mapping of the GPDs H and E, which enter in the "Ji sum rule" and provide access to the total parton angular momentum:

$$J^f(Q^2) \;=\; \frac{1}{2}\lim_{t\to 0}\int_{-1}^{1} dx\, x\left[H^f(x,\xi,t)+E^f(x,\xi,t)\right], \tag{4}$$

where

$$\frac{1}{2} \;=\; \sum_{q=u,d,s} J^q(Q^2) \;+\; J^g(Q^2). \tag{5}$$

While some information on the GPD H is already provided by the existing data, the GPD E is basically unknown. The most promising DVCS observables that are sensitive to E are the transverse target spin asymmetry in the case of proton targets, and the longitudinal beam spin asymmetry with neutron targets. Such measurements are currently either planned or being performed at Jlab, and represent a flagship goal of the Jlab physics program after the 12 GeV upgrade of the accelerator complex.

The Compass experiment is currently undertaking a measurement of exclusive photon and meson production with unpolarized proton targets and high-energy polarized muon beams, mainly covering the kinematic domain of sea quarks and complementing the measurements at larger x_B performed or planned at lower energies. In this configuration, Compass is mostly sensitive to the GPD H, and will provide a separate measurement of the real and imaginary parts of the $\mathscr{H}$ CFF by combining cross-sections measured with beams of opposite charge and polarization.

By employing a transversely polarized proton target, COMPASS has the possibility to access the GPD E through the measurement of the transverse target spin dependent DVCS cross-sections. Such a measurement would be complementary to the CLAS12 data, and would provide a crucial extension of the kinematical coverage to the small x_B domain (**how can we show that this is crucial?**).

3.2.2 Worldwide Competition

The wealth of new accurate measurements that will become available in the next decade will provide the experimental ground for validating and improving GPD models through global fits, possibly beyond the leading approximations and including higher twist and higher order contributions, which seem to be needed to describe the existing data [**?**].

The recent 12 GeV energy upgrade of the CEBAF accelerator at Jefferson Lab [1] will allow high-precision measurement of observables related to the partonic structure of nucleons in the valence quark domain, significantly extending the kinematic coverage of previous measurements at lower energies. The high luminosity, high-precision measurements performed in Hall A [**?**] and C [**?**] will be complemented by the large acceptance of the CLAS12 [**? ? ? ? ? ?**] experiment in Hall B. In the longer term, the Electron-Ion Collider [**?**] will further extend the kinematic coverage to the gluon sector and provide polarized data of unprecedented precision for GPD and TMD studies. The kinematic domain covered by past, running and planned DVCS experiments is summarized in fig. 2.

3.2.3 Theoretical predictions for COMPASS

Since at COMPASS both beam and target are polarized, the relevant observables for accessing the GPD E are represented by the transverse beam charge & spin difference and sum of the $\mu p^{\uparrow} \to \mu\gamma p$ cross-section, respectively defined as follows:

$$\mathscr{D}_{CS,T} \equiv \Big(d\sigma^{\overset{+}{\leftarrow}}(\phi,\phi_S) - d\sigma^{\overset{+}{\leftarrow}}(\phi,\phi_S+\pi)\Big) - \Big(d\sigma^{\overset{-}{\rightarrow}}(\phi,\phi_S) - d\sigma^{\overset{-}{\rightarrow}}(\phi,\phi_S+\pi)\Big), \tag{6}$$

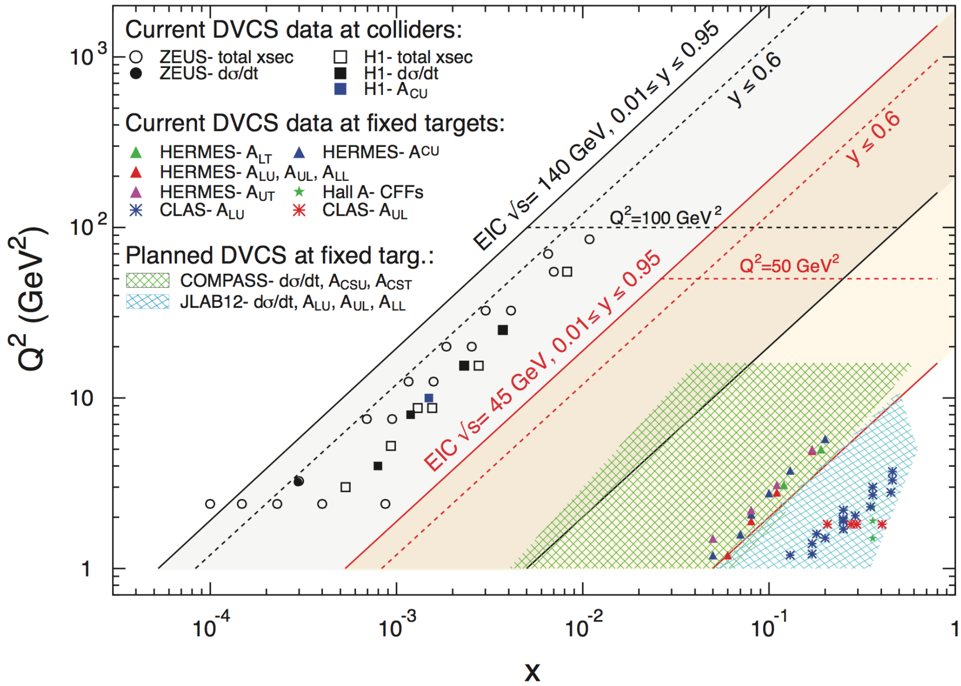

Figure 2: Overview of the existing and planned measurements of DVCS in both fixed-target and collider mode.

$$\mathscr{S}_{CS,T} \equiv \left(d\sigma^{\overset{+}{\leftarrow}}(\phi,\phi_S) - d\sigma^{\overset{+}{\leftarrow}}(\phi,\phi_S+\pi)\right) + \left(d\sigma^{\overset{-}{\rightarrow}}(\phi,\phi_S) - d\sigma^{\overset{-}{\rightarrow}}(\phi,\phi_S+\pi)\right). \tag{7}$$

Two experimental asymmetries can also be derived from these expressions:

$$\mathscr{A}^D_{CS,T} = \frac{\mathscr{D}_{CS,T}}{\Sigma_{unpol}} \text{ and } \mathscr{A}^S_{CS,T} = \frac{\mathscr{S}_{CS,T}}{\Sigma_{unpol}}, \tag{8}$$

where Σ_{unpol} represents the lepton-charge-average unpolarized cross section.

The quantities between parenthesis represent the differences of cross sections with the two opposite target spin orientations (denoted by ϕ_S and $\phi_S + \pi$, see fig. 3). The difference and sum of cross-sections defined above can be decomposed in angular harmonics of the type $[\sin(\phi-\phi_S)\sin(n\phi)]$, $[\sin(\phi-\phi_S)\cos(n\phi)]$, $[\cos(\phi-\phi_S)\sin(n\phi)]$ and
$[\cos(\phi-\phi_S)\cos(n\phi)]$, whose coefficients are expressed as linear or bi-linear combinations of $\mathscr{H}$, $\widetilde{\mathscr{H}}$ and $\mathscr{E}$ CFFs. As an example, the leading twist-2 coefficient in $\mathscr{D}_{CS,T}$ is associated to the $[\sin(\phi-\phi_S)\cos(\phi)]$ modulation in the interference term, and receives contributions from the imaginary parts of $\mathscr{H}$ and $\mathscr{E}$ at the same level [2]:

$$c^I_{1T_-} \propto \frac{t}{4M^2}\mathrm{Im}\left[(2-x_B)F_1\mathscr{E} - 4\frac{1-x_B}{2-x_B}F_2\mathscr{H}\right]. \tag{9}$$

The various coefficients can be extracted from a Fourier analysis of the measured cross-sections or asymmetries. The size of the asymmetry associated to the $c^I_{1T_-}$ term has been recently estimated by P. Sznajder in the context of the PARTONS framework [**?**], comparing the VGG [3] and GK [4] model predictions as function of x_B, Q^2 and $-t$ in the typical kinematic domain of COMPASS. As shown in fig. 4, the expected asymmetries are sizable and, in the case of the GK model, show a clear sensitivity to the contribution of the GPD E.

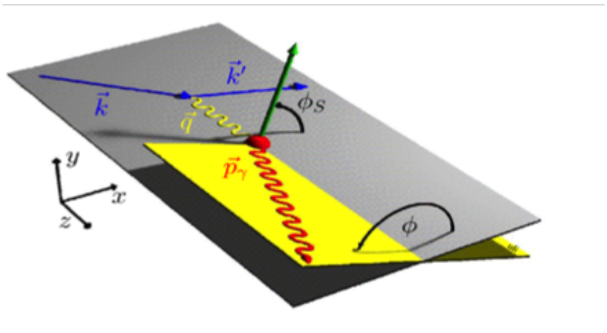

Figure 3: Definition of the relevant angles in the DVCS on a transversely polarized target.

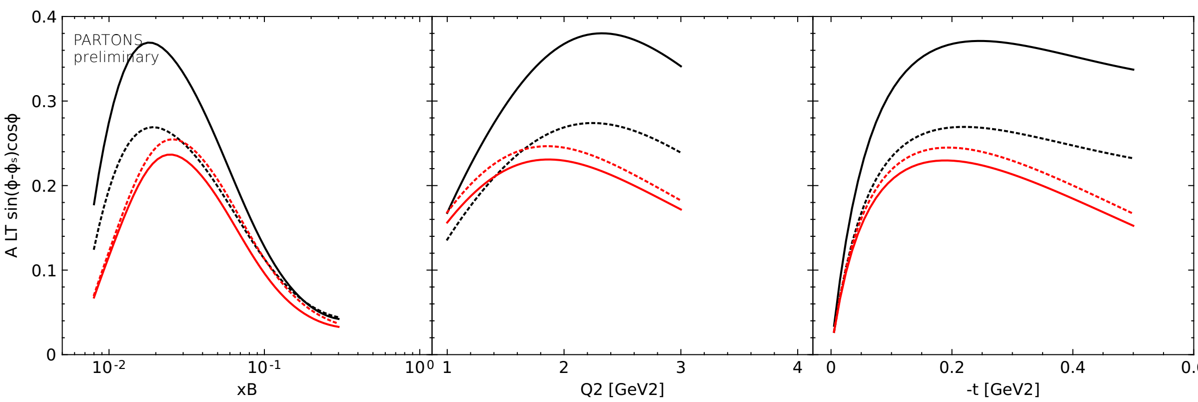

Figure 4: Estimation of the amplitude of the $[\sin(\phi-\phi_S)\cos(\phi)]$ modulation in the COMPASS kinematics, based on predictions from the VGG [3] (red) and GK [4] (black) models at leading order (solid lines) and with the additional assumption of $E=0$ (dashed lines). The estimates have been obtained in the context of the PARTONS [**?**] framework.

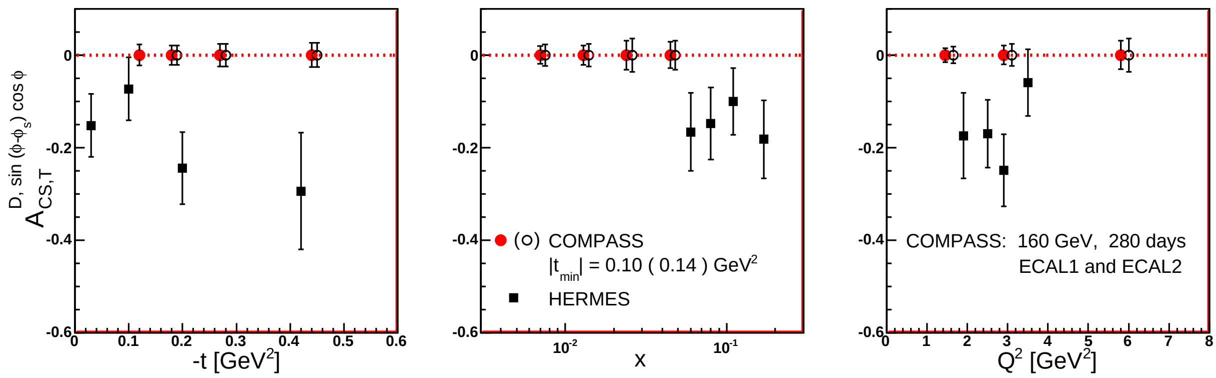

Figure 5: Expected statistical accuracy of $A_{CS,T}^{D,\sin(\phi-\phi_s)\cos\phi}$ as a function of $-t$, x_B and Q^2 from a measurement in 140 days with the COMPASS spectrometer, using a 160 GeV muon beam and a transversely polarized NH_3 target. Solid and open circles correspond to a minimum detectable $|t|$ of 0.10 GeV^2 and 0.14 GeV^2, respectively. Also shown is the asymmetry $A_{U,T}^{\sin(\phi-\phi_s)\cos\phi}$ measured at HERMES [5] with its statistical errors. Figure from ref. [6].

3.2.4 Projections and Accuracy for COMPASS

The expected statistical accuracy for a COMPASS measurement of the $[\sin(\phi-\phi_S)\cos(\phi)]$ modulation using a transversely polarized NH_3 target is shown in fig. 5. The red points and the open circles in the plots represent the projections for a measurement in 140 days at the nominal muon beams intensity, and for a minimum detectable $|t|$ of 0.10 GeV^2 and 0.14 GeV^2, respectively. For comparison, the black squares show the asymmetry $A_{U,T}^{\sin(\phi-\phi_s)\cos\phi}$ measured at HERMES [5] with its statistical errors. The COMPASS data could therefore provide a measurement of the $[\sin(\phi-\phi_S)\cos(\phi)]$ modulation with a statistical accuracy of approximately 2.5% in the so far uncharted region of $5\cdot 10^{-3} \lesssim x_B \lesssim 5\cdot 10^{-2}$.

The technical realisation of detecting recoil particles with polarized solid-state targets is detailed in Section 6.2.3.

4 Hadron Physics with Standard Hadron Beams

4.1 DY and charmonium production with conventional hadron beams

4.1.1 Introduction: Meson Structure and the Origin of Nuclear Mass

The quark-gluon structure of light mesons and the physical origin of their small masses remains largely unknown. Strong interaction dynamics generate a striking mass difference between heavy 3-quark nucleon bound states and light 2-quark pion bound states. Pion-mediated Yukawa interactions bind nucleons to nuclei and the resulting large nuclear masses govern the gravitational forces that have formed our solar system. While there are ample data available on the proton, the experimental determination of meson structure remains the long-awaited and critical input to theoretical efforts that seek to explain the emergence of massive composite hadrons, including the large mass difference between pions and protons.

Two Standard Model mechanisms contribute to the generation of mass. Spontaneous electroweak symmetry breaking gives rise to the Higgs mechanism providing fundamental particles with their current masses. For example, the masses of the up and down quarks are 2.2 MeV and 4.7 MeV respectively. Second, strong-interaction chiral symmetry breaking leads to the large masses of composite light-quark states. For the proton, the sum of the current quark masses from the Higgs mechanism is about $m_{uud} = 9\,\mathrm{MeV}$ while the observed proton mass is 100 times larger, $m_p = 938\,\mathrm{MeV}$. For the pion the current quark mass is $m_{ud} = 7\,\mathrm{MeV}$, while measurements yield a physical mass of $m_\pi = 139.6\,\mathrm{MeV}$. Consequently, present quark models do not allow a consistent description of the pion and proton bound masses: the mass of a constituent quark in the proton will be about 300 MeV compared to 70 MeV for the pion.

In chiral QCD with massless quarks, hadron masses in the Lagrangian emerge through the trace anomaly of the energy momentum tensor. For the proton, the binding energy and the mass of dressed quarks add to about $m_p = 1\,\mathrm{GeV}$. Very differently for the pion, the Goldstone Boson of the interaction, the binding energy and the dressed quark mass cancel to $m_\pi = 0\,\mathrm{GeV}$ [24]. In lattice QCD, Large Momentum Effective Theory (LaMET) [25] will make it possible to calculate hadron quark and gluon distribution functions quantitatively, see for example [26] and [27]. Such calculations greatly benefit from the arrival of Peta-scale supercomputers. Recently, there has been increasing interest in theoretical calculations of meson parton structure, including the Nambu-Jona-Lasinio model [28, 29], the chiral constituent quark model[30], the light-front constituent model[31], and from QCD Dyson-Schwinger equations[32, 33].

Detailed experimental information for the proton quark and gluon structure is available from the analysis of numerous lepton-nucleon deep inelastic scattering experiments combined with several data sets of jet, hadron, and Drell-Yan cross sections observed in proton-proton and proton-anti-proton collider experiments over a broad range of the scattering kinematics. Global analyses have been carried out using NNLO in perturbative QCD and have resulted in precise knowledge of quark and gluon distribution functions of the proton.

In contrast, the quark and gluon structure of mesons is only poorly constrained from early Drell-Yan cross section measurements for pions [34, 35][36, 37] [38, 39] and completely unconstrained for kaons [40]. The sparse experimental information on meson structure limits the ability to test theoretical progress directed at determining quark and gluon distributions from ab initio lattice-QCD. Further, it limits testing advances in understanding the dynamical generation of hadron masses in QCD. Important experimental activities are underway to study the pion structure through final state neutron-tagged DIS at Jefferson Laboratory. The feasibility of pion structure measurements at a future Electron-Ion Collider is being evaluated. But the need to relate the experimental neutron tagged DIS to the physics of DIS off-pions will translate into new theoretical model uncertainties that still need to be assessed.

The current high intensity pion-dominated hadron beam available from the M2 beamline at CERN provide a unique opportunity for measurements of pion and nucleon structure through pion induced Drell-

Yan on polarized and unpolarized proton, deuteron and nuclear targets. A significant improvement in the statistical precision can be achieved using modern analysis methods that access the Drell-Yan signal also at lower invariant masses. Compared to previous extractions of parton distributions, future analysis of Drell-Yan data will be based on the modern description of the Drell-Yan process at NNLO pQCD, reducing theoretical uncertainties. At a later stage, future RF separated kaon beams at CERN will lead to the first measurement of kaon structure, and RF separated antiproton beam will provide precision measurements on the spin dependent transverse momentum PDFs of the nucleon. These will be described in section 5.3.

In summary, in this section we propose a detailed study of the pion structure from additional data taking with the CERN M2 existing hadron beams. The following physics goals should be reached:

– determine pion valence and sea quark distributions;

– study charmonium production mechanism, in order to infer on the pion gluon distributions;

– study flavour-dependent nuclear effects.

The first two topics aim at a full, detailed picture of the pion structure, while in the last one we propose to contribute significantly to the precision of nuclear PDFs in the large x_2 region and check the flavour-(in)dependence of the EMC effect, mostly. In parallel, we propose to perform precise measurements of the Drell-Yan and J/ψ angular distributions produced from an isoscalar target, which shall complement those presently being performed at the COMPASS experiment with an ammonia target. As will be shown, these goals can be achieved simultaneously with two years of a dedicated run using both positive and negative pion-tagged beams of 190 GeV. A target system consisting of a long light isoscalar target followed by a shorter and heavier nuclear target is proposed.

4.1.2 Valence and sea separation in the pion

Pion induced Drell-Yan data were collected by experiments NA3[34], NA10 [35], WA39 [41] and now by COMPASS at CERN, and by experiment E615[36] at Fermilab. The experiments NA3 and WA39 studied pion induced Drell-Yan production for both beam charges. NA3 published an extraction of the pion distributions, based on their data alone. For different reasons none of these data sets have been included in the available extractions from global fits. Figure 6 shows the pion valence from two of the global analyses, SMRS [42] and GRV/S[43, 44]. These extractions rely on the π^- Drell-Yan data from E615 and NA10, and do not include uncertainty estimates. In the analysis of GRV/S the sea content is derived from momentum conservation, the gluon contribution being constrained by the direct photon measurements of WA70 [45] and NA24 [46]. Sutton et al.[42] provide their own parametrisation for the sea, considering three hypotheses for the amount of sea contribution (10%, 15% and 20%), which then also leads to three different results for the gluon contribution. The valence and sea distributions from NA3 are also shown, together with the respective error bands, propagated from their published fit coefficients and correlation matrix.

We propose to determine the shape of the sea quarks for x values larger than 0.1 and better constrain this contribution by collecting data with positive and negative pion beam on an isoscalar target, as proposed by [47]. Assuming charge conjugation, SU(2)$_f$ symmetry for valence quarks and SU(3)$_f$ symmetry for sea quarks, it is possible to build the two linear combinations 10 and 11:

$$\Sigma_{val}^{\pi D} = -\sigma^{\pi^+ D} + \sigma^{\pi^- D} \propto \frac{1}{3} u_v^\pi (u_v^p + d_v^p) \tag{10}$$

$$\Sigma_{sea}^{\pi D} = 4\sigma^{\pi^+ D} - \sigma^{\pi^- D} \tag{11}$$

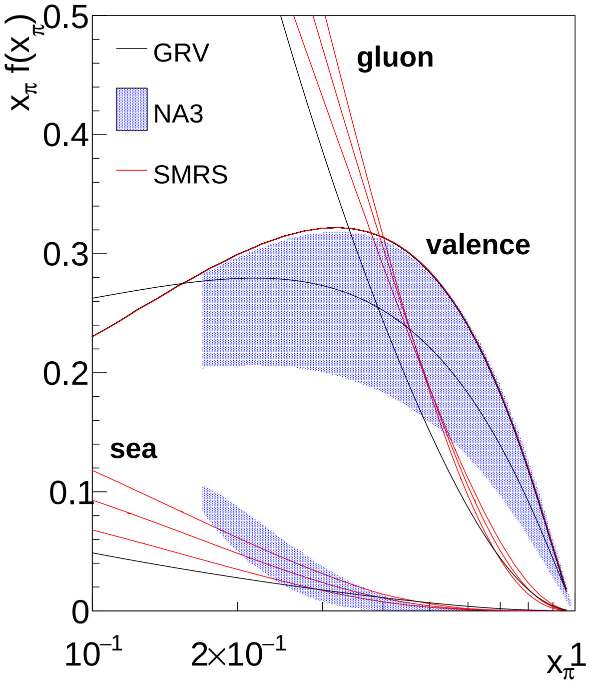

Figure 6: Pion distributions from global fits of SMRS and GRV/S, shown together with the NA3 extraction [34]. The three sea curves labelled SMRS correspond to three different hypotheses for the sea content. As a result, there are also three curves for the gluon contribution.

The first combination contains only valence-valence terms, while in the second no valence-valence term remains. Assuming small nuclear effects to this ratio, $\Sigma_{sea}/\Sigma_{val}$ can be computed for any of the measured x_N values. The use of a light isoscalar carbon target instead of the non-isoscalar platinum and tungsten targets used by NA3 and NA10 respectively, reduces nuclear effects.

Evaluating the ratio $\Sigma_{sea}/\Sigma_{val}$ requires precise cross-sections determination. We aim at an absolute cross-section determination at the level of 3% systematic error. A cross-check of the relative normalisation can be performed by comparing the J/ψ cross sections taken with the two beam charges. The cross-section ratio for π^- and π^+-induced J/ψ production on a Pt target was measured to be 1.016 ± 0.006) by NA3 [48].

The relative contribution of the sea quarks increases as x decreases. Therefore, a good separation with the valence quarks requires x values as low as possible, and incident pion momentum as high as possible. For a reasonable geometrical acceptance down to $x_F = -0.2$ and incident momentum of 190 GeV, values of $x_\pi = 0.10$ can be reached.

The negative hadron beam of 190 GeV momentum contains mainly pions, with a small contamination ($<$ 4%) from kaons and antiprotons, while the positive hadron beam contains $\approx$80% protons. The percentage of pions in the positive beam can be increased from 20% to $\approx$40%, by the use of a differential absorber, as was done in the past by the NA3 experiment. This option is being considered for the new experiment. A better shielding from environmental radiation would also allow to double the beam intensity, thus shortening the required data collection time. This possibility is also being studied.

Figure 7 left-top shows the achievable cross-sections accuracy of the proposed experiment, as simulated from Pythia at leading order, with a K-factor of $K = 2$ consistent with what was obtained by past experiments. Represented is the option of 255 days of π^+ beam data taking and 25 days with π^- beam of 190 GeV momentum on a carbon target of 4×25 cm. The difference in data collection time between the two beam polarities is explained by the Drell-Yan cross-section difference itself and by the positive versus negative hadron beams composition, that together lead to a share 10:1 of π^+ to π^- running time. Beam intensities of 7×10^7 particles per second (as used in COMPASS Drell-Yan data-taking), with two pulses of 4.8 s in each SPS super-cycle of 52 s are assumed. The fraction of pions in the positive hadron beam is 24%. CEDAR detectors provide beam particle identification with 90% efficiency. The product of other efficiencies, acceptance and livetime is estimated as 0.13 . The carbon target is followed by a tungsten target placed 40 cm downstream of it.

The right-hand side of Fig. 7 shows accuracy estimates of the pion $\Sigma_{sea}/\Sigma_{val}$ as a function of x_π, in three possible dimuon mass ranges. The top panel presents the background-free Drell-Yan mass range, while the two below use the assumption that machine learning techniques will succeed in isolating the Drell-Yan contribution from competing processes. The curves labelled SMRS represent three different contributions of the sea quarks to the pion momentum, ranging from 10% to 20%. Below $x_\pi = 0.5$ the ratio is strongly dependent on the amount of pion sea . This strong variation at low x shows that SMRS is unconstrained in this region, since no sea-sensitive data were included in the global fits. The top panel shows also the sea distribution extracted by NA3 based solely on their own data together with its uncertainty band.

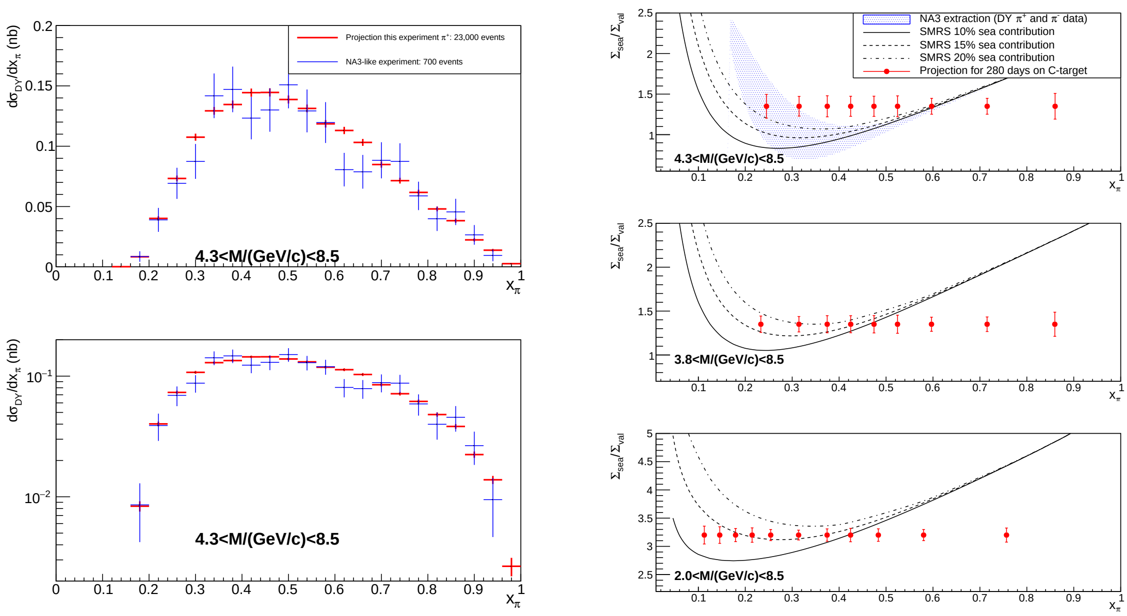

Figure 7: a) Drell-Yan cross-section as a function of x_π, with the expected statistical accuracy from the proposed experiment using a carbon target with the π^+ beam. The accuracy of an NA3-like experiment is also shown for comparison. b) Σ_s/Σ_v as a function of x_π: extraction from SMRS together with the derived result from NA3.

Recently developed techniques of data analysis are planned to be employed in order to separate the different physics contributions to the dimuon mass spectrum. The so-called machine learning algorithms allow to clusterize real data according to identical behaviors in terms of a set of physics variables. Models are then used to attribute a physics origin to each given set. The clustered data are used to train neural networks at classifying each event according to its probability to be from a given physics origin. The whole method can be validated using Monte-Carlo samples. It is presently being developed for use in the COMPASS experiment, to treat the collected Drell-Yan data. Such approach shall allow for the analysis of Drell-Yan events not only in the traditionally considered ”safe range” (free from contaminations) $4.3 < M < 8.5$ GeV, but also to analyse it in the extended region $3.8 < M < 8.5$ (dominated by Drell-Yan, and even to add the very challenging lower mass range $2.0 < M < 3.8$, where charmonia is the dominant contribution, together with an important fraction of semi-leptonic open-charm decays into pairs of muons, that come mixed with the Drell-Yan contribution.

In Table 1 the achievable statistics of the proposed experiment for a running period of two CERN years (2×140 days) is compared to the Drell-Yan statistics of past experiments. In the experimental conditions assumed, the sea contribution to the pion momentum could be evaluated with an accuracy of 5% or better.

Experiment	Target type	Beam energy (GeV)	Beam type	Beam intensity (part/sec)	DY mass (GeV/c^2)	DY events
E615	20cm W	252	π^+ π^-	17.6×10^7 18.6×10^7	4.05 – 8.55	5000 30000
NA3	30cm H_2	200	π^+ π^-	2.0×10^7 3.0×10^7	4.1 – 8.5	40 121
NA3	6cm Pt	200	π^+ π^-	2.0×10^7 3.0×10^7	4.2 – 8.5	1767 4961
NA10	120cm D_2	286 140	π^-	65×10^7	4.2 – 8.5 4.35 – 8.5	7800 3200
NA10	12cm W	286 194 140	π^-	65×10^7	4.2 – 8.5 4.07 – 8.5 4.35 – 8.5	49600 155000 29300
COMPASS 2015 COMPASS 2018	110cm NH_3	190	π^-	7.0×10^7	4.3 – 8.5	35000 52000
This exp	100cm C	190	π^+	1.7×10^7	4.3 – 8.5 3.8 – 8.5 2.0 – 8.5	23000 37000 170000
This exp	100cm C	190	π^-	6.8×10^7	4.3 – 8.5 3.8 – 8.5 2.0 – 8.5	22000 34000 161000
This exp	24cm W	190	π^+	0.2×10^7	4.3 – 8.5 3.8 – 8.5 2.0 – 8.5	7000 11000 51000
This exp	24cm W	190	π^-	1.0×10^7	4.3 – 8.5 3.8 – 8.5 2.0 – 8.5	6000 9000 48000

Table 1: Statistics collected by the past experiments, compared with the achievable statistics of the new experiment.

4.1.3 J/ψ production mechanism and the pion gluon distribution

Charmonium production provides a particularly attractive alternative for accessing the badly known meson structure. The cross sections are large, typically a factor of 20 to 30 higher in comparison with the Drell-Yan process. While at collider energies they mainly come from gluon-gluon interaction, at the relatively low fixed-target energies they are sensitive to both quark and gluon momentum densities. The different quark and gluon distributions of the interaction partons result in different x_F dependences. Separating the two contributions should, within some model uncertainties, allow an access to the parton distributions in the beam particle.

Analyses aiming at a determination of the gluon distribution of the pion, $g_\pi(x)$, were performed by some of the pioneering dimuon production experiments, NA3[48] and WA11[49] at CERN. Assuming that the J/ψ production cross section at sufficiently low x_F proceeds through gluon-gluon fusion, the authors provide phenomenological fits to the data, using the simple parametrisation:

$$g_\pi(x) = A(1-x)^\beta, \tag{12}$$

where the parameter β describes the slope of the $g_\pi(x)$ distribution as a function of the Bjorken x and A is a normalization factor. A similar analysis was later done by the E537 collaboration at Fermilab [50], using Be and W targets. In all these experiments the determination of $g_\pi(x)$ depends on the assumptions for the fraction of the J/ψ (or Υ) produced by gluon-gluon fusion and on the knowledge of the nucleon or nuclear gluon distributions. Not surprisingly, the corresponding uncertainties results in a large spread of the derived β values.

The large number of J/ψ dimuon events, collected simultaneously with the proposed pion-induced Drell-Yan data should greatly help in improving the situation. About one million events could be expected for the combined π^+ and π^- data on a ^{12}C target and about half of this number on a ^{184}W target, allowing for a precise determination of the corresponding x_F and p_T distributions. The present better knowledge of the gluon distribution in the nucleon, combined with the important progress achieved in understanding the J/ψ production mechanism should also contribute for a better determination of the gluon distribution in the pion.

The exctraction of $g_\pi(x)$ from the data still relies on a good understanding of the J/ψ production mechanism. Two basic models are used to describe the J/ψ production. The simpler Color Evaporation Model (CEM), has enjoyed considerable success in the past, as it has been shown[51] to successfully describe cross sections and momentum distributions. It treats identically quarkonium and open-charm production, the former one being restricted to invariant masses below the $D\bar{D}$ production threshold. The more recent and more rigorous Non-Relativistic QCD model[52] (NRQCD) explicitly uses color and spin to calculate the various charmonium states. It separates (using factorization) the short-distance perturbative and the long-distance non-perturbative effects. The non-perturbative factors in NRQCD are treated as matrix elements that are calculated or determined from the experimental data.

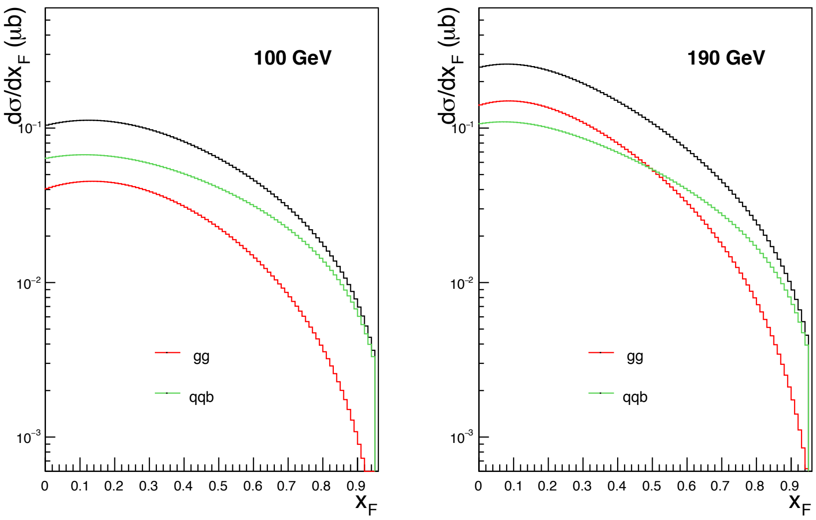

Figure 8: Cross sections for the pion-induced J/ψ x_F distribution at 100 GeV (left) and 190 GeV (right) in the CEM for a ^{12}C target. The red, green and black curves show the gg, $q\bar{q}$, and total cross sections, respectively.

In both models the cross section is a sum of two main contributions: $q\bar{q}$ annihilation and gg fusion. A detailed study of their x_F dependence[53] shows that, in spite of some quantitative differences, both models qualitatively agree: the gg term dominates at low x_F, whereas the $q\bar{q}$ term becomes important at large x_F. In addition, the relative gg fraction decreses when lowering the incident pion energy. This is illustrated in Fig.8, for the CEM at LO of QCD for two energies: 100 GeV and 190 GeV. For both energies the same scaling factor of 0.389, as fitted to the J/ψ production data[48] on a Pt target, is used. At 100 GeV the $q\bar{q}$ contribution dominates the cross section over the entire range of x_F, whereas at 190 GeV it is larger for $x_F > 0.5$ only.

The different relative fractions of gg and $q\bar{q}$ as a function of the energy can be further constrained by comparing J/ψ production data at different energies. The proposed DY data should be taken at 190 GeV. Additional pion data could be collected at lower incident energies either in a dedicated run, or simultaneously with the kaon structure studies using the RF-separated beams. The data from two energies could then be combined for a separate extraction of the the gg and $q\bar{q}$ x_F dcontributions.

Such study could allow for a further constrains on the available J/ψ production models at low centre-of-mass energies. A good understanding of the production mechanism is a mandatory condition for a reliable extraction of the pion quark and gluon densities.

4.1.4 Nuclear Dependence Studies: Flavour-dependent valence quark

The distributions of partons in a bound nucleon differ from those in a free nucleon. More than thirty years ago, a measurement made by the European Muon Collaboration (EMC) showed [54] that medium modifications can play a significant role for nuclear observables. Since then, an impressive amount of deep-inelastic scattering (DIS) data taken in several laboratories around the world has been accumulated [55]. One of the main findings of these studies is that quarks play an important role in the determination of the properties of nuclei. On the theoretical side, many models have been proposed, but a satisfactory explanation of the EMC effect is still missing [56]. The situation has recently become more perplexing, after a JLab experiment on light nuclei[57] provided evidence that the nuclear dependence is not always a function of the atomic number or the mean nuclear density.

DIS experiments are only sensitive to the charge-weighted sum of the quark and antiquark distributions. However, nuclear effects could be different for up and down quarks. Here Drell-Yan experiments can play a major role, as with different pion beam charges one or the other valence distributions are preferentially accessed.

The possibility of flavor dependent quark modifications in nuclei was raised by several authors, namely recently by [58]. The inclusion of pion-induced Drell-Yan data, together with the independent contraints on up and down quarks may have strong impact in the nuclear PDF global fits. This is illustrated in figure 9, where the results for the valence distribution modification on tungsten found by the nCTEQ15 group releases such quark flavor contraints, but includes no data effectively constraining it. Thus the over-estimated green error bar. On the contrary, the EPS09 extraction shown by the blue band in the figure, that imposes same nuclear modifications for up and down quarks, underestimates severely the error bars. The potencial impact of pion induced Drell-Yan data becomes evident.

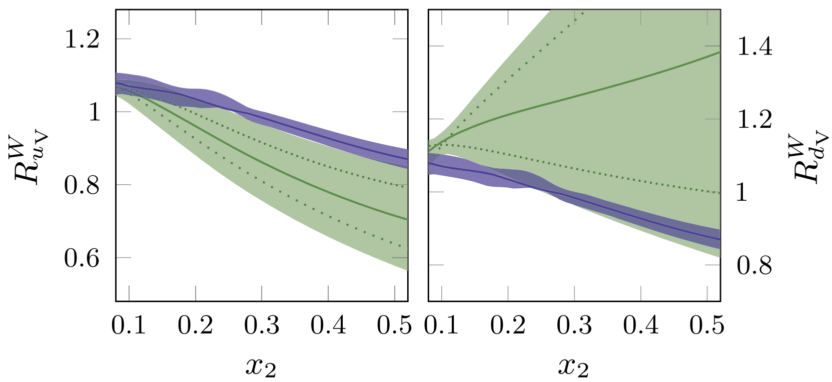

Figure 9: From Paakinen et al. [58]

A new measurement would aim at a precise pion-induced DY measurement in order to evaluate the EMC effect on the valence quarks. A comparison between the Drell-Yan data collected with both positive and negative pion beams should allow for a flavour-dependent study of the nuclear effects.

A recent calculation[59], based on the Nambu-Jona-Lasinio (NJL) model, was used to evaluate the nuclear quark distributions inside a large-A nucleus. A remarkable success of the NJL model is that it accounts [59] for a large fraction of the so-called NuTeV anomaly of the weak mixing angle. An important feature of this calculation is that for nuclei with N>Z, the isovector mean field affects differently the light quarks, leading to the prediction of different nuclear modifications for u and d quarks. This is shown in Figure ??. [Explanation for the figure]

Using the CBT model, Dutta et al. [60] have explored the sensitivity of a future Drell-Yan experiment to the flavour-dependent EMC effect. The data available from the NA10 experiment seem to be in agreement with the flavour-dependent PDFs, although a better accuracy is necessary to confirm the effect. This is illustrated in Fig. 10-top, where on the right-hand side the expected accuracy of the proposed measurement is also shown.

The same experimental conditions as described in 4.1.2 are considered. Pythia simulations at leading order with a K-factor of K=2 are performed for a proton and a neutron target separatly. Then the results are combined accordingly to the nuclear composition of the physical targets. The projected statistical uncertainties on the Drell-Yan cross-section ratio for a positive π^+ beam to a π^- beam on tungsten are represented in Fig. 10-middle. The results are compared to the previous measurement performed by E615 and to a leading order calculation using two recent nuclear PDFs. Figure 10-bottom represents another observable introduced by [61], where the sensitivity to the nuclear valence asymmetry is enhanced, as it can be infered from the larger error bands. This new observable makes full usage of the statistics collected by the proposed experiment.

In parallel to the Drell-Yan events, the proposed new measurement will also lead to the collection of large statistics of J/ψ events. The comparison of pion-induced J/ψ production for a heavy target to an isoscalar target could therefore be used to attempt an access to the nuclear gluon distribution, assuming that a separation of the $q\bar{q}$ and gg fusion processes can be performed.

4.1.5 Drell-Yan and J/ψ angular distributions

In parallel to the main measurements, aiming at the pion structure characterization, the study of Drell-Yan and J/ψ angular distributions with both polarities pion beam will be performed. The use of a light isoscalar target, like deuterium or carbon, will provide results complementary to those obtained by COMPASS with an ammonia target.

4.1.6 Run plan: physics goals and required beam time

CERN is presently the only place in the world where high-energy and high-intensity hadron beams of both polarities are available. The beam intensity in the target region is presently limited by radio-protection constraints. An improved radiation shielding in the target region would allow for wider opening of the beam line collimators, thus increasing the beam intensity of the proposed measurements. For conservative reasons, the estimates presented above do not take into account these possible improvements yet. Once implemented these modifications would reduce the two years of data-taking to one year.

The present COMPASS apparatus efficiently complements the uniqueness of the CERN M2 beam line. Built around two large spectrometers, the setup has a large geometrical acceptance, of nearly 40% . This acceptance compares extremely favourably to the acceptances of previous Drell-Yan experiments, usually limited to less than 10%. In addition, the azimuthal acceptance is quite uniform.

Presently, the Drell-Yan data analysis concentrates on the high mass region, 4.3 GeV$< M_{\mu^+\mu^-} <$ 8.5 GeV, avoiding the backgrounds from dimuon decays of heavy vector mesons and, at low mass, also avoiding combinatorial backgrounds. However, new analysis tools based on machine learning techniques are being developed. They are being tested in the COMPASS Drell-Yan data. It is expected that this will

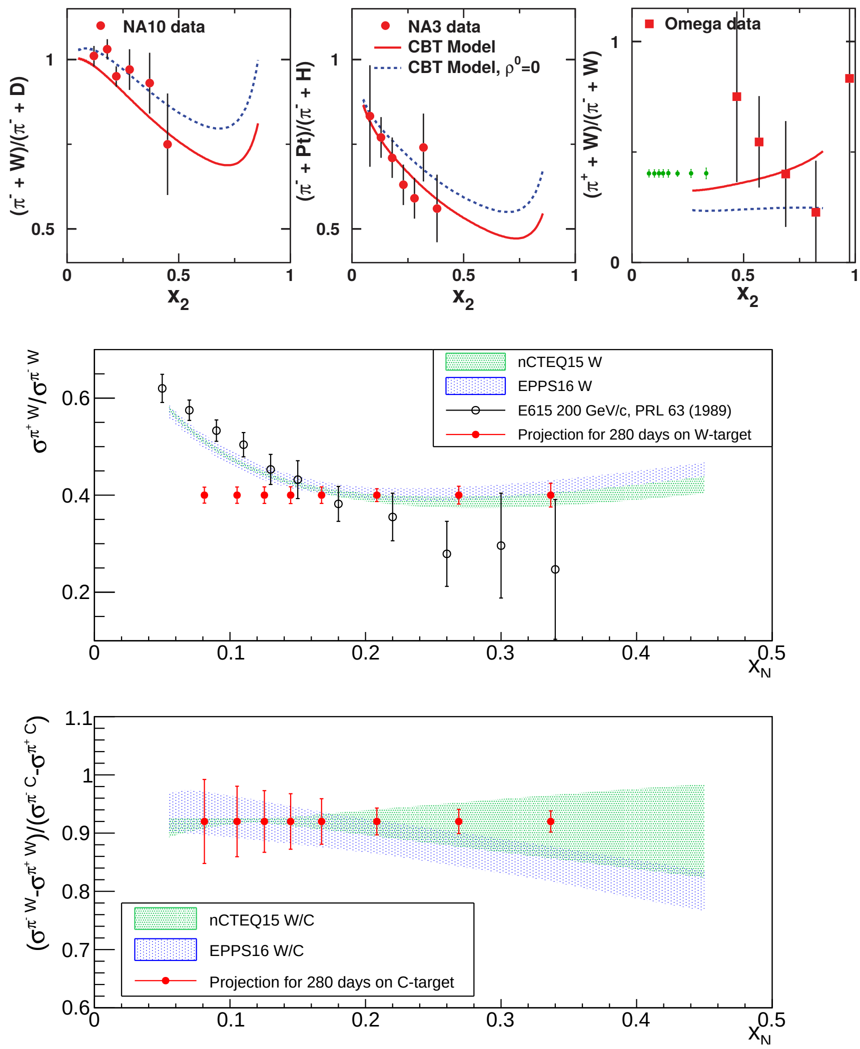

Figure 10: Top row: From Dutta et al. CBT model compared to NA10, NA3 and Omega ratios, the projected statistical uncertainties from the proposed experiment are also shown in green together with Omega data. Middle row: Ratio of Drell-Yan cross-section induced by positive pion beam to that by negative pion beam *vs* x_N. The expected statistical uncertainties from the proposed experiment are compared to E615 results and two sets of nuclear PDFs. Bottom row: Ratio of Drell-Yan cross-section beam charge difference in Tungsten target to that in Carbone target *vs* x_N. The expected accuracy of the proposed experiment is shown together with two set of nuclear PDFs.

increase the available Drell-Yan statistics by a very large factor in the future Drell-Yan running, as shown in table 1.

In addition to novel machine learning techniques for background rejection in the Drell-Yan data analysis, the proposed physics program depends on the development of new beam instrumentation: high-performance particle ID for pion identification in the incoming hadron beam and advanced vertex detectors to improve dimuon resolutions.

In order to maximise the data taking efficiency and precision, we would need to:

– improve the read-out of the two CEDARs (beam PID efficiency >90%, and high purity)

– foresee a dedicated detector for precise luminosity measurement (precision in the order of 3%)

– install beam trackers to achieve a precise beam reconstruction

– build a dedicated vertex detection system for improved vertex resolution

– design a high purity and efficiency dimuon trigger, with target pointing capability

Once these instrumentation upgrades will be in place it is proposed to run for 2 equivalent years with both negative and positive hadron beams (sharing 10:1, as explained previously), using a target setup that includes from upstream to downstream (1) a segmented carbon target (2) a tungsten small target (3) the tungsten beam plug, whose first centimeters are also used as target. New vertex detectors and beam counters will be placed downstream of each sub-target. The requirement of good statistics with a positive pion beam puts an additional constraint to the choice of incident beam momentum. For nominal momentum of 190 GeV/c, the fraction of the positive pions in the beam is 24%. The fraction of pions could be further increased by installing a passive polyethylene absorber along the beam path. Due to the different interaction lengths, the protons in the beam are more absorbed than the pions. With a 2 m long absorber, the NA3 experiment could reach a π^+ fraction of 36% at 200 GeV/c. For an incident momentum of 190 GeV/c this translates into a pion fraction of about 40%. If necessary from counting rate considerations, this fraction could be further increased (by up to 50% more) by choosing a slightly lower incident momentum, of 160 GeV/c.

The alternatives to use the COMPASS polarised ^{6}LiD target or an unpolarised liquid deuterium target, were also studied, but where shown to lead to too low statistics. The unpolarized target choice makes the physics scope of the measurement more limited though, restricting it to the separate access to valence and sea distributions of the pion.

In all the proposed measurements a good separation between pions and kaons is mandatory in what concerns negative hadron beams. In the case of the positive hadron beam, the challenge to identify the 24% pions out of the most abundant protons is even more pressing. An excellent beam particle tagging system, with an efficiency at the level of 90% or higher, is mandatory for the success of the program. This may be achieved by the ongoing upgrade of the present CEDARs (differential Cherenkov counters) used in the COMPASS experiment, or by means of new threshold Cherenkov detectors, as done by NA3, for example.

Assuming a 10:1 share for Drell-Yan between the positive and negative beams respectively, the Drell-Yan events that could be collected in two ”years” (two times 140 effective physics data-taking days), represent a statistical accuracy better by an order of magnitude than that of NA3.

Worldwide competition

High-energy pion beams are exclusively available at CERN. Secondary meson beam lines are also under construction at the J-PARC facility in Japan. However, the energy planned, of up to 15 GeV, remains too low for extensive pion structure studies.

The only alternative way of accessing either the form factors or distribution functions of the pion relies on the validity of the pion-cloud model. Investigation of the pion structure through leading neutron DIS electro-production were performed[39] at HERA. While these experiments cover the x region below $x = 0.01$, the resulting extraction of the amount of pion sea suffers from large model uncertainties, mainly coming from the unknown normalisation of the pion flux. An experiment at JLab[62] proposes to make similar measurements in the large x region and to normalise the pion flux to the available Drell-Yan data.

In what concerns the J/ψ studies, there are currently no other laboratories where pion-induced charmonium production can be investigated.

An exploration of the nuclear sea quark distribution has just been completed by the SeaQuest experiment [63] at Fermilab. Using the proton-induced Drell-Yan process at incident momentum of 120 GeV/c, this experiment probes the antiquark distributions in nuclei. If combined with future Drell-Yan data for the valence quark, as detailed in this proposal, the two experiments are complementary to each other.

The JLab EMC PVDIS experiment[64] proposes to investigate possible flavour-dependent nuclear medium modification effects using parity-violating deep inelastic scattering on a ^{48}Ca target, as suggested in Ref. [65].

4.2 Spectroscopy with Low-Energy Antiprotons

4.2.1 Physics Case

Although conceptually rather simple, the strong interaction between quarks and gluons is still far from being understood. At distance scales much smaller than the size of a nucleon, perturbative methods are routinely being used to make precision calculations of strong interaction effects. The perturbative approach, however, fails dramatically at distances approaching the nucleon size, when the coupling constant α_s is of order unity and where pions and other light hadrons become the relevant degrees of freedom. The spectroscopy of hadrons is a powerful tool towards a better understanding of the strong interaction between quarks and gluons in this regime.

The observation of many charmonium- and bottomonium-like X, Y, Z states which do not match the scheme ecpected from model calculations, has triggered a tremendous interest in this exciting field of physics in recent years (see e.g. [66] for a recent review). COMPASS has observed a similar resonance-like signal in the light-quark sector, the $a_1(1420)$ [67]. Figure 11 summarizes the current status of the charmonium-like spectrum [66]. All states indicated by blue and magenta horizontal lines are candidates for states beyond the $q\bar{q}$ configuration of mesons, which have been sought-after for many years.

QCD allows for and predicts full multiplets of such states, in contrast to very few (or even none) which have been unambiguously established experimentally. Recently, Lattice Gauge Theory started to make predictions for non-exotic and exotic charmonium-like states, albeit with an unphysical pion mass and still ignoring decays. Nevertheless, such calculations are useful as a guidance towards a future understanding of the spectrum. Figure 12, e.g., shows the spectrum of hybrid candidates obtained by the Hadron Spectrum Collaboration for a pion mass of 400 GeV. The pattern of quantum numbers follows the same structure as in the light-meson sector [68], with a low-lying supermultiplet of hybrid mesons with quantum numbers 0^{-+}, 1^{--}, 2^{-+} and 1^{-+}, the latter being a spin-exotic multiplet.

In recent years, COMPASS has studied the spectrum of light-quark mesons with unprecedented statistical precision, requiring the development of novel analysis techniques in order to minimize the model bias when interpreting the data. Using a high-energy pion or proton beam scattering off a liquid hydrogen or solid nuclear targets, excited states were produced in diffractive reactions which are dominated by the exchange of a Pomeron in the t-channel (Fig. 13a).

Whereas diffractive reactions of beam pions or kaons dominantly produce final states containing light quarks, experiments employing the annihilation of antiprotons of comparatively low energy between 12 GeV and 20 GeV provide a different and complementary access to excited states of mesons and baryons, covering not only the light and strange quark sector, but also the charmonium and possibly the bottomonium region. In the past, a wealth of data was collected by experiments employing antiproton-proton annihilation, e.g. Crystal Barrel at LEAR [70] and experiments E760 and E835 at Fermilab [71, 72]. The PANDA experiment a FAIR will use a dedicated antiproton storage ring to study, among other physics topics, the spectrum of mesons in the charmonium region [73].

Antiproton annihilation (13b) can proceed either in flight or at rest. For annihilation in flight, also high-spin states can be populated (up to $L \sim 15$ at $\sqrt{s} \sim 6$ GeV). New states are generated either resonantly in s-channel formation or in associated production together with a recoiling particle. The quantum numbers of the multi-meson system are restricted only by conservation laws of the reaction. The final state will contain contributions from all possible intermediate states with different quantum numbers. A partial wave analysis is usually required to disentangle the different contributions. The formation of states provides access to all states with non-exotic quantum numbers, in contrast to e.g. e^+e^- annihilation, where

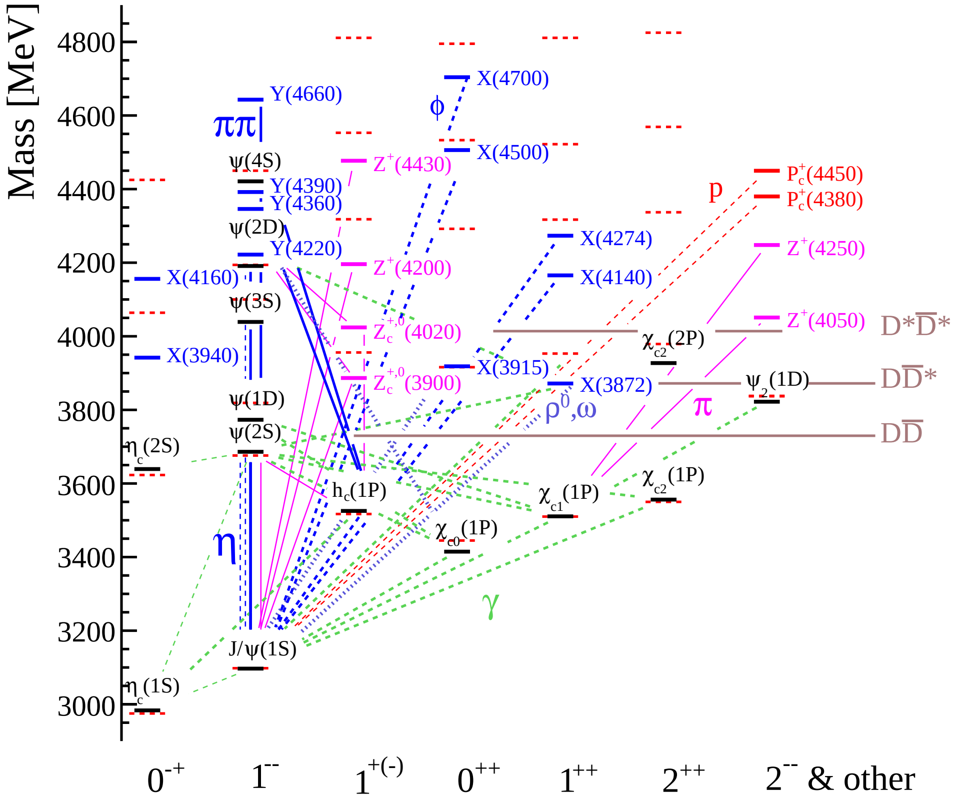

Figure 11: Current status of the charmonium-like spectrum [66]. Horizontal lines indicate (red) expected states, (black) experimentally established states, (brown) open flavor thresholds, (blue, magenta) candidates for chamornium-like states. The lines connecting the states denote known transitions.

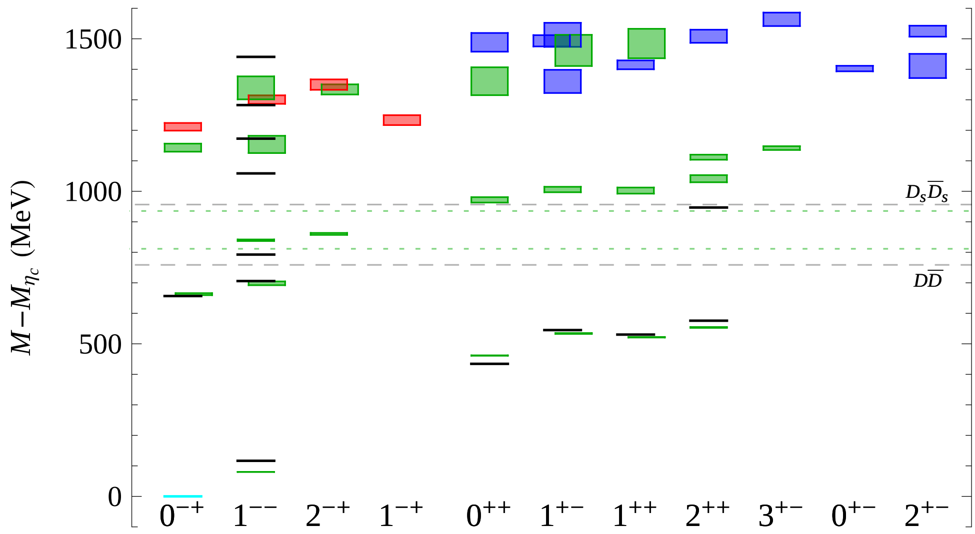

Figure 12: Lattice QCD spectrum for charmonium hybrid candidates [69]. Red (dark blue) boxes are states suggested to be members of the lightest (first excited) hybrid supermultiplet.

Figure 13: Production mechanisms of mesons. (a) Diffractive production in peripheral scattering of high-energy hadrons off a proton or nuclear target. (b) Proton-Antiproton annihilation of a low-energy antiproton beam on a proton target. X can be a $q\bar{q}$ state, a hybrid with gluonic degrees of freedom or a glueball without valence quark content.

only states with quantum numbers 1^{--} are directly formed. Especially the production in association with a recoil particle in addition allows states with spin-exotic exotic quantum numbers to be produced. This is the mode with the highest discovery potential for new states, including states with explicit gluonic degrees of freedom, i.e. hybrids or glueballs in the charmonium sector. Consequently, this is where an experiment at the M2 beamline of the SPS can make important contributions, long before the start of PANDA, which is currently envisaged for 2025, albeit still with large uncertainties and at low luminosity at best.

The M2 beam line can provide, with minimal modifications compared to the present setup, a rather clean beam of antiprotons with momenta around 12 to 20 GeV. According to preliminary calculations, the intensity of antiprotons at the target is between $1.1 \cdot 10^7$ and $1.8 \cdot 10^7$ per pulse of 10^{13} protons on the production target at momenta of 12 and 20 GeV, respectively, and is limited by radiation protection issues. Employing a 40 cm long liquid hydrogen target, as for the measurements with a pion beam, a luminosity of the order of $10^{30}\,\mathrm{cm}^{-2}\mathrm{s}^{-1}$ can be achieved.

This opens the possibility to use antiproton annihilations as a tool to study the spectrum of quarkonia and possibly exotic states. According to model and lattice calculations, the lightest charmonium hybrid is predicted at a mass around 4.3 GeV with spin-exotic quantum numbers. Also the lowest-mass glueball with spin-exotic quantum numbers, predicted at a mass between 4 and 5 GeV is within the kinematic reach of this experiment. A production survey of these states could thus be performed at the SPS of CERN, including the production of high-spin states. Other possible measurements include the measurements of $\overline{p}p$ production cross sections for X,Y,Z states. The production cross sections of exotic charmonia are largely unknown and one of the major uncertainties for the simulation of signal-to-background ratios in PANDA. Thus, besides improving our general understanding of the production mechanisms, a better knowledge of these quantities would pave the way for PANDA to strengthen and focus its physics perspectives on precision studies.

The setup for these measurements will make use of the existing forward spectrometer, augmented by a powerful target spectrometer to maximize the acceptance for exclusive measurements of multi-particle final states. We are currently investigating several options in this direction, including e.g. the use of parts of the WASA spectrometer.

4.2.2 Beam Line

Starting from the current layout of the M2 beam line, a study in the framework of the Physics Beyond Colliders Initiative has been launched by EN-EA in order to check principal limitations and feasibility of low-energy antiproton beams.

In a first step, the production of antiprotons at several desired energies has been estimated with the help of the so-called Atherton parametrisation [74], based on production measurements on Beryllium

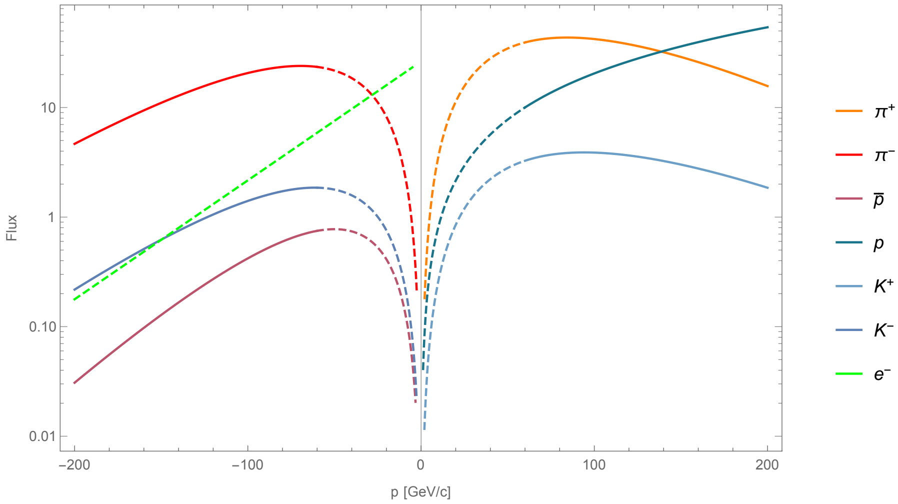

Figure 14: Atherton parametrisation for production of different particle species given in flux per solid angle [steradian], per interacting proton, and per dp [GeV/c] as a function of secondary momenta for a 0 mrad production angle [74].

targets in the North Area. In Fig. 14, the flux of secondary particles at 0 mrad production angle is plotted versus the secondary momentum. For the two study cases at 12 (20) GeV$/c$, the flux is about 0.41 (0.20) antiprotons per interacting proton per steradian per GeV$/c$ momentum bite. This corresponds to about 4.4% to 4.8% of the total negative hadron flux. Based on the experience of operating the West Area in the 1990s, the main background contribution of the beam has been identified as electrons. As depicted in Fig. 14, the electrons at lower energies have a contribution of over 90% to the total flux. Hence, a suppression of the electron background has to be included, most probably by the insertion of a thin lead sheet at a focal position in the beam optics in order to keep the contribution by multiple scattering to the beam divergence at the CEDAR counters low.

Given a 99% suppression of electrons and including the decay of hadrons along the M2 line, this would result in a fraction of 18.2% (11.3%) of antiprotons at the Compass target location for 12 (20) GeV$/c$ beams. With a typical solid angle of $\pi 10^{-5}$, a target efficiency of 40% for the 500 mm T6 target head, a flux of 10^{13} protons on T6, and assuming a 2% momentum bite for new low-energy optics, the resulting antiproton flux would be 10^8 $(5 \cdot 10^7)$ for 12 (20) GeV$/c$ beams. As the intensity in EHN2 is limited by radiation protection to about 10^8 particles per 4.8 s spill, the total antiproton flux thus is limited by the purity of the beam. Hence an upper limit of the antiproton flux at the Compass target is estimated to be $1.8(1.1) \cdot 10^7$ antiprotons per spill.

For an efficient transport of low-energy antiprotons, several optimisations of the M2 beam line could be envisaged. Besides a study of dedicated low-energy optics, a completion of the vacuum in the line would be highly desirable. So far, the M2 beam line is optimised for muon transport, which means several elements specific to muon beams were not designed for operation in vacuum, such as the magnetic collimators (“scrapers”), collimator 5, and 9.9 m of Beryllium absorbers inside bend 4. As a consequence, a total of about 80 m of beam line remain without vacuum. Depending on the operation conditions, two solutions would be preferred. For a full year of operation without muon beams, the above mentioned elements could be removed from the beam line and/or be exchanged by standard magnets and absorbers, which are compatible with the vacuum requirements. In this case, the removal of scrapers will have the consequence of a large muon component in the beam in the order of 3-5 % and a increased muon halo due to the M2 geometry. In case this background cannot be tolerated or an intermediate operation of muon beams is envisaged, another solution could be a fitting of vacuum tanks inside the scrapers. In addition to the optics change and vacuum optimisation, the CEDAR counters would have to be exchanged for so-called West Area CEDARs that are optimised for beams below 100 GeV/c. In this configuration, other optical elements and another gas (N_2) are used.

4.2.3 Measurements

Using an antiproton beam with a momentum between 12 GeV/c and 20 GeV/c, we plan to perform spectroscopy of heavy-quark mesons by measuring exclusive reactions into multi-particle final states. With the available centre-of-mass energies at the M2 beam line, we cover the full range of charmonium-like states up to masses of ~ 6 GeV. In principle, higher beam momenta would allow us even to touch the bottomonium region, although then the intensity of antiprotons will be smaller.

With a production survey at fixed antiproton beam momentum, we plan to study high-spin charmonia and charmonium-like states as well as exotics like hybrids and glueballs. Of particular interest at present is the study of the Z_c multiplets (charged and neutral), which until now have only been observed in e^+e^- reactions.

The cross sections for the production of charmonium-like states in antiproton annihilations are largely unknown. Experimental results on inclusive J/ψ production in $p\bar{p}$ annihilation have been obtained e.g. at CERN SPS at a $\bar{p}$ momentum of 39.5 GeV/c and a cross section of (12 ± 5) nb has been extracted [?]. Theoretical estimates range from 0.1 nb to 10 nb (see e.g. an estimate of $\bar{p}p \to \pi^0 J/\psi$ in [75]). It is thus important to measure these cross sections, firstly in order to test production models and secondly to provide input for simulations of the physics performance which can be achieved with future precision experiments like PANDA.

Based on the luminosity estimated above and using the inclusive J/ψ cross section of 12 nb [?], we will produce of the order of 120,000 inclusive J/ψ per year of running, corresponding to $\sim 7{,}000$ J/ψ decaying to $\mu^+\mu^-$. This number may be increased by a factor of 5 by including e.g. the e^+e^- decay channel and by increasing the target length to 100 cm.

4.2.4 Experimental Requirements

Since the beam at the M2 beamline of the SPS will contain not only antiprotons, but also pions and electrons, it is important that each incoming beam particle is identified and tagged by CEDAR Cherenkov detectors. Since we need to push the intensity to the limit allowed by radioprotection, these detectors have to work efficiently at intensities of 10^8 particles per spill.

As target we envisage a $40 - 100$ cm long cylinder containing liquid hydrogen, similar to what was used for the pion beam measurements at COMPASS in the years 2008-2012. In addition, the use of foils or wires could be envisaged as nuclear targets.

In order to study the required energy and angular acceptance, we performed phase-space simulations of the reactions

1. $p\bar{p} \to \pi^- Z_c^+(4430)$, with $Z_c^+ \to \pi^+ J/\psi$,
2. $p\bar{p} \to \pi^0 Z_c^0(4430)$, with $Z_c^0 \to \pi^0 J/\psi$,
3. $p\bar{p} \to \eta h(4300)$, with $h \to \pi^0\pi^0 J/\psi$ (fictitious $c\bar{c}$ hybrid at 4.3 GeV) and $\eta \to \gamma\gamma$,

all with $J/\psi \to \mu^+\mu^-$, at an antiproton beam momentum of 12 GeV/c. Figure 15 shows the distributions of momenta or energies of charged pions, muons, and photons versus polar angle from the production of Z_c (reactions 1 and 2) in the laboratory frame.

The corresponding phase-space distributions in the laboratory frame for reaction 3 are shown in Fig. 16.

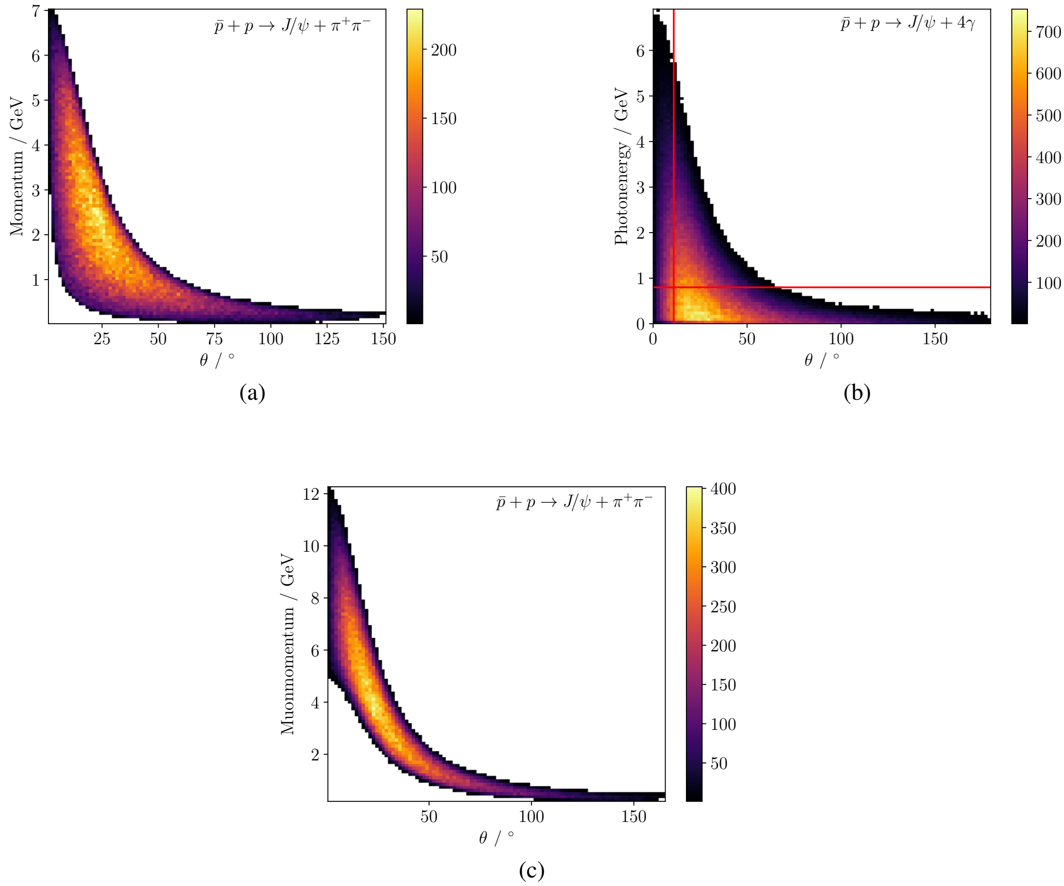

Figure 15: Kinematic distributions from phase-space simulations of $\bar{p}p$ annihilation at an antiproton beam momentum of $12\,\mathrm{GeV}/c$. (a) Charged-pion momentum vs polar angle from the reaction $p\bar{p}\rightarrow\pi^-Z_c^+(4430)$, with $Z_c^+\rightarrow\pi^+J/\psi$, (b) Photon energy vs polar angle from the reaction $p\bar{p}\rightarrow\pi^0Z_c^0(4430)$, with $Z_c^0\rightarrow\pi^0J/\psi$ and (c) muon momentum vs polar angle from the decay of J/ψ.

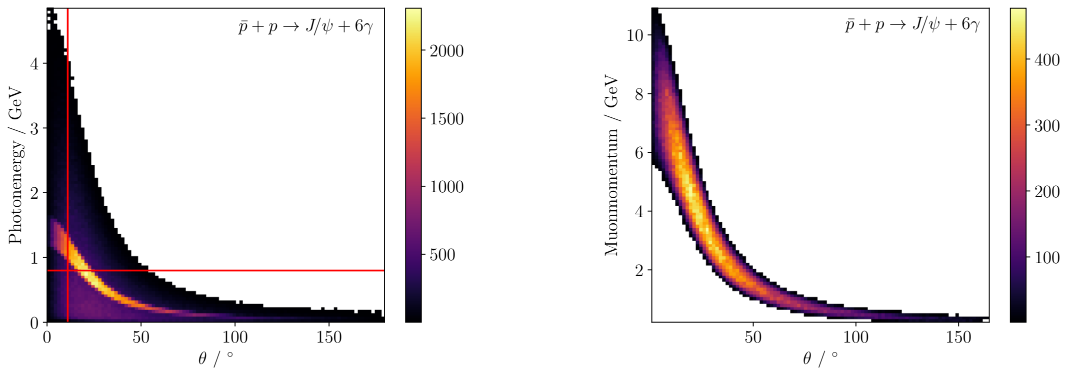

(a) (b)

Figure 16: Kinematic distributions from phase-space simulations of $\bar{p}p$ annihilation at an antiproton beam momentum of $12\,\mathrm{GeV}/c$. (a) Photon energy vs polar angle from the reaction $p\bar{p} \to \eta h(4300)$, with $h(4300) \to \pi^0\pi^0 J/\psi$ and $\eta \to \gamma\gamma$. The red lines indicate the acceptance of the WASA calorimeter discussed in section 6.2.4. (b) Muon momenta vs polar angle from the decay of J/ψ.

Because of the reduced beam energy compared to the earlier measurements performed by COMPASS, which used beam energies above $100\,\mathrm{GeV}$ with a correspondingly larger boost of final-state particles in forward direction, it is clear that in order to perform exclusive measurements, an additional coverage with charged-particle tracking and calorimetry surrounding the target is needed. In particular, the detection of photons from the decay of π^0 and η will be of importance for the reduction of combinatorial background and thus the identification of states.

A trigger should include dimuon and possibly dielectron production from the decay of J/ψ. While muon identification requires dedicated muon chambers, electron identification could be achieved by a transition radiation tracker.

The considerations about the experimental setup are detailed in Sec. 6.2.4.

4.3 Measurement of antimatter production cross sections for Dark Matter Search

4.3.1 Physics Case

Multiple and concurring evidences indicate that the vast majority of the matter content of the universe is non barionic and electrically neutral. This constituent of the universe is usually called Dark Matter (DM), for its lack of electromagnetic interactions.

The DM surrounds the galaxies and the universe large structures, being the major constituent of the gravitational fabric of the universe. The Dark Matter origin an the nature is one of the most intriguing puzzle still unresolved, the most appealing hypothesis is that it would consist of weakly interacting massive particles (WIMPs), supposed to be cold thermal relics of the Big-Bang.

The indirect detection of DM is based on the search of the products of DM annihilation or decay. They should appear as distortions in the gamma rays spectra or as anomalies in the rare Cosmic Ray components. In particular cosmic rays antimatter components, like antiprotons, antideuterons and positrons, promise to provide sensitivity to DM annihilation on the top of the standard astrophysical production.

$$\chi + \chi \to q\bar{q}, W^-W^+, \ldots \to \bar{p}, \bar{D}, e^+, \gamma, \nu$$

The search for DM annihilation products motivated the development of new challenging experiments, either ground-based or in space, which produced spectacular results; among them, the AMS-02 experiment on the International Space Station. In the following, we will briefly discuss how the measurements of antimatter production cross sections, namely antiprotons and antideuterons, performed by experiments at the accelerators, is crucial for the the DM indirect search.

4.3.1.1 Antiproton production cross section The dominant part of the antiprotons in our galaxy originates by the inelastic scattering of incoming Cosmic Rays (CRs) off Interstellar Medium (ISM) nuclei at rest and represents the background when searching for small contributions from exotic sources.

After the breakthrough from the satellite-borne PAMELA detector, the $\bar{p}$ flux and the $\bar{p}$/p ratio have been measured with unprecedented accuracy of a few percent by AMS-02 [**?**] over an energy range from below 1 GeV up to a few hundreds of GeV, showing that above $\sim 60 GeV$ that ratio is independent of the energy.

The Cosmic Ray generated antiproton (secondary) component is expected to decrease more rapidly than the primary proton spectrum, however the predictions are affected by several uncertainties. As depicted in figure 17 [**?**] , we can identify three sources of uncertainty: the primary slopes, the propagation in the Galaxy [**?**] , and the antiproton production cross section. While AMS-02 measurements will contribute to reduce the first two, new dedicated measurement must be performed for the latter.

To be able to profit of the AMS-02 high precision data, a similar accuracy in the computation of $\bar{p}$ source term for all the production channels has to be achieved. Nuclei heavier than protons and helium give a

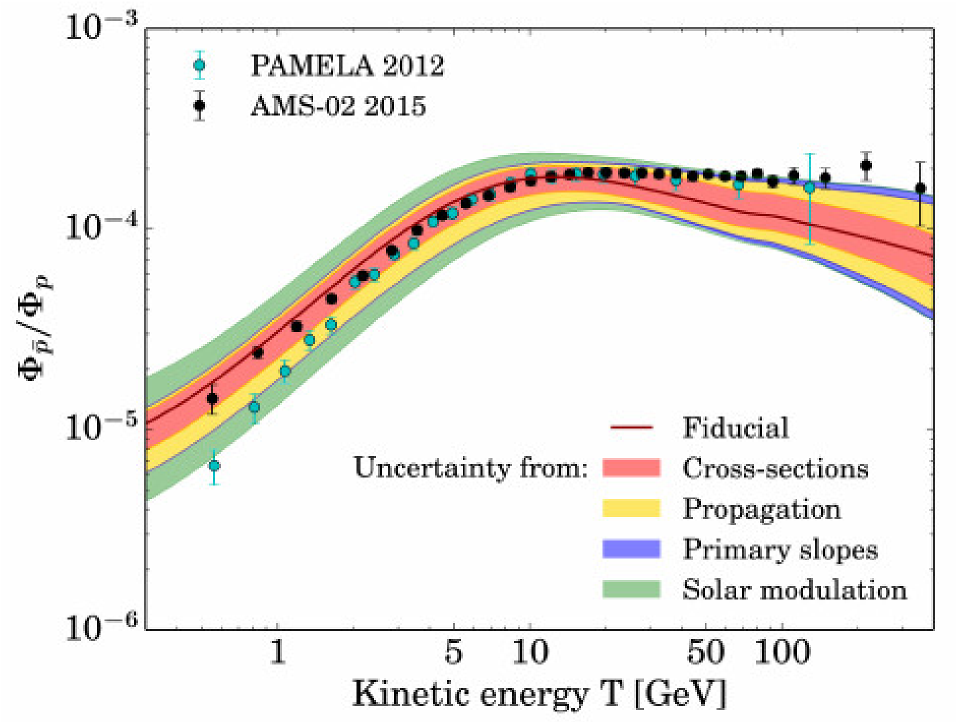

Figure 17: The combined total uncertainty on the predicted secondary $\bar{p}$ / p ratio, superimposed to the PAMELA and the AMS-02 data.

very small or negligible contribution, thus playing a marginal role, either as projectiles or targets, in the secondary antiprotons production. The dominant reactions are the ones involving protons and helium (p-p, p-He, He-p, He-He). Accurate measurements of $\bar{p}$ production cross-section in p-p collisions and p-He collisions are thus of fundamental importance in a wide energy range from 10 GeV to a few TeV in order to reduce the uncertainty on the secondary $\bar{p}$ production and finally disentangle if there is an evidence of exotic components coming from DM annihilation or decay in AMS-02.

While some experimental datasets on p-p collisions are available, the very first dataset on p-He collision was collected at the end of 2015 by the LHCb experiment at 4 TeV and 7 TeV. A COMPASS++ fix target experiment at CERN would contribute to this fundamental DM search, performing a complementary measurement with proton beam of few hundreds of GeV/c impinging on a liquid He target.

4.3.1.2 Antideuteron production With respect to the indirect DM search using antiprotons and positrons, which suffer from relatively high and uncertain standard astrophysical background, search with low energy antideuterons benefit from strongly suppressed background.

The dominant secondary $\bar{D}$ production channel is the one involving p-H collisions, followed by cosmic proton colliding on IS helium (p-He). The $\bar{D}$ flux from a wide range of DM models exceeds the background flux by more than two orders of magnitude in the energy range below 0.25 GeV/n, and by more than an order of magnitude up to 1 GeV/n; thus low energy $\bar{D}$ offer a potential breakthrough in an unexplored phase space for indirect DM search. And many dark matter models predict antideuteron flux within the reach of currently operating or planned experiments, like BESS, AMS-02, and GAPS. Nevertheless the largest uncertainties in the flux estimation, both for primary and secondary (background) $\bar{D}$ are due to the hadronization and coalescence models used to describe antideuteron formation, and to the propagation models. Understanding antideuteron production is thus one of the crucial point for the interpretation of the cosmic-ray data, which impacts both the antideuteron background expectation as well as the formation in the aftermath of dark matter annihilations or decays. The predicted antideuteron fluxes depend on the only free paramater of the coalescence model, i.e. the coalescence momentum p_0, defined as the radius of the sphere in the momentum space, within which any (anti)nucleons will coalesce to produce (anti)nucleus. This parameter has to be determined fitting the theoretical model predictions to the available experimental data on $\bar{D}$ production, collected by ALEPH, CLEO, CERN ISR, ZEUS, ALICE, BABAR. No a univoque value of p_0 could determined that simultaneosly fits all the data. This uncertainty has quite dramatic implications for the search for cosmic antideuterons, due to the strong dependence of the antideuteron yield on the coalescence momentum, $N_{\bar{D}} \propto p_0^3$. The antideuteron production cross-section is not further discussed in this document in the following sections, but it will be object of a more detailed feasibility study in a proposal.

4.3.2 Feasibility of the measurement at COMPASS

The production cross section for antiprotons from $p+p$ and $p+He$ collisions is known only with errors of the order from 20% to 30% depending on the energy.

This cross section cannot simply be constrained by measurement on the other products of the interactions, a direct measurement is then needed. Here we explore the possibility to use a magnetic spectrometer as the COMPASS detector at CERN to measure the products of the interactions of SPS protons of different momenta on a target of liquid hydrogen and liquid helium.

We simulate $p+p$ and $p+He$ interactions to characterize the features of these events in term of multiplicity, energy and angular distribution of the produced particles, in particular the antiprotons, and we study the COMPASS performances for these events topology.

Finally we discuss the measurement of the differential antiproton production cross section and the possible sources of systematic errors.

We performed the simulation with two beam/target configurations:

1. 190 GeV/c protons on liquid H_2

2. 190 GeV/c protons on liquid He

As summarized in table 2, antiproton events represent 7% of the events with an interaction, for 190 GeV/c beam energy. We are interested in understanding the features of these events in terms of the

	p+p	p+He
Beam Mom	190 GeV/c	190 GeV/c
Mult ($Z \neq 0$)	7.7	10.1
$\bar{p}$ ev frac	7.1%	7.7%
$\bar{p}$ $\langle p \rangle$(GeV/c)	15.3	14.5

Table 2: Simulation: antiproton event fraction with respect the interaction events, and antiproton average energy.

number of charged tracks, their forward angle, the number of produced antiprotons and their energy distribution.

We show some data for $p+p$ events at 190 GeV/c. Figure 18 reports the average particle occurrency, figure 19 reports the distribution of final state multiplicity and charged final state multiplicity and finally figure 20 shows the antiproton energy spectrum.

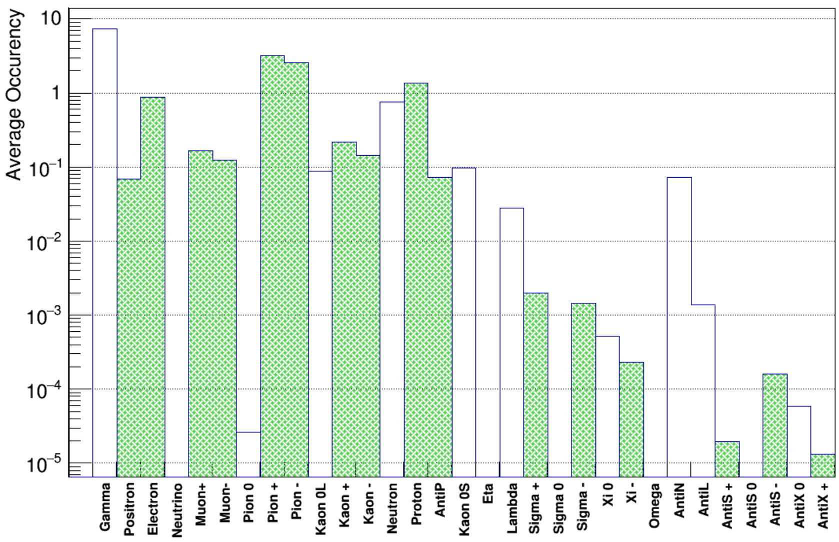

Figure 18: Particle type abundance in $p+p$ 190 GeV/c events.

4.3.2.1 COMPASS performance on measuring interaction events We studied the COMPASS performance in terms of:

– ability to reconstruct the tracks within its geometric acceptance

– momentum measurement resolution for each track

– vertex reconstruction and position resolution

– particle identification (RICH)

The target geometry allows for accepting particles with an angle to the longitudinal COMPASS axis (z) smaller than 180 mrad ($\sim$ 10 deg or $\eta > 2.4$), fig 21.

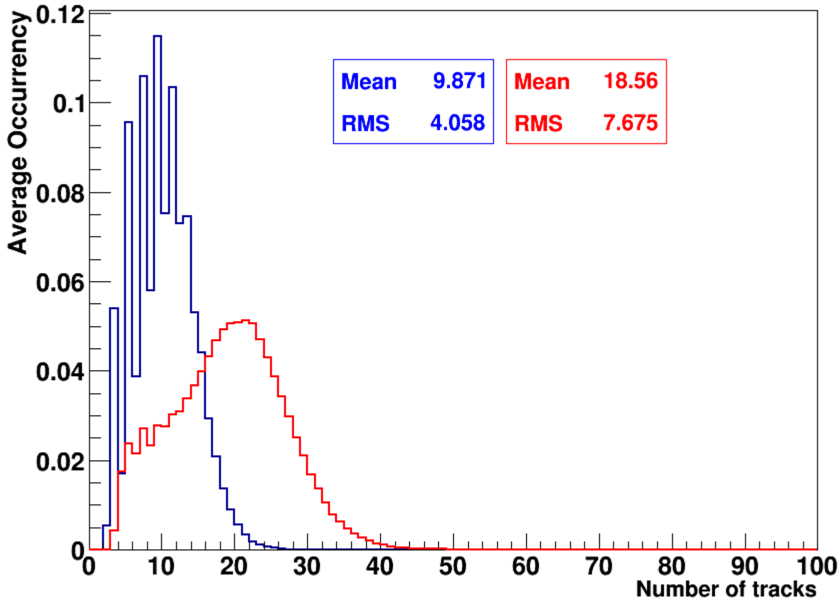

Figure 19: Particle multiplicity in $p+p$ 190 GeV/c events. Blue line all tracks, red line charged tracks.

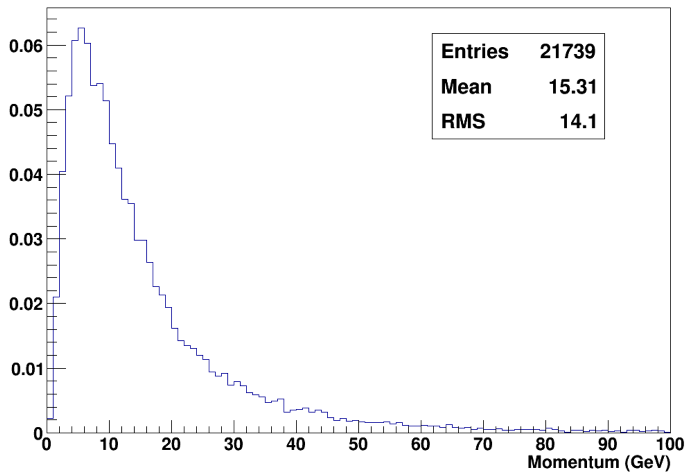

Figure 20: Momentum spectrum of $\overline{p}$ produced in $p+p$ interactions at 190 GeV/c

Figure 22 shows the π^- track reconstruction efficiency as a function of momentum and pseudo rapidity. For momenta above 1 GeV/c and pseudo rapidity above 2.4, the tracking efficiency is greater than 90% and is mildly dependent on momentum magnitude and direction. Similar efficiency has been observed for π^+, p and $\overline{p}$; figure 23 shows the momentum dependence of tracking efficiency for these particles. The smaller $\overline{p}$ statistics make the corresponding efficiency curve affected by large errors. The observed similarity between the π^+ and π^- efficiencies, suggests the spectrometer behaves equally for positive and negative tracks, hence it is safe to assume that p and $\overline{p}$ reconstruction efficiencies are the same.

The resolution in the momentum magnitude and direction is also very good. When using the large angle part of the spectrometer (typically $p < 20\ GeV/c$) $\sigma_p/p \approx 1\%$, when the small angle spectrometer is used $\sigma_p/p \approx 0.3\%$. The angular resolution has a typical value of 0.8%, while remaining always better than 3% in the pseudo rapidity range $2.4 < \eta < 8$.

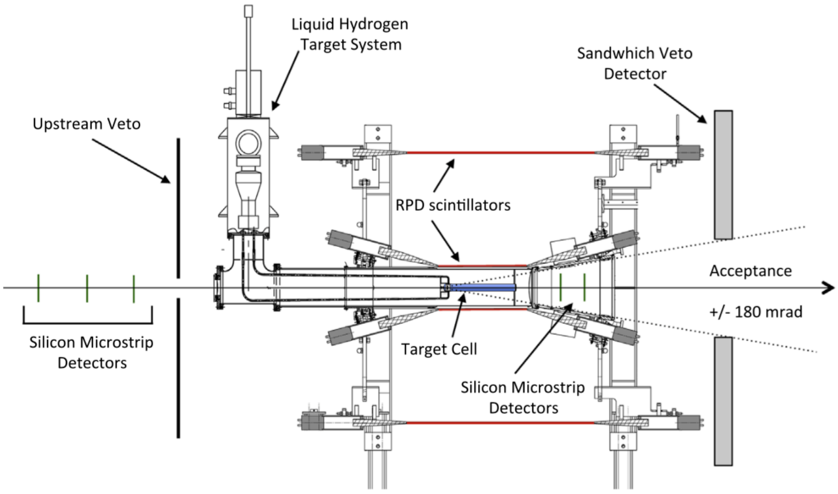

Figure 21: Longitudinal section of the COMPASS liquid $H2$ target.

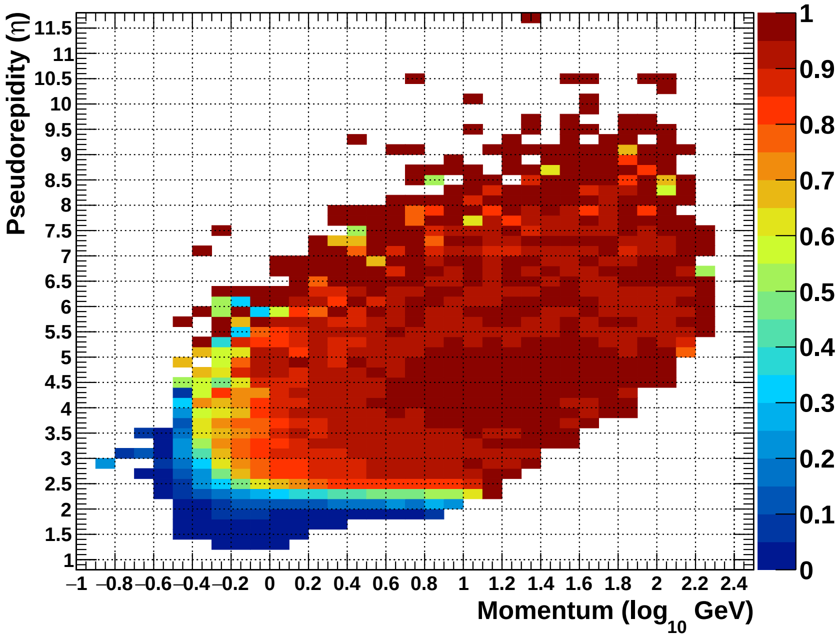

Figure 22: Double differential (η,$log_{10}(p)$) reconstruction efficiency for negative pions from 190 GeV/c p+p interactions.

Track association in vertexes is very efficient. Within the spectrometer acceptance ($\eta > 2.4$, $p > 1\ GeV/c$) the ratio of the primary vertex reconstructed track multiplicity to the MC multiplicity is 0.98 ± 0.05. The vertex position residual in the z direction has a width of $\approx 0.7mm$.

In summary COMPASS spectrometer performs very well in reconstructing the event topology and the track sign and momentum.

Signals from the Ring Imaging Cherenkov (RICH) detector allow to measure the speed of the particle. An estimation of the particle mass is then obtained from the velocity and the rigidity measurement, providing a mean for particle identification.

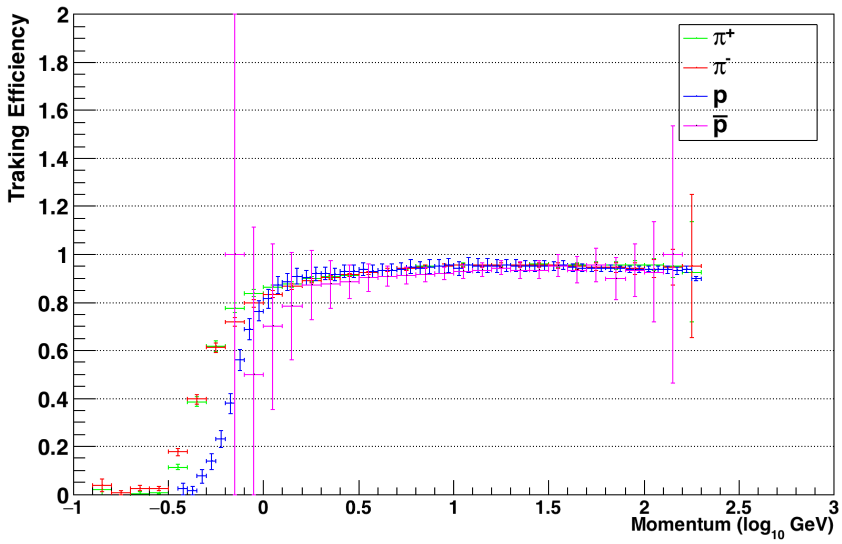

Figure 23: Tracking efficiency as function of the particle momentum, for π^+ (green),π^i (red),p (blue),$\overline{p}$ (purple),

Considering the RICH position $\approx 5m$ downstream from the target, we expect to observe the following particles: $e^{\pm}$, $\mu^{\pm}$, $\pi^{\pm}$, $K^{\pm}$, p and $\overline{p}$ [1]. Muons are otherwise identified by their penetration capability, and can be, for the moment, neglected.

The RICH radiator is a buffer of C_4F_{10} gas with refraction index id $\eta = 1.0014$, this correspond to a threshold in velocity of $\beta = 0.9986$. The corresponding momentum threshold depends on the particle mass: $p_{min} = 2.6\ GeV/c$ for pions, $p_{min} = 9.3\ GeV/c$ for pions, $p_{min} = 17.7\ GeV/c$ for protons. RICH beta resolution $\sigma_\beta/\beta = 0.6\%$ allow for an efficient separation of π, k and p, via mass measurement $m = p/(\beta\gamma)$. Figure 24 shows the reconstructed mass vs the reconstructed momentum for a equal population of π, k and p. The very good separation of the proton signal from the π and K one allows for an unambiguous identification of protons, and hence antiprotons in the momentum range 18 to 45 GeV/c.

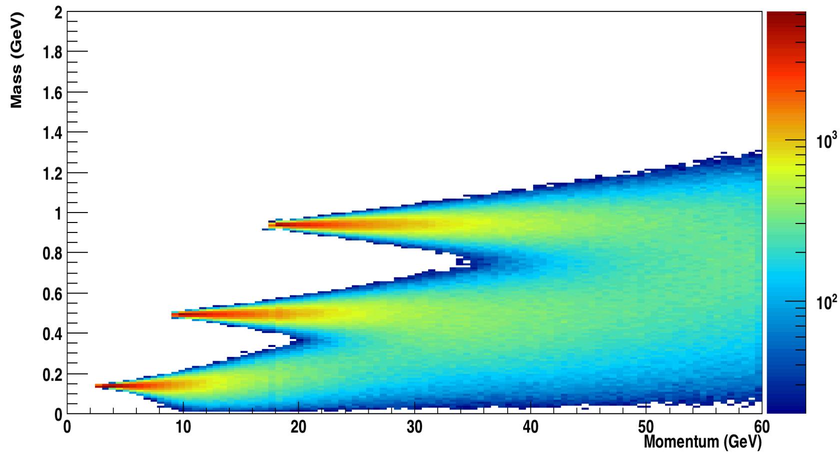

Figure 24: Reconstructed mass from RICH β and p, versus reconstructed momentum. The selected sample has an equal abundance of π k and p.

Below the proton momentum threshold ($\sim 18\ GeV/c$), and above the Kaon threshold ($\sim 10\ GeV/c$), the absence of a RICH signal can be interpreted as an identification of the particle as a proton (or antiproton). This identification must be corrected for the RICH efficiency, and a thorough study should be

[1] Also few track of Hyperons could trigger the RICH but their expected abundance is negligible

implemented to keep this efficiency under control. The use of this additional method would extend the (anti)proton identification range to momenta in the range 10 to 45 GeV/c.

4.3.2.2 Measuring the antiproton cross section We want to measure the double differential (angle and momentum) antiproton cross production from $p+p$ and $p+He$. Following what discussed in the previous section we are going to identify and count the antiproton track in each event as a function of momentum and pseudo rapidity $N_{\overline{p}}(p,\eta)$.

The counting will happen for two separate energy ranges of momentum. The first $p[18,45]GeV/c$ where we can use the RICH to identify the antiprotons by their mass. The second $p[10,18]GeV/c$ where we use the absence of the RICH signal (veto mode) to identify the particle as not π or K.

In both cases the counting must be corrected for several effects including the track efficiency, the RICH detector efficiency, the particle identification efficiency. These efficiencies can be estimated with the MC simulation and possibly directly from the data.

To calculate the antiproton cross section we must divide the (corrected) number of antiproton events, to the total number of interaction events (N_i).

This denominator can be obtained from the trigger number including corrections for several effects.

COMPASS will be operated with a minimum bias trigger, which includes:

- Beam trigger + hodoscope veto: ensures that the particle reach COMPASS within the target cross section, it also includes a preselection of protons from the CEDAR beamline Cherenkov detectors
- Sandwich veto: exclude events with signals outside the COMPASS acceptance after the target
- Beam killer: remove events where protons keep the beam direction 32 m downstream the target.

The beam intensity delivered to the COMPASS beam line (NA M2) will be adjusted to provide $\sim 5\ 10^5\ p/s$ at the target. With this trigger configuration and beam intensity we expect a trigger rate of $\sim 25\ kHz$ well within the performances of the COMPASS DAQ.

In this configuration and assuming a total of 10s of beam from SPS for each minute, we are expected to collect and identify $\sim 25\ 10^4$ events per minute. Considering the antiprotons estimated production cross section, a conservative antiproton identification efficiency of 70%, and a double differential cross section with 20 bins in momentum and pseudorapidity, we will reach a statistical error of 1% after ~ 4 hours of beam time. Including a contingency factor we will need 6 hours of beam time for each combination of target and beam settings.

Several corrections to the events and trigger counts are needed to obtain an accurate measurement. Each of these corrections bring a source of systematic error. For what concerns the trigger count we must account for the trigger efficiency, the DAQ dead time and the purity in selecting protons in the secondary beam. For what concerns the antiproton events count we need to account for the overall event reconstruction efficiency and the antiproton tracking and particle identification efficiencies which are possibly dependent on momentum and pseudorapidity. Overall we expect to reach a systematic error of $\sim 5\%$.

We would like to take data at proton momenta: 50, 100, 190 GeV/c and the maximal momentum achievable at SPS M2 beam line.

4.3.2.3 Antihyperons and antineutrons In order to calculate the total amount of antiprotons produced in our galaxy the contribution from antineutrons and antihyperons decaying into antiprotons has also to be taken into account. The total cross-section is then obtained re-scaling from the prompt production:

$$\sigma_{tot} = \sigma_{promt}(2+\Delta_{IS}+2\Delta_{\Lambda})$$

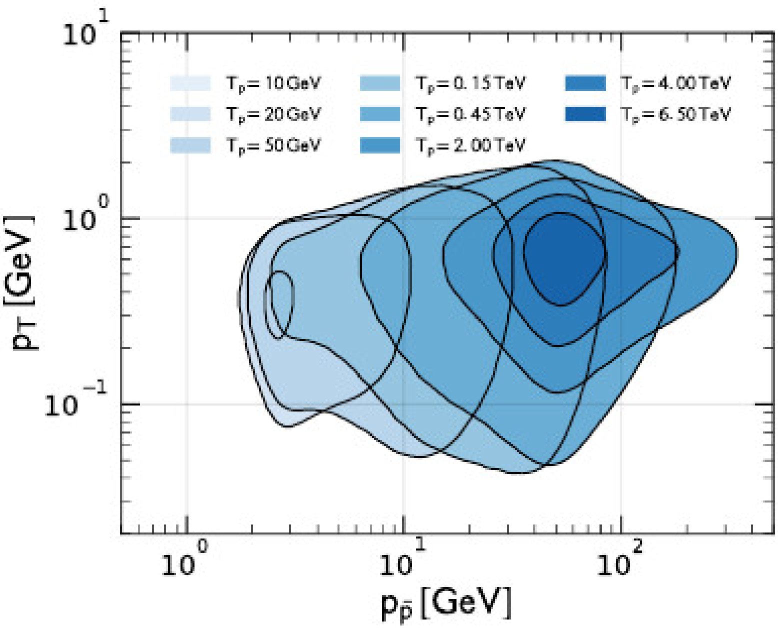

Figure 25: Parameter space for the pHe channel corresponding to an exemplary fixed target experiment. The different Hades areas correspond to different proton beam energies.

where Δ_{IS} is the enhancement factor of antineutrons over antiproton production due to isospin effects, Δ_{Λ} is the hyperon factor, assuming that antiproton and antineutron production from hyperons is equal. The overall uncertainty arising from antineutron and hyperon-indiced production has been evaluated to be energy dependent and not to exceed 5% [**?**]. Moreover in the COMPASS spectrometer secondary vertexes can be reconstructed and distinguished from primary vertexes, thus hyperon-induced antiprotons production can be well separated from prompt production and measured.

4.3.3 Competition and Complementarity

As already mentioned in section 4.3.1, the exceptional experimental accuracy of the order of a few % achieved by AMS-02 on CR $\bar{p}$ flux and $\bar{p}$/p flux ratio poses the challenge of achieving similar precision in phenomenological models that describe the CR $\bar{p}$ flux as produced by the interaction of the CR primary components with the ISM. Such phenomenological prediciton is currently spoiled by the large uncertainty on the anti-p production cross-section. In order to cover all the AMS-02 $\bar{p}$ energy range, precise $p+p \rightarrow \bar{p}+X$ and $p+He \rightarrow \bar{p}+X$ cross-section data are needed with proton beam kinetic energy T_p from 10 GeV to 6 TeV and a pseudorapidity η ranging from 2 to almost 8. The present collection of data is still far from the necessary kinematical coverage, which could be fulfilled by fixed target experiment at CERN, with energies from tens of GeV up to a few TeV. Fig. 25 shows the parameter space that has to be covered as function of T_p and η, at different kinetic energy $T_{\bar{p}}$ of the antiproton, for the case of $p+He \rightarrow \bar{p}+X$ cross-section: in this plot a 3 % accuracy is required on the cross-section determination inside the blue shaded region, and a 30 % accuracy outside the contours, in order to guarantee the AMS-02 precision level on the $\bar{p}$ source term [**?**]. The only data available so far from high energy protons scattering on helium nuclei are the ones collected in May 2016 by LHCb operated in fixed target mode with the SMOG device [**?**]at 6.5 TeV ($\sqrt{S_{NN}} = 110 GeV$, in the pseudorapidity range $2 < \eta < 5$, and in the detected antiproton momentum range $12 < T_{\bar{p}} < 110 GeV/c$. A second sample of data, not yet published, has been collected by LHCb at $\sqrt{S_{NN}} = 86.6 GeV$ in November 2016.
COMPASS++ could perform measurements of antiproton production in pHe collisions at different momenta of the proton beam, from a few tens of GeV/c up to 450 GeV/c, in the pseudorapidity range $2 < \eta < 8$. Combined with the LHCb measurements at very high energy, the COMPASS++ data could

fulfill the necessary kinematical coverage, finally contributing to significantly reduce the uncertainty on the expected amount of secondary antiprotons produced by spallation of primary cosmic rays on the interstellar medium, which is currently one of the most limiting factor for the interpreation of the AMS-02 data on the $\bar{p}$ flux and the $\bar{p}$/p flux ratio for the Dark Matter indirect search.

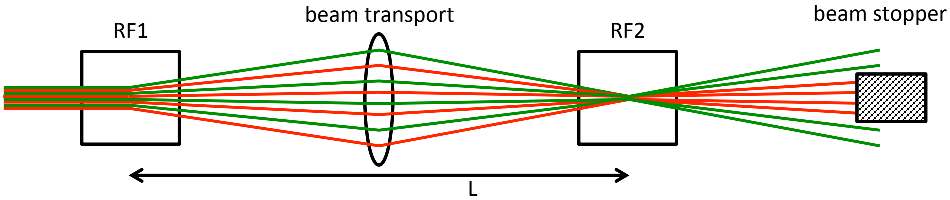

Figure 26: Panofsky-Schnell method for RF-separated beams. The unwanted particles (red) are stopped by a beam stopper while the wanted particles (green) receive a net deflection by the combination of the RF1 and RF2 dipole RF cavities out of the central axis.

5 Hadron Physics with RF-Separated Beams

5.1 Beam Line

For the several proposals of high energy hadron beams, a study of a possible enrichment of desired particle species in the M2 beam has been launched by EN-EA in context of the Physics Beyond Colliders Initiative. Contrary to lower energies as described in Sec. 4.2.2, an enrichment of antiprotons is not naturally given by the length of the beam line due to the higher lifetimes of particles in the laboratory frame. In addition, several proposals prefer a higher content of kaons and positive pions in the beam.

Starting again from studying limitations in terms of production of particles, there are several possibilities to enrich the content of a wanted particle species in the beam, usually by suppression of unwanted particles. Due to the $1/p^3$ dependence of electro-static separators, this method is not reasonable for use at beam energies higher than a few GeV. While in principle an enrichment by differential absorption would be feasible, the very low efficiency, high losses, and small suppression factors for unwanted particles leave only the possibility of RF-separated beams.
The method of RF-separation was first employed at CERN in the 1960s based on ideas of Panofski and Schnell as for instance described in Ref. [78]. The main idea is based on the different velocities of particle species in a beam with a defined momentum.

As displayed in Fig. 26, two dipole RF cavities (RF1 + RF2) are implemented at a given distance L. The transverse kick of RF1 is either amplified or compensated by RF2 depending on the phase difference between both. This phase difference is given by the difference of velocities of the several particle species. For two species 1 and 2 with velocities β_1 and β_2, the phase difference reads $\Delta\Phi = 2\pi(Lf/c)(\beta_1^{-1} - \beta_2^{-1})$. In the limit of large momenta, the phase difference can be expressed as a mass difference between the two species at the beam momentum p:

$$\Delta\Phi = 2\pi(Lf/c)\frac{m_1^2 - m_2^2}{2p^2}$$

For kaons as wanted particles, the phase difference could be chosen at $\Delta\Phi_{\pi p} = 2\pi$, which results in $\Delta\Phi_{\pi K} = 94°$. This means that the kick for both protons and pions would be compensated by RF2 and they would be absorbed in the beam stopper. The kaons would receive a close to maximum transverse kick and mostly go around the stopper. For antiproton beams, the phase difference could be chosen at $\Delta\Phi_{\pi\bar{p}} = \pi$, which results in $\Delta\Phi_{\bar{p}K} = 133°$ and $\Delta\Phi_{\bar{p}e} = 184°$. In this case, the antiprotons would receive an acceptable deflection while electrons and pions are dumped effectively. Based on a study by J.Doornbos at Triumph for CKM, we assume a similar input for frequency ($f = 3.9$ GHz) and kick strength of the RF cavities ($dp_T = 15$ MeV$/c$). Given the length of 1.1 km of the M2 beam line, the length L between cavities cannot be chosen larger. In such a study case, the upper momentum limitation for RF-separated kaon beams would be around 75 GeV$/c$ and around 108 GeV$/c$ for RF-separated antiproton beams, see Fig. 27. As the phase difference depends quadratically on the chosen momentum, such beams would

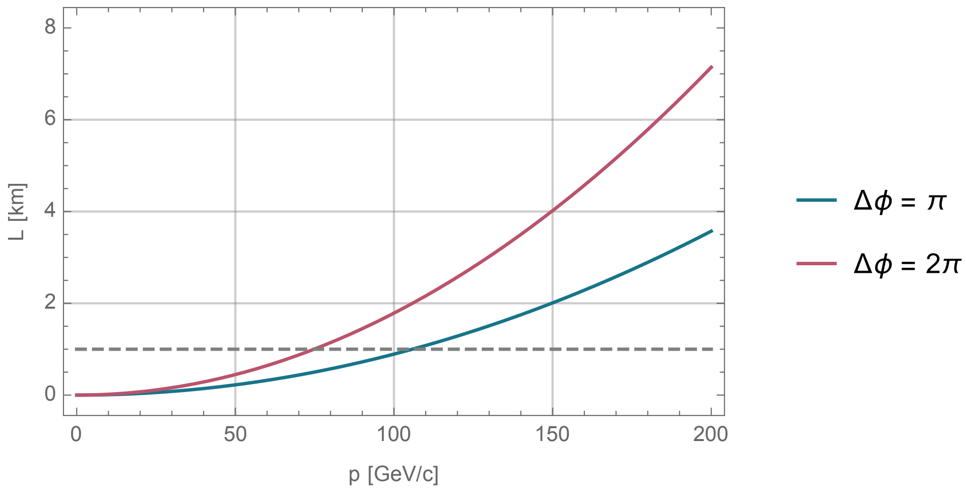

Figure 27: Dependence of the final beam momentum as a function of length L between the RF cavities for two different phase differences. The case of $\Delta\Phi = 2\pi$ corresponds to kaons as wanted particles while $\Delta\Phi = \pi$ would be the choice for antiprotons.

deliver acceptable separation only in a small momentum band. In addition, the dispersion of the beam $\Delta p/p$ needs to be limited to about 1 % in order to prevent a phase shift of $\Delta\Phi_f = \Delta\Phi_i(1 - 2\Delta p/p)$ and thus a lower separation efficiency.

With the given acceptance values and target efficiency as explained in Sec. 4.2.2, an exemplary calculation was performed for the case of a 100 GeV/c antiproton beam. Assuming that 80 % of antiprotons would pass the beam stopper and an optimisation of the solid angle to $10\pi\mu$sterad, one would expect about $8 \cdot 10^7$ antiprotons in EHN2 for 10^{13} incident protons at the T6 target. Due to the current RP restrictions for EHN2 of 10^8 particles per 4.8 s spill, the limit would be given only by the achieved purity of the beam. Assuming 50 % purity, this would be about $5 \cdot 10^7$ antiprotons per spill.

5.2 Spectroscopy of Kaons

5.2.1 Physics Case

The Particle Data Group lists 25 strange mesons, which have been measured in the mass range from 0.5 to 3.1 GeV/c^2 [79]. Only 12 of them are included in the summary tables. The remaining 13 states still need further clarification. For two of them, even their spin-parity quantum numbers J^P are not yet determined. Figure 28 shows the masses of the observed strange mesons and compares them to a relativistic quark-model calculation from ref. [80]. For some well-known states, like e.g. the K ground state, the $K^*(892)$, the $K_1(1270)$, and the $K_1(1400)$, the quark-model prediction agrees well with the experimental observations. However, many predicted states have not yet been observed and some of the observed states do not fit into the quark-model picture. While the PDG lists e.g. three excited K states with $J^{PC} = 0^{-+}$ in the region below 2.5 GeV/c^2, the quark model predicts only two states, neither of those matching with the observed states. another example are the K_0^* states, among which the $K_0^*(1430)$ is the best established one. There is also some experimental evidence for an excited $K_0^*(1950)$, but the observed mass is between the masses of two K_0^* states predicted in ref [80]. However, another quark-model calculation in ref. [81] predicts only one excited state in better agreement with the experimental observations. The most disputed state is the $K_0^*(800)$ or κ. The quark-model calculations in refs. [80, 81] predict no K_0^* state below 1 GeV/c^2. Also the experimental situation is not clear. In many experiments, significant intensity is observed below 1 GeV/c^2, which is typically parameterized as an “effective-range non-resonant” component with a phase shift [82]. However, more advanced analyses, using a K-matrix

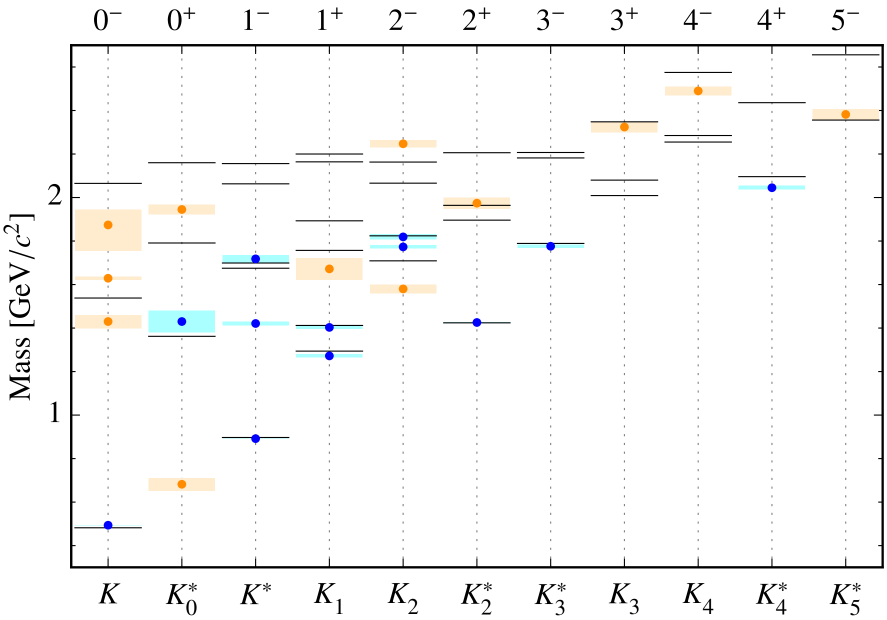

Figure 28: Excitation spectrum of strange mesons from PDG [79] (points and shaded boxes representing the central value and uncertainty of the measurements) compared to a relativistic quark-model prediction from ref. [80] (black lines). States included in the PDG summary table are shown in blue, the remaining states are shown in orange. The states are grouped by their J^P quantum numbers.

approach [83] or Roy-Steiner equations [84] find a pole below $1\,\mathrm{GeV}/c^2$ associated with the $K_0^*(800)$. This situation is similar to the challenges in understanding the S-wave in the $\pi\pi$ system. There, only high-precision data [85] in combination with advanced models [86] allowed to establish the $f_0(500)$ state and to determine its parameters. These examples show that there are still many missing states and open questions in the strange-meson sector, which need to be addressed. The final goal is to identify all strange and light non-strange mesons in the quark-model multiplets. This allows to single out supernumerous states and identify multiplets beyond the quark model, including e.g. gluonic excitations.

Most of the experimental data on strange mesons are based on experiments that were performed more than 30 years ago. Since PDG listings 1990 [87], only four additional kaon states have been included in the PDG listings and only one state entered the summary tables. On the other hand, strange mesons appear in many processes in modern hadron and particle physics. An example are searches for CP violation in multi-body heavy-meson decays, e.g. in $B^\pm \to D^0 K^\pm$ with $D^0 \to K_S^0 \pi^+ \pi^-$, which are currently under study at B-meson factories like BaBar [88], Belle [89], and LHCb [90] and will remain an interesting topic with the upcoming high-precision measurements at Belle II and LHCb. These CP-violation searches are usually Dalitz-plot amplitude analyses [82]. Typically, the isobar model is used, where the decay amplitudes are parameterized by intermediate resonances appearing in the various subsystems of the final-state particles. To keep pace with the high statistical precision of the data, the models require as input an accurate knowledge of these appearing intermediate states, e.g. the strange mesons appearing in the $K_S^0 \pi^\pm$ subsystems in the example above. The large datasets allow to directly study strange mesons in heavy meson decay, as done e.g. in refs. [88, 89]. However, even with the biggest datasets, in the employed isobar models typically the masses and widths of only a few selected states can be fitted to the data while the parameter values of most of the kaon states included in the fit need to be taken from other measurements.

5.2.2 Previous Measurements

A complementary process to directly study strange mesons is peripheral production (diffractive production or charge-exchange reactions) in scattering reactions of a high-energy kaon beam off a fixed target. In the past, this reaction was used by experiments at BNL [91], CERN [92–96], and SLAC [97–100] to study strange mesons decaying into various final states. For example, the LASS experiment measured 100000 events of the $K^-\omega$ final state using an $11\,\mathrm{GeV}/c$ K^- beam [100]. The analysis of these data contributed significantly to establishing the $K_2(1820)$ state. One of the largest datasets was acquired by the ACCMOR collaboration using a $63\,\mathrm{GeV}/c$ K^- beam [94]. They analyzed 200000 events of the reaction $K^- + p \to K^-\pi^-\pi^+ + p_\mathrm{recoil}$. From this dataset, they extracted the parameters of five strange mesons and studied the excitation spectrum of the $J^P = 0^-$ K states. However, even these large data samples are not sufficient to resolve the details of the kaon spectrum, especially for kaon states at higher masses, e.g. the excited $J^P = 0^-$ K states.

Also COMPASS has measured strange mesons in peripheral production in the years 2008 and 2009 using the $\approx 2.5\,\%$ K^- fraction in our secondary hadron beam. In a first analysis of 270000 events of the reaction $K^- + p \to K^-\pi^-\pi^+ + p_\mathrm{recoil}$ [101], we find results consistent with previous measurements [94, 100]. Currently, we are improving this analysis. By major enhancements of the applied PID methods, we are expecting to obtain an event sample of 800000 events. This would increase the statistical precision by a factor of two, compared to the ACCMOR analysis and would allow us to measure masses and widths with an improved precision and possibly give us access to some higher-lying kaon states.

5.2.3 Novel Analysis Techniques

The main goal of the COMPASS physics program in the years 2008 and 2009 was the measurement of the spectrum of light non-strange mesons. Analog to the $K^-\pi^-\pi^+$ channel for strange meson spectroscopy, our flagship channel for light non-strange meson spectroscopy is $\pi^- + p \to \pi^-\pi^-\pi^+ + p_\mathrm{recoil}$, for which we acquired 50 M exclusive events [102]. This huge dataset allows us to apply novel analysis methods. It allows us to perform the partial-wave analysis independently in narrow bins of the squared four-momentum transfer t' between the beam pion and the target proton. The additional information from this t'-resolved analysis helps to better separate the resonant and non-resonant contributions. For the first time, we can also extract the t' dependence of individual signals in our data [103, 104]. Especially for the spectroscopy of strange mesons, a dataset large enough to perform a t'-resolved analysis would be helpful to separate the many overlapping states with same J^P quantum numbers, e.g. the $K_1(1270)$ and $K_1(1400)$. Furthermore, in our $\pi^-\pi^-\pi^+$ analysis, we are able to study the $\pi^-\pi^+$ subsystem of the $\pi^-\pi^-\pi^+$ final state, using a so-called “freed-isobar” approach [102]. Applied to strange-meson spectroscopy, this approach would allow us to study e.g. the K_0^* states in the $K^-\pi^+$ subsystem of the $K^-\pi^-\pi^+$ final state. However, large data samples are mandatory in order to apply this method. Finally, large datasets improve the statistical precision of the measurements and therefore allow us to study much weaker signals, like e.g. the $a_1(1420)$ signal discovered in the our 50 M $\pi^-\pi^-\pi^+$ events [67]. Although it contributes only $0.3\,\%$ to the total intensity, we observe a clear $a_1(1420)$ signal and we extract its parameters with high precision. Also some of the missing strange meson states, which are predicted by the quark-model, could have such small signals. These examples clearly show that large data samples would not only improve the statistical precision of the measurements, but first and foremost would open a whole new field of novel methods and thus would give us new insights into the strange-meson sector. To apply the methods discussed above also to strange meson spectroscopy, a dataset of at least 10 M to 20 M events of the flagship channel $K^- + p \to K^-\pi^-\pi^+ + p_\mathrm{recoil}$ needs to be acquired, which is a factor 15 to 25 more than what has been measured so far.

5.2.4 *Future Measurements at COMPASS*

In order to obtain such a unprecedented dataset for strange-meson spectroscopy, the K^- fraction in the beam has to be vastly increased. One possibility is an RF-separated beam. With a kaon-beam intensity of 4×10^7 per spill at the experiment target position we could acquire a $K^-\pi^-\pi^+$ sample of about 20 M events within one year of data taking.[2] Diffractive production does not depend strongly on the beam energy. With a beam momentum of at least $50\,\mathrm{GeV}/c$, diffractive production will be the dominant process and beam excitations can be well separated from target excitations. This is very important in order to obtain a clean sample of exclusive events and to keep systematic uncertainties from contributions of other processes small. The most important requirement for the experimental setup is a uniform detection efficiency over a broad kinematic range. Apart from precise tracking and vertex reconstruction, a good particle identification is mandatory. As the RF separation does not lead to a pure kaon beam, an efficient beam-particle identification with a low misidentification probability via the CEDAR detectors is required. This requires a small beam divergence at the position of the CEDARs. Additionally, kaons have to be distinguished from pions in the final-state, e.g. for the $K^-\pi^-\pi^+$ final state. This requires a good final state particle identification over most of the momentum range from around $1\,\mathrm{GeV}/c$ up to the beam momentum, with an high efficiency above 50 %. To study also final states with neutral particles, like $K^-\pi^0\pi^0$, the detection of photons over a broad kinematic range by electromagnetic calorimeters is important.

5.2.5 *Planed or Proposed Measurements at other Facilities*

There are also proposals and plans for future measurements of strange mesons at other facilities. In τ decays, strange mesons can appear in subsystems, e.g. in $\tau^- \to K^-\pi^+\pi^-\nu_\tau$, which will be measured at Belle II, BES III and LHCb to study strange mesons. However, the largest possible mass of the strange subsystem is limited by the rather low τ mass of $1.8\,\mathrm{GeV}/c^2$, so that many of the observed or predicted kaon states are out of reach (see figure 28). Furthermore, the event samples are typically an order of magnitude smaller than those of measurements using peripheral production [106, 107]. On the other hand, the low-mass tails of the higher-lying kaon states might still play a role in the mass range of the τ decays. This means that the analysis of τ decays would benefit from a high-precision measurement of those states at COMPASS. The situation is similar for heavy-meson decays. In D decays like e.g. $D \to K\pi\pi$ [108, 109], the mass range is limited by the D mass of $1.86\,\mathrm{GeV}/c^2$. In B decays, the limited dataset size restricts the possibility to study strange mesons with high precision.

Another approach to study strange mesons is in photo production. For example, GlueX proposed a measurement of the $KK\pi\pi$ final state, for which they expect a dataset of 100 M events [110]. Using an approach similar to our “freed-isobar” method, they could study strange mesons in e.g. the $K\pi$ and $K\pi\pi$ subsystems. However, it might be challenging to obtain accurate insight into the strange subsystems from four-body final states, compared to direct strange meson production at COMPASS. Recently, measurements with a secondary K_L beam were proposed at GlueX [111]. In their proposal, they focus on hyperon spectroscopy. For a strange meson spectroscopy program, they mention only the charged and neutral $K\pi$ final state, which gives them access only to K_J^* states.

At J-PARC, a new beam line with a separated kaon beam will be built in the near future [112]. They aim for a K^- intensity of 10^7 per spill, similar to our proposal for COMPASS; however, with a much lower beam momentum of 2 to $10\,\mathrm{GeV}/c$. At these low momenta, the separation between beam and target excitations will become difficult and might lead to larger systematic uncertainties. To our knowledge, no strange meson spectroscopy program has been proposed at J-PARC so far and there are no plans for a general purpose detector with high-precision tracking and calorimetry, which is needed for spectroscopy

[2] We acquired 50 M $\pi^-\pi^-\pi^+$ events within one year of data taking with a π^- beam intensity of 5×10^7 per spill [105]. Assuming that due to the final state PID the detection efficiency for $K^-\pi^-\pi^+$ is approximately 50 % of the one for $\pi^-\pi^-\pi^+$, we expect 20 M $K^-\pi^-\pi^+$ events for one year of data taking.

as discussed above.

Most of the planned or proposed measurements of the strange meson sector can either not compete with the measurement we propose or are complementary to our measurement. Therefore, a spectroscopy program at COMPASS using an RF-separated kaon beam would be an unique opportunity to study the excitation spectrum of strange meson in great detail using the advanced methods we have developed for our $\pi^-\pi^-\pi^+$ sample. This would significantly improve the precision of know states, allow us to search for new states, which complete the light-meson multiplets, and would clarify some of the open questions.

5.3 Drell-Yan physics with high intensity kaon and antiproton beams

Within the conventional quark model, the properties of the hadrons are mainly determined by their valence quark structure. An exchange of a u quark with a d quark makes the neutron different from the proton. Similarly, a replacement of the d quark with a s quark makes the kaon different from the pion. The heavier quark in the kaon leads to a significantly heavier hadron mass, much larger that the difference between the s and d quark masses. The mass scale in each hadron, generated through dynamical chiral symmetry breaking, is associated with the gluon propagation; the massless gluons acquire running mass, which is then transmitted to the quark sector. Exploring the hadron structure, and particularly the quark and gluon distributions on the lightest mesons, provide a glimpse to the appearance of the hadron mass and its connection with the colour confinement, as explained in Sec. 4.1.1. At present the valence kaon distribution is nearly unknown and no information exists neither on the kaon sea, nor on the kaon gluon distribution. On the theoretical side, the situation is rapidly evolving: a number of theoretical calculations based on various approaches are now investigating the kaon PDFs, usually as an extension of pion PDFs studies.

The availability of a kaon beam, such as the one foreseen by radio-frequency separation of charged hadrons at the SPS, provides a unique opportunity for performing extensive studies of the kaon partonic structure. The high intensity kaon beam will allow for Drell-Yan measurements with unprecedented statistics. A detailed comparison between the quark structure of the two lightest hadrons becomes possible. The Drell-Yan kaon data should be complemented with J/ψ production and prompt photon measurements, paving the way for a determination of the kaon gluon structure as well.

The RF-separated antiproton beam, on the other hand, makes possible the measurements of nucleon single spin asymmetries with reduced systematic uncertainties. Thanks to charge symmetry, the antiproton induced Drell-Yan process will provide an access to convolutions of valence quark TMD PDFs of the nucleon only. The M2 beam line with RF-separated beam tuned to have high-energy and high-intensity antiprotons would provide the only presently foreseen possibility for such measurements in the world, in a reasonable time scale.

5.3.1 Nucleon spin structure with antiproton beam

The Drell-Yan process using an anti-proton beam on a transversely polarized proton target provides an ideal opportunity to study the transverse momentum dependent PDFs of the nucleon. Compared to the pion-induced Drell-Yan studies being presently performed at COMPASS the uncertainties related to the limited knowledge of pion structure will be eliminated. Additionally, thanks to the boost provided by the high energy collisions on fixed target, an extended x-region is explored, since there is some complementarity of the u-quark TMD PDF covered from target side and from beam side, and as well some overlap.

The antiproton induced Drell-Yan on transversely polarized proton target is the most promising way to access the Boer-Mulders function of the nucleon. In the Drell-Yan cross-section, two transverse spin-dependent modulations can be measured, that result from convolutions of the valence $\bar{u}$-Boer-Mulders function in the antiproton with the valence u-transversity function in the proton ($\cos(2\phi_{CS}+\phi_s)$ modulation) or with the valence u-pretzelosity function in the proton ($\cos(2\phi_{CS}-\phi_s)$ modulation). Given the present knowledge of the u-transversity in the nucleon, extracted from the SIDIS results of the COMPASS and HERMES experiments, one can aim at accessing the u-Boer-Mulders of the nucleon.

As compared to the pion induced Drell-Yan cross-section, the antiproton induced process has larger cross-section. In spite of the beam RF-separation limitations discussed in Sec. 5.1), for the present estimates it is assumed that with additional R&D the beam energy could be increased. Figure 29 compares the Drell-Yan cross-section dependence on the beam energy, for the pion induced and the anti-proton induced cases, emphasysing the advantage of larger beam energies.

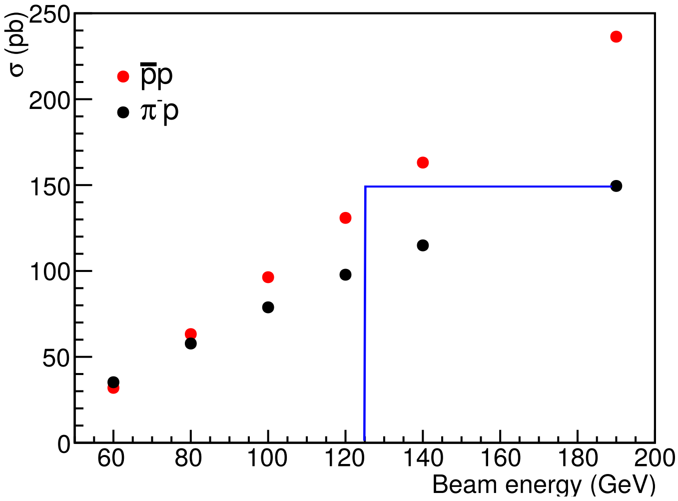

Figure 29: Drell-Yan cross section dependence on the beam energy, for the two cases: negative pion induced and anti-proton induced processes.

For a beam energy of 100 GeV, a Drell-Yan experiment needs to cover angles in the order of 250 mrad in order to have a global geometrical acceptance above 40%, as illustrated in right panel of figure 30.

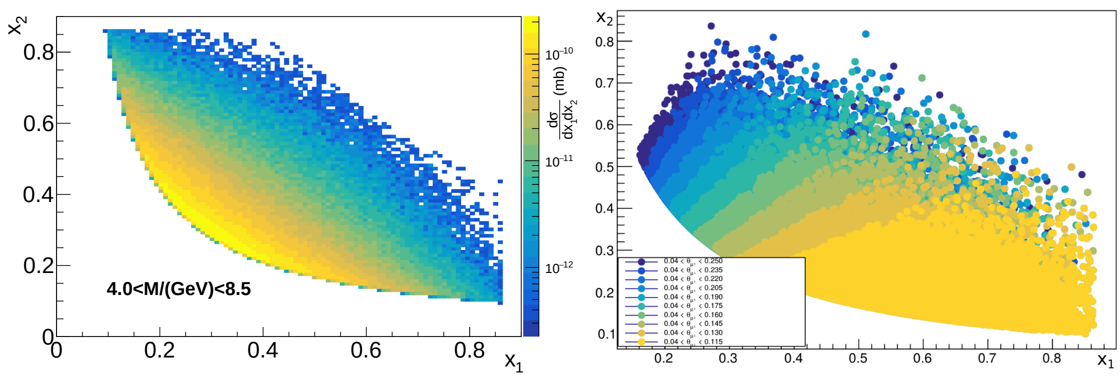

Figure 30: Drell-Yan dimuons cross-section at 100 GeV beam on an NH_3 target of 110 cm. Dimuons with masses 4-8.5 GeV are considered (left). The acceptance of the proposed experiment is also shown.

These simple studies illustrate in an obvious way that a change of paradigm with respect to past Drell-Yan experiments is needed to achieve the large statistics mandatory for azimuthal asymmetry studies. Only a compressed setup allows to reach a coverage of ± 250 mrad. While past experiments could only achieve this by using a hadron absorber, at the cost of dramatically reducing their mass and vertex position resolution, there are now technical solutions that may be explored in an innovative way to reach this purpose. As will be explained in Sec. **??**, a highly segmented active absorber, with embedded magnetic field, may be the ideal device, providing: dielectron tracking, dimuon vertex pointing power, dilepton auto-trigger, and muons momentum measurement all-in-one, for large angle pairs. Layers of magnetised iron with tungsten-silicon detectors sandwished in between them seem a-priori a viable option whose feasibility will be further explored. Simple calculations show that a detector with transverse dimensions of 1.5×1.5 m^2 and 250 cm long could be distanced by 75 cm from the polarized target, still providing ± 250 mrad coverage.

Table 3 gives the achievable statistics for 140 days of beam time on a NH_3 target with the presence of the active absorber.

Experiment	Target type	Beam type	Beam intensity (part/sec)	Beam energy (GeV)	DY mass (GeV/c^2)	DY events $\mu^+\mu^-$	DY events e^+e^-
This exp.	110cm NH_3	$\bar{p}$	3.5×10^7	100	4.0 – 8.5	28,000	21,000
				120	4.0 – 8.5	40,000	27,300
				140	4.0 – 8.5	52,000	32,500

Table 3: Achievable statistics of the new experiment with an active absorber and 140 days of beam time.

5.3.2 *Kaon valence distribution*

The presence of the valence strange quark significantly alters the properties of the kaon in comparison to those of the pion. Being much heavier than the light quarks, it carries a larger fraction of the kaon momentum. Accordingly, the valence distribution in the kaon is expected to be significantly different from that of the pion. At the same Q^2 scale, the $s(x)$ and $u(x)$ valence quark distributions of the kaon are expected to peak to values respectively larger and smaller than that of the pion. The kaon $u(x)$ and $s(x)$ distributions, as calculated in the framework of the Dyson-Schwinger Equations[33] are compared to the pion $u(x)$ distribution in Fig. 31-left. All three PDFs are evaluated at a small, non-perturbative QCD scale and then evolved to 5.2 GeV, a scale typical for fixed-target Drell-Yan experiments.

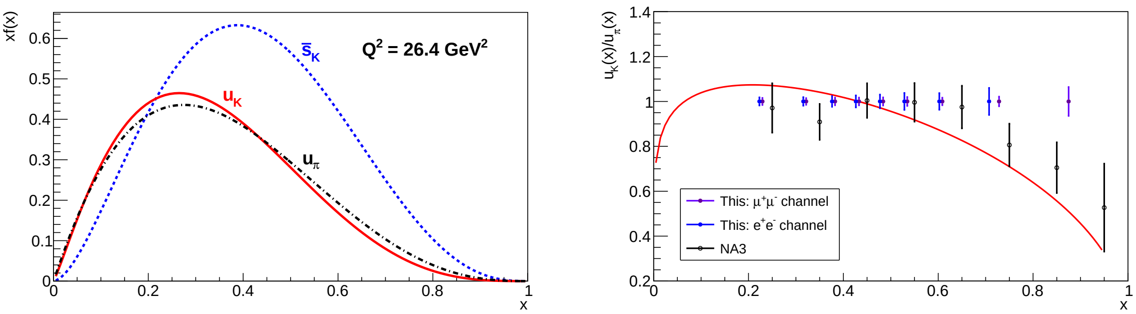

Figure 31: Left: Valence PDFs for the u quark in the pion and u and s quarks in the kaon, following the framework described in Ref. [113]. Right: Projected statistical uncertainties on the kaon to pion Drell-Yan yield ratio in the assumption of a 100 GeV beam and 140 days on a carbon target. The projections are given for two channels and the results are compared to NA3 measurement as well as to the model shown on the left.

Since the u quark valence distribution in the kaon carries a momentum fraction smaller than that of the pion, it should show somewhat faster decrease for large x values. This behaviour is qualitatively confirmed by the first and only available experimental comparison between K^- and π^--induced Drell-Yan measurements [114] by the NA3 collaboration, as shown in the right-hand side of Fig. 31. The NA3 result presented is based on 700 Drell-Yan events produced with kaons in addition to 21000 events produced with pions. The ratio is consistent with unity up to $x_\pi = 0.6$ and start dropping beyond $x_\pi = 0.7$.

The kaon $u(x)$ valence distribution can be determined with a much improved accuracy in a dedicated measurement with the planned RF-separated kaon beam as explained in Sec. 5.1. A 100 cm long carbon target (4×25 cm) is assumed, with a new, large-acceptance, active absorber downstream of it. The active absorber, built to extend a COMPASSlike spectrometer acceptance, is considered to be 250 cm thick, with inner radius of 9 cm and outer one of 135 cm. Assuming 100 GeV hadron beams with an intensity of 7×10^7 parts/second, an unpolarized carbon target, and 2×140 days of data-taking, about 65000 kaon induced Drell-Yan events should be collected in total.

The above mentioned beam flux has a kaon purity of about 30%. An efficiency independent of the beam energy is assumed, which therefore gives more favorable fluxes for higher energies. A reconstruction efficiency, similar for dimuons and dielectrons, of 80% is assumed. For electron-positron pairs, this estimate is based on the AnDY measurements **??**. Table 4 presents a first estimate of the achievable statistics for kaon induced Drell-Yan, in the assumption of equal time sharing between the two beam charges, chosen for a good kaon valence determination. The best time sharing for minimizing the statistical uncertainties on sea-valence separation should be 210 days of K$^+$ and 70 days K$^-$, assuming LO DY cross-section derived from pion induced one, and a K-factor=1.5 to roughly match NA3 observations.

Experiment	Target type	Beam type	Beam intensity (part/sec)	Beam energy (GeV)	DY mass (GeV/c^2)	DY events $\mu^+\mu^-$	e^+e^-
NA3	6cm Pt	K$^-$	????	200	4.2 – 8.5	700	0
This exp.	100cm C	K$^-$	2.1×10^7	80	4.0 – 8.5	25,000	13,700
				100	4.0 – 8.5	40,000	17,700
				120	4.0 – 8.5	54,000	20,700
		K$^+$	2.1×10^7	80	4.0 – 8.5	2,800	1,300
				100	4.0 – 8.5	5,200	2,000
				120	4.0 – 8.5	8,000	2,400
This exp.	100cm C	π^-	4.8×10^7	80	4.0 – 8.5	65,500	29,700
				100	4.0 – 8.5	95,500	36,000
				120	4.0 – 8.5	123,600	39,800

Table 4: Achievable statistics of the new experiment, assuming 2×140 days data-taking with equal time sharing between the two beam charges. For comparison, the collected statistics from NA3 is also shown.

The Drell-Yan production of negative kaons and pions will be measured simultaneously. Taking the ratio of kaon to pion yields will reduce systematical uncertainties. Within small corrections for the sea-valence contributions, the kaon to pion ratio is proportional to the ratio between their respective $u(x)$ distributions. The projected accuracy of this ratio is shown in right panel of Fig. 31.

5.3.3 Kaon valence-sea separation

The kaon sea distribution is presently unknown. It can only be determined through a comparison between positive and negative kaon induced Drell-Yan measurements. In such measurements, the K^+ cross section is sensitive to sea-valence and sea-sea terms only, so the difference between K^- and K^+ beams is sensitive to valence-valence terms only. With an isoscalar light target one can define [115] the sea to valence ratio $R_{s/v}$ as:

$$\Sigma_{val} = \sigma^{K^-A} - \sigma^{K^+A} \tag{13}$$

$$R_{s/v} = \sigma^{K^+A} / \Sigma_{val} \tag{14}$$

Figure 32 shows the computed $R_{s/v}(x)$ ratio using three different assumptions for the amount of kaon sea, and for three possibilities of kaon beam energy. Since kaon sea distributions are not available, the parametrisations of Ref. [42] for the pion have been used with the appropriate changes. The three distributions were obtained imposing sea quark momentum contributions between 10% and 20%. For $x_K = 0.4$ the difference between the two extreme values of the sea contribution reaches about 25%. With decreasing x_K the difference increases, by an approximate factor of 1.6 at $x_K = 0.2$. Three different kaon beam momenta are represented, the largest one corresponding to the most favorable from the physics point of view, but requiring additional R&D.

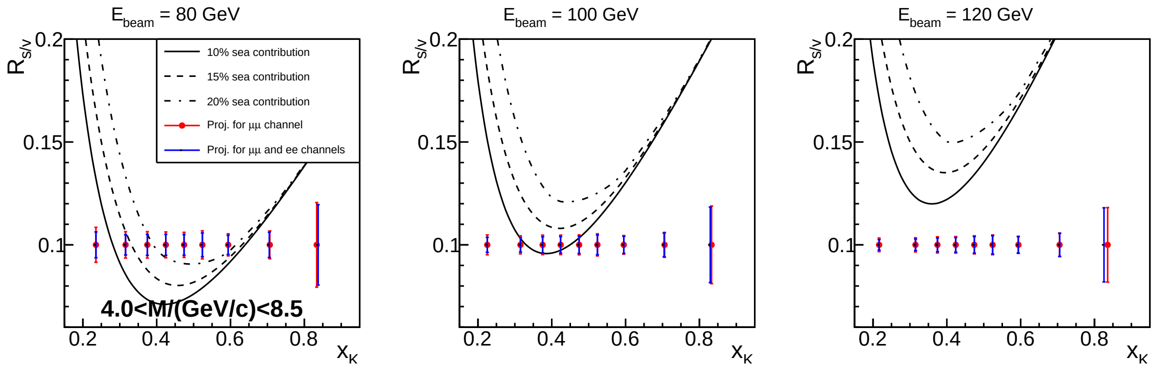

Figure 32: $R_{s/v}$ as a function of x$_K$ is shown for three hypotheses of the kaon beam momentum. The projected statistical uncertainties of the proposed experiment are compared to the sensitivity of $R_{s/v}$ to the kaon sea quark content. The three curves representing 10%, 15%, and 20% of kaon momentum carried by sea quarks are derived from SMRS pion PDFs by interchanging d-quarks with s-quarks.

5.3.4 The J/ψ production mechanism and the gluon distribution in the kaon

The heavier quark in the kaon radiates less gluons than the lighter quarks in the pion. A natural consequence of this expectation is that the gluons in the kaon carry less momentum than the gluons in the pion. Using the Dyson-Schwinger Equation (DSE) approach, the authors of Ref. [33] find that at the hadronic scale the gluons contribute to only 5% of the total momentum in the kaon, instead of about 1/3 for the pion. A stringent check of this prediction requires the measurement of the presently unknown kaon gluon distribution.

The gluon distribution in the kaon can in principle be inferred through a measurement of the kaon-induced J/ψ production. An important advantage of this process is its large cross section, reaching 100 nb/nucleon for small values of x_F, as compared to fraction of nb/nucleon for the high-mass Drell-Yan region at the fixed target energies available at the CERN SPS. As discussed in Sec. 4.1.3 the J/ψ production is not well understood. For fixed-target energies, the simple Color Evaporation Model (CEM) does not agree with the more thorough NRQCD approach, and the relative contributions of the gg fusion and $q\bar{q}$ annihilation terms depend on the model considered [53]. In both models the gg component is larger at small x_F, whereas the $q\bar{q}$ term is dominant at large x_F, although with somewhat different intensities.

Here, the availability of the two different kaon beam charges can greatly help. A comparison between cross sections measured with the two beam charge signs can be used to both improve our understanding of the J/ψ production mechanism and to infer the gluon distribution in the kaon. Indeed, the J/ψ cross section for the positive kaon beam is different from the one for the negative kaon beam. The main difference comes from the valence $\bar{u}$ quark in the negative kaon, which annihilates the valence u quark in the target. In contrast, there are no valence $\bar{u}$ quarks in the positive kaon. Therefore, the $q\bar{q}$ term is solely generated from the valence-sea and sea-sea contributions; those terms contribute an order of magnitude less to the $q\bar{q}$ annihilation term. The valence strange quark in the kaon is also suppressed, as there are no valence strange quarks in the target. A comparison between the positive and negative kaon-induced cross sections for J/ψ production on a ^{12}C target, as calculated in LO CEM, is shown in Fig. 33. While the gg term is identical for both kaon charges, the $q\bar{q}$ terms differ by more than a factor of three.

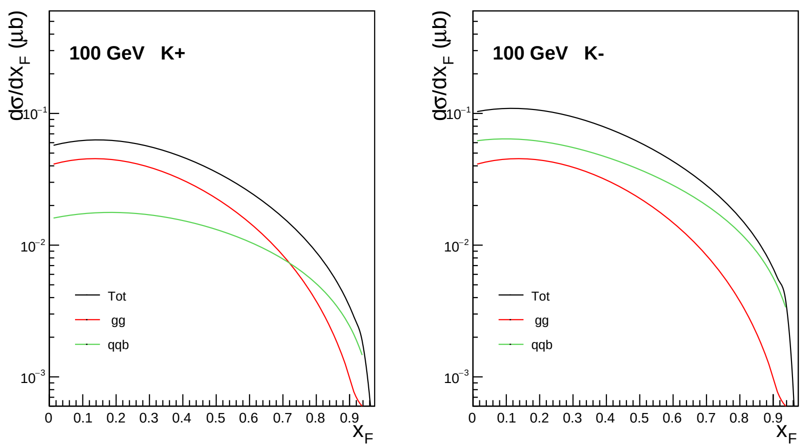

Figure 33: Differential cross section as function of x_F, as obtained in the Color Evaporation Model, on a ^{12}C target for kaon-induced J/ψ production with 100 GeV positive kaon beam (left) or negative kaon beam (right).

Since the gg contributions for both K$^-$ and K$^+$ beams are the same, the difference between the K$^-$ and K$^+$-induced J/ψ cross sections is then equal to the $\bar{u}u$ valence-valence term:

$$\sigma_{J/\psi}^{K^-} - \sigma_{J/\psi}^{K^+} \propto \bar{u}^K u^N \tag{15}$$

In the difference, the identical gg contributions from the positive and negative kaon beams cancel. All other sea-valence, valence-sea, and sea-sea terms are also identical and cancel as well. The difference from the two cross sections thus provides an alternative way for accessing the $u(x)$-quark valence distribution in the kaon, after unfolding the well known $u(x)$ distribution in the nucleon target. This determination of the kaon valence density can then be compared to the valence density determined using the Drell-Yan process. Both Drell-Yan and J/ψ production methods could be used simultaneously to minimize any model dependencies in the extraction.

An unambiguous determination of the $q\bar{q}$ annihilation term through a measurements of the K$^-$ vs K$^+$ difference also gives access to the remaining gg contribution, within a given model. The gg term is a convolution of the well-known gluon distribution of the nucleon and the gluon distribution in the kaon, and will open a way to determining the kaon gluon distribution.

5.3.5 Comparison with experimental efforts elsewhere

The interest for an improved understanding of the kaon structure is rapidly rising. Experiments dedicated to the measurement of the kaon valence structure are planned [116**?**], based on the validity of the meson-cloud model. The JLab experiment plans to cover the x_K region between 0.4 and 0.95 . The kaon structure studies will be extended to lower x_K values at the forthcoming Electron Ion Collider. For both these experiments, at JLab and at EIC, the interpretation of their future kaon data strongly relies on a model-dependent kaon flux determination. The proposed kaon induced Drell-Yan measurement does not suffer from these limitations and is therefore a much more direct way to access kaon structure.

Secondary kaon and antiproton beams are also under preparation at the JPARC facility in Japan. These JPARC beams are expected to reach intensities of up to 10^6 particles/second for incident momenta of up to a maximum of 15 GeV/c. Because of the lower momenta and intensity, no future experiment at JPARC can be competitive with the proposed studies of the meson and nucleon structure.

5.3.6 Run Plan: physics goals and required beam time

There is presently no planned facilities in the world providing high energy and high intensity kaon and antiproton beams. Although the RF-separation project at CERN is unique, the technique it is based on is known and used since some time.

The possibility to use a RF-separated beam can only be considered after the long CERN shutdown LS3. With the technologies presently available, kaon and antiproton beams of momenta up to 80 and 100 GeV respectively could be envisaged. But further R&D might increase those limits, with obvious advantages to the physics case here presented.

The longer time-scale before the start of this phase allows to envisage an ambitious development at the level of the spectrometer itself. A detector joining calorimetry and tracking, embedded in a magnetic field providing momentum measurement, which in itself behaves as active absorber, is being considered. Such detector would provide the largest geometrical acceptance ever achieved in a fixed target Drell-Yan experiment.

A nominal kaon beam intensity of 2.10^7 kaons/second and a 100 cm long carbon target about 40 000 negative kaon DY events could be collected in one year of data taking, and a number of J/ψ events above 1 million. An additional year with positive kaon beam would allow for sea-valence separation in the kaon.

The antiproton Drell-Yan measurement requires one more year of data-taking. Considering a 100 GeV beam with intensity of 3.5×10^7 antiprotons/second, and a polarized NH_3 target 110 cm long, some 50,000 Drell-Yan events could be collected, allowing for transverse spin asymmetry studies of the nucleon, independent from the knowledge of the pion structure.

5.4 Study of gluon distribution in kaon via prompt photon production

5.4.1 Gluon PDFs for mesons

Recent progress in theoretical calculations (see Sec. 4.1.1 and 5.3) makes the gluon distributions in the pion and the kaon especially important. Gluons not only significantly contribute to the internal structure of the mesons; they also play a major role in the generation of their mass [117]. The available experimental information is however severely limited. In contrast to the rather well mapped out gluon distribution in the nucleon, the gluon content of the mesons is essentially unknown. The planned RF-separated beams facility at CERN provides a unique opportunity for dedicated measurements of the two lightest meson gluon distributions.

In order to measure the gluon PDFs for the pion the next hard processes were used: i) J/ψ, Υ-states production; ii) dijet production in gg and qg scattering; and iii) prompt photon production in the gluon Compton scattering. The first method assumes that quarkonia production mainly proceeds through gluon fusion into quark-antiquark pairs. It is affected by uncertainties related with the accounting for other production mechanisms. The second approach requires energetic meson beam, has low sensitivity and its systematics is defined by the knowledge of fragmentation functions. As for the third method, the cross section of prompt photons production is known at least up to the NLO [125]. Systematics of this method is mainly defined by experimental conditions and its dependence on the model assumptions is minimal.

5.4.2 Prompt photons

Prompt photons are photons produced in the hard scattering of partons. According to the factorization theorem the inclusive cross section for production of a prompt photon in a collision of hadrons h_A and h_B can be written as follows:

$$d\sigma_{AB\to\gamma X} = d\sigma_{dir} + d\sigma_{frag} = \sum_{a,b=q,\bar{q},g} \int dx_a dx_b f_a^A(x_a,Q^2) f_b^B(x_b,\mu^2) d\sigma_{ab\to\gamma x}(x_a,x_b,Q^2) + d\sigma_{frag}. \quad (16)$$

Here $d\sigma_{dir}$ is the contribution of photons emitted via direct coupling to a quark (direct photons) and $d\sigma_{frag}$ represents the contribution of photons produced from the fragmentation of a final partonic state (fragmentation photons). f_a^A (f_b^B) is the parton density for hadron h_A (h_B), x_a (x_b) is the fraction of the momentum of hadron h_A (h_B) carried by parton a (b) and Q^2 is the square of the 4-momentum transferred in the hard scattering process. $\sigma_{ab\to\gamma x}(x_a, x_b, Q^2)$ represents the cross section for the hard scattering of partons a and b. Contribution of fragmentation photons in the discussed kinematic range does not exceeds $10-20\%$ even for much higher energies [126] and can be taken into account. There are two main hard processes causing the production of direct photons: i) gluon Compton scattering $gq(\bar{q}) \to \gamma q(\bar{q})$ (dominating) and ii) quark-antiquark annihilation $q\bar{q} \to \gamma g$. Measurement of the differential cross section of the prompt photon production $Ed^3\sigma/dp^3$ in the pion-nucleon collisions was already used by the fixed target experiments WA70 [45], E706 [127], etc. for determination of the pion gluon structure.

5.4.3 *Prompt photon production at COMPASS*

In order to determine the gluon structure of charged kaon we propose to measure the differential cross section of the prompt photon production $Ed^3\sigma/dp^3$ in the kinematic range of the transverse momentum $p_T > p_{T0} = 2.5$ GeV/c and the CMS rapidity $-1.4 < y < 1.8$ using a positive kaon beam of 100 GeV/c ($\sqrt{s} = 13.7$ GeV). This range corresponds to $x_g > 0.05$ of the kaon beam and $Q^2 \sim p_T^2$. The corresponding kinematic distribution for $x_T = 2p_T/\sqrt{s}$ vs y for the gluon Compton scattering process, the kinematic ranges covered by previous low-energy pion beam experiments and possible kinematic region for COMPASS are shown in Fig. 34a (according to [128]).

A positive beam is chosen in order to reduce the number of prompt photons produced via $q\bar{q}$ annihilation. Auxiliary data sample should be collected with a negative kaon beam in order to separate the gluon Compton scattering and quark-antiquark annihilation production mechanisms. The data taking with a kaon beam should be preceded by one year of data taking with a pion beam at similar conditions or the pion component of the RF-separated beam could be used in the case of its sufficiency. Pion data will be used for refinement of the pion gluon structure and for the study of systematic effects.

The contribution of the gluon Compton scattering to the cross section $\sigma_{AB\to\gamma X}$ calculated under the LO approximation (Pythia6) in the kinematic range that is mentioned above for the 100 GeV/c pion beam, which interacting with a proton target, is 53 nb. The corresponding contribution of the quark-antiquark annihilation process is 6 nb and 42 nb for the positive and negative beams, respectively. Similar magnitudes of the cross sections could also be expected for a kaon beam of the same momentum. Figure 34b represents energy dependence of the prompt photon production cross section for $p_T > p_{T0}$=2.5 GeV/c for both production mechanisms for positive and negative kaon beams under assumption $g_\pi(x, Q^2) = g_K(x, Q^2)$.

The main contribution to a systematic uncertainty which dominates over a statistical error is expected to originate from the estimation of the number of photons produced from decays of secondary π^0 and η mesons (minimum bias photons). This kind of the background is especially important at small p_T and defines the lower limit of the accessible p_T range. p_T distributions for gluon Compton scattering photons and for minimum bias photons are shown in Fig. 35. Value of p_{T0} was assumed on the ground of the experience of previous experiments at similar $\sqrt{s}$. Limited spatial resolution of electromagnetic calorimeters could lead to misidentification of a cluster produced by both photons from decay of an energetic π^0 as a single photon cluster. This effect becomes significant at high p_T. Background form 2γ decays of π^0 and η can be reduced by reconstruction of such decays. Final subtraction of this background is based on the precise Monte-Carlo simulation of the setup. Detection of a photon produced much upstream the target and mis-association of such photon with the interaction in the target may also lead to significant overestimation of its p_T.

For effective study of prompt photon production the following requirements should be fulfilled.

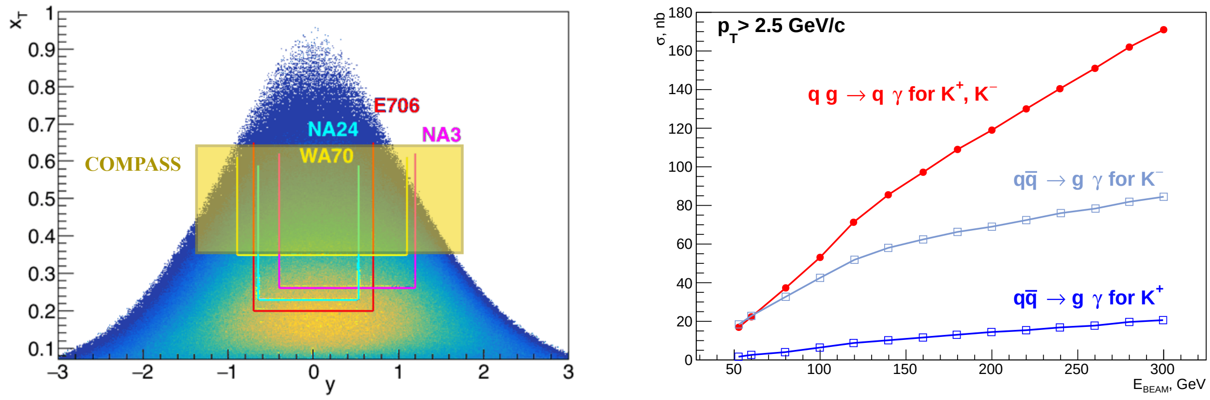

Figure 34: a) Kinematic distribution for $x_T = 2p_T/\sqrt{s}$ vs y for the gluon Compton scattering process for a 100 GeV K^+ beam scattered off a proton target. The kinematic ranges covered by previous low-energy pion beam experiments and possible coverage of COMPASS are also shown in different colors. b) Energy dependence of the prompt photon production cross section for p_T >2.5 GeV/c for both production mechanisms for positive and negative kaon beams under assumption $g_\pi(x,Q^2) = g_K(x,Q^2)$.

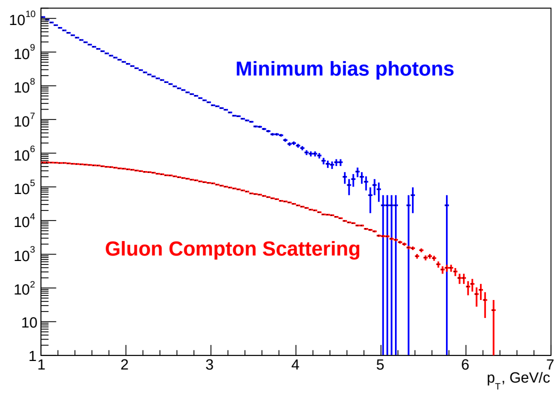

Figure 35: p_T distributions for prompt photons from the gluon Compton scattering (red) and for minimum bias photons (blue) produced in the interaction of a 100 GeV K$^+$ beam and a proton target (according to Pythia6 and assumed that $g_\pi(x,Q^2) = g_K(x,Q^2)$). Distributions are normalized to one year of data taking. For the prompt photons the K-factor 1.4 is taken into account.

– The positive kaon beam of 100 GeV/c or higher momentum and intensity of 2×10^7 kaons per second should be delivered to the experimental area.

– The CEDAR detectors should be used for rejection of events produced by beam particles different from the kaons.

– A two meters long liquid hydrogen target ($\sim$0.2 X_0), transparent for produced photons, should be used. A solid target of low-Z material could also be discussed.

– The existing electromagnetic calorimeters, ECAL0 and ECAL1, can provide sufficient capability for detection of prompt photons in the rapidity range $-1.4 < y < 0.4$ and $-0.2 < y < 1.8$ respectively (see Fig. 36a). They have to be included into dedicated triggers. The ECAL2 calorimeter should play an important role in the π^0 background subtraction.

– A stainless still shielding is required to be installed upstream the target to prevent illumination of the calorimeters by photons produced in the interaction of beam kaons with beam part elements of the setup.

– A tracking detector (X and Y planes) with aperture of about 2.3×2.3 m^2 and the beam hole 0.5×0.5 m^2 should be installed in front of the ECAL0 in order to provide capability to identify "charged" clusters in the ECAL0 and reject charged particles with high p_T. Spatial resolution of the detector is defined by the ECAL0 cell size (3.8 cm) and should be of about 1 cm.

– Transparency of the setup should be increased in order to reduce the number of secondary photons.

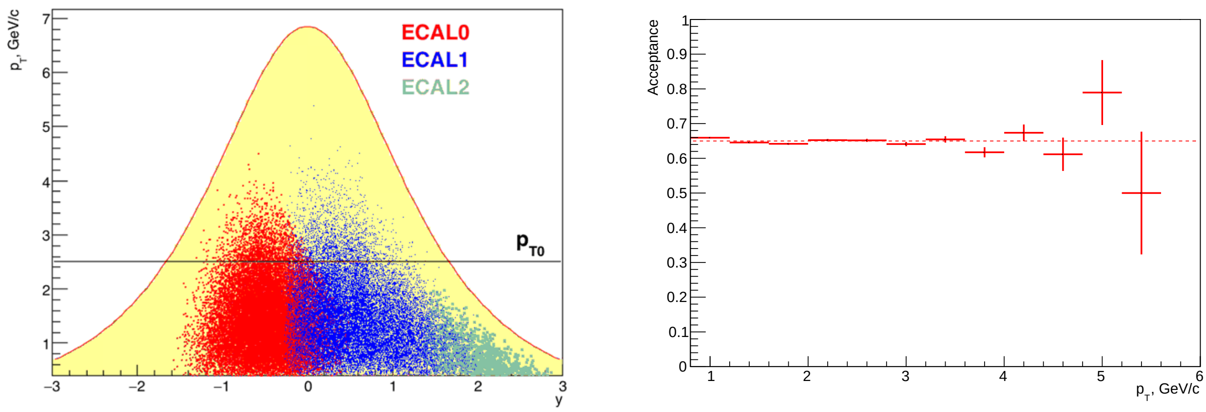

Figure 36: a) Kinematic range in the rapidity y and the transverse momentum for prompt photons produced in the gluon Compton scattering. Regions covered by the electromagnetic calorimeters ECAL0, ECAL1 and ECAL2 are shown in red, blue and green, respectively. The COMPASS setup for GPD run (2017) is used. b) Acceptance of the COMPASS setup used for the GPD run in 2017 for prompt photons as a function of their transverse momentum p_T.

Acceptance of the COMPASS setup used for the GPD run in 2017 for prompt photons as a function of transverse momentum p_T is shown in Fig. 36b. The detector geometry, material map and minimal thresholds for cluster energy in ECAL0, ECAL1 and ECAL2 on the level 0.5 GeV, 1 GeV and 2 GeV, respectively, are taken into account. The acceptance is rather flat up to very high p_T and is about 0.65.

Prompt photon production rate estimation is based on the next assumptions: period of data taking is 140 days with the accelerator efficiency of 0.8 that corresponds to the integrated flux 2×10^{13} kaons delivered to the 2 m long liquid hydrogen target; LO gluon Compton scattering cross section is the LO cross section with the K-factor 1.4, is 74 nb (for $p_T > 2.5$ GeV/c); duty factor of the detector is 0.9; general acceptance (including geometry, photon conversion and selection criteria) is 30%. Thus the expected statistics of gluon Compton scattering events in the kinematic range $p_T > 2.5$ GeV/c and $-1.4 < y < 1.8$ is 3.4×10^6 events.

5.4.4 Worldwide competition

At the moment there are no announced plans to study the gluon structure of charged kaons.

5.5 Primakoff Reactions

5.5.1 Kaon polarizability

The electric (α) and magnetic (β) polarizabilities characterize the meson in terms of its interaction as a complex QCD system with an external electromagnetic field and can be probed in the Conpton scattering.. They are fundamental parameters of meson physics, and provide a possibility to compare

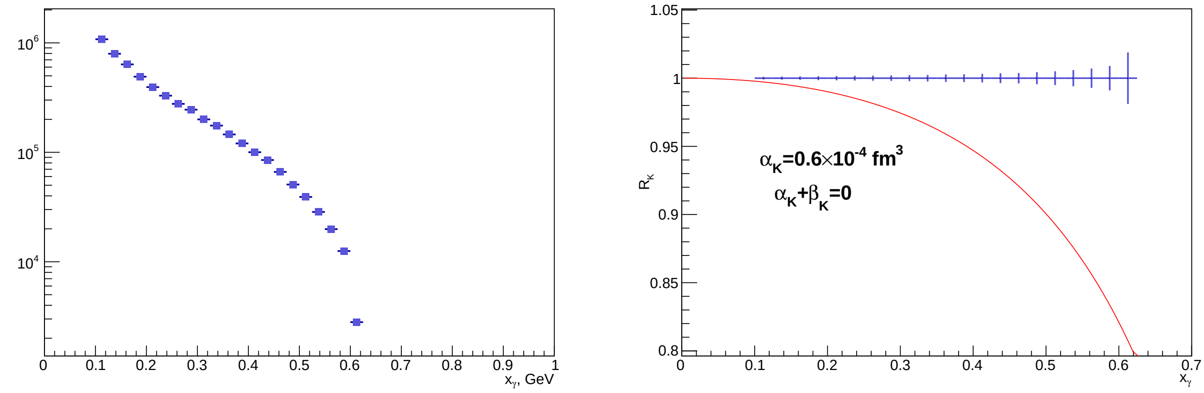

Figure 37: a) The expected x_γ spectrum for $K^-\gamma$ events. b) The statistical accuracy for the measurement of the ratio R_K of the differential cross-section for the real kaon over the expected cross-section for a hypothetical point-like kaon as a function of x_γ. The ratio R_K corresponding to the χPT prediction is shown in red.

experimental results with theoretical predictions. The polarizabilities of the charged pion predicted by chiral perturbation theory (χPT) in the two-loop approximation are $\alpha_\pi - \beta_\pi = (5.7 \pm 1.0) \times 10^{-4}\,\mathrm{fm}^3$ and $\alpha_\pi + \beta_\pi = 0.16 \times 10^{-4}\,\mathrm{fm}^3$ [129]. The currently most precise measurement of the pion polarizability is $\alpha_\pi = (2.0 \pm 0.6_{stat} \pm 0.7_{syst}) \times 10^{-4}\,\mathrm{fm}^3$, which is in agreement with the predictions of χPT [129, 132]. This result was obtained by the COMPASS experiment in the so-called Primakoff reaction $\pi^- Z \to \pi^- \gamma Z$ with $190\,\mathrm{GeV}/c$ negative pion beam under the assumption $\alpha_\pi + \beta_\pi = 0$ [23].

For the kaon, since it is a more compact and rigid object than the pion, the naive expectation is to observe smaller values for the polarizabilities. Indeed, the χPT prediction for the charged kaon polarizability in one-loop approximation is $\alpha_K = (0.64 \pm 0.10) \times 10^{-4}\,\mathrm{fm}^3$ under the assumption that $\alpha_K + \beta_K = 0$ [130]. The quark confinement model predicts values of $\alpha_K = 2.3 \times 10^{-4}\,\mathrm{fm}^3$ and $\alpha_K + \beta_K = 1.0 \times 10^{-4}\,\mathrm{fm}^3$ [131]. As for an experimental validation, only an upper limit $\alpha_K < 200 \times 10^{-4}\,\mathrm{fm}^3$ (CL=90%) has been established from the analysis of X-rays spectra of kaonic atoms [133].

A measurement of the kaon polarizability via the reaction $K^- Z \to K^- \gamma Z$ — similar to the measurement of the pion polarizability performed by COMPASS — is challenging to prepare. The kaon component in a conventionally produced hadron beam is too small at high beam energies, to collect the required amount of data on a reasonable timescale. Also the identification of the beam particles with a high enough purity is challenging. To this end, an RF-separated hadron beam, in which kaons have been enriched, would provide an unique opportunity to perform the first measurement of the kaon polarizability. Additional difficulties for the kaon polarizability measurement are the small kinematic gap between the threshold in the invariant mass $M_{K^-\gamma}$ and the first resonance K$^*(892)$ in respect to the pion case (with $\rho(770)$ resonance) and one order of magnitude smaller Primakoff cross section than the one for the pion.

For the kaon polarizability measurement with a $100\,\mathrm{GeV}/c$ RF-separated kaon beam we assume the next conditions:

– the basic spectrometer configuration as it was used in 2009 and 2012 for the analogous measurements with the pion beam: the CEDAR detector on the beam line, a 0.3 X_0 thick nickel target, silicon-based telescopes up- and downstream the target, similar dead time of trigger and DAQ);

– trigger on the high-energy deposition the ECAL1 and ECAL2 calorimeters;

– the new DAQ system with capability to accept trigger rate up to 100 kHz.

Assuming an integrated flux 2×10^{13} kaons after one year of data taking, we estimate the achievable statistics to be of about 2.4×10^{6} $K^{-}\gamma$ events in the kinematic range $0.1 < x_{\gamma} < 0.6$ and $M_{K^{-}\gamma} < 0.8\,\mathrm{GeV}/c^{2}$. Here, x_{γ} is the energy of a produced photon normalized to the beam energy. The trigger efficiency is supposed to be close to 100% in the whole range of x_{γ}. The expected x_{γ} spectrum of $K^{-}\gamma$ events is shown in Fig. 37a. The ratio R_K of the differential cross-section for the kaon over the expected cross-section for a hypothetical point-like kaon as a function of x_{γ} under assumption $\alpha_K + \beta_K = 0$ can be approximately expressed as

$$R_K = 1 - \frac{3}{2} \cdot \frac{x_{\gamma}^{2}}{1 - x_{\gamma}} \cdot \frac{m_K^{3}}{\alpha} \cdot \alpha_K^{3}, \tag{17}$$

where α is the fine structure constant. It is important to emphasize that polarization effects in case of the kaon are amplified by the factor of $(m_K/m_{\pi})^{3} \approx 44$ in respect to the pion. The statistical accuracy for the measurement of the ratio R_K of the differential cross-section for the kaon over the expected cross-section for a hypothetical point-like kaon as a function of x_{γ} is presented in Fig. 37b. The expected ratio R_K corresponding to the χPT prediction is also shown. The statistical accuracy of the α_K extraction under the assumption $\alpha_K + \beta_K = 0$ is $0.015 \times 10^{-4}\,\mathrm{fm}^{3}$. As for the systematic uncertainty, the main contributions are expected from (i) uncertainty of the determination of the tracking detector efficiency from the Monte Carlo simulation; (ii) statistical uncertainty of the π^{0} background subtraction; (iii) effect of the uncertainty on the estimate of strong interaction background and its interference with the Coulomb contribution; (iv) uncertainty of $\pi\gamma$ events subtraction due to a pion contamination in the beam. The statistical uncertainty is expected to be smaller than the statistical one.

We are not aware of any other plans to measure the charged kaon polarizability.

6 Instrumentation

Many programs introduced in this Letter of Intent are based on the concept of using the basic features of the present COMPASS setup [?], [?]: one or two large-gap dipole magnets with tracking stations around them, combined with particle identification detectors. The standard polarized target is described in Ref. [?] and the liquid hydrogen (LH2) target in Ref. [?].

Most future programs require additional specific detectors or other equipment, as explained in the text (Sec. 6.1 for general upgrades and Sec. 6.2 for specific upgrades). The CEDARs, located at the beam line, are necessary for all hadron programs for beam-particle identification. The RICH is necessary for several programs for the separation of produced hadrons.

Some of the programs plan the use of the existing M2 muon or hadron beams, while other programs are designed for future RF-separated hadron beams in the M2 beam line with enhanced fractions of kaons and antiprotons (Sec. 5.1).

The specific parameters and hardware upgrades for each program are summarized in Tab. 5.

Program	Beam Energy [GeV]	Beam Intensity [/s]	Trigger Rate [kHz]	Beam Type	Target	S?	Hardware Additions	R?	C?
Proton radius	100	$4 \cdot 10^6$	100	$\mu^\pm$	high-pr. H2	$\times$	active TPC, SciFi trigger, silicon veto		
GPD E	160	10^7	10	$\mu^\pm$	NH3↑	$\times$	recoil silicon, modified PT magnet		
Anti-matter	190	$5 \cdot 10^5$	25	p	LH2, LHe	$\times$	recoil TOF	$\times$	$\times$
Spectroscopy $\overline{p}$	12, 20	$5 \cdot 10^7$	25	$\overline{p}$	LH2		target spectrometer: tracking, calorimetry	$\times$	$\times$
Drell-Yan conv	190	$7 \cdot 10^7$	25	$\pi^\pm$	C/W	$\times$	vertex detector		$\times$
Drell-Yan RF	$\sim$100	10^8	25-50	$K^\pm, \overline{p}$	6LiD↑, C/W		”active absorber”, vertex detector		$\times$
Primakoff	$\sim$100	$5 \cdot 10^6$	> 10	K^-	Ni	$\times$		$\times$	$\times$
Prompt photon	100	$5 \cdot 10^6$	10-100	K^+	LH2	$\times$	hodoscope		$\times$
Spectroscopy K^-	50-100	$4 \cdot 10^6$	25	K^-	LH2	$\times$	recoil TOF	$\times$	$\times$

Table 5: Requirements for the future programs at the M2 beam line after 2021. “[GeV]” indicates the beam energy, “[kHz]” the estimated trigger rate. “Rate” refers to the beam-particle rate on the target. Standard muon beams are in blue, standard hadron beams in orange, and RF-separated hadron beams in red. “S” refers to standard COMPASS spectrometer setup, “R” to RICH-1 and if possible RICH-0, and “C” to CEDARs.

6.1 General upgrades

The following general upgrades of the COMPASS apparatus are considered:

– A new type of front-end electronics (FEE) and trigger logic that is compatible with triggerless readout including an FPGA-based TDC with time resolution down to 100 ps and digital trigger, capable of trigger rates up to 90-200 kHz (Sec. 6.1.1).

– New large-size PixelGEMs as replacement and spares for aging large-area GEMs (Sec. 6.1.2).

– New large-area multi-pattern gaseous detectors (MPGD) based on GEMs or MicroMega technology to replace aging MWPCs (Sec. 6.1.3).

– High-rate-capable CEDARs (Sec. 6.1.4) for all hadron-beam programs to identify the desired beam particle.

– The existing RICH-1 will be required by the spectroscopy programs (Secs. 4.2 and 5.2), the anti-matter cross section measurement (Sec 4.3), and the Primakoff program (Sec. 5.5). A high-aperture RICH-0 would be desirable for these programs in order to separate hadrons at lower momenta (Sec. 6.1.5).

6.1.1 Front-end Electronics and DAQ

The goal of the front-end electronics and data-acquisition system is the read out detectors with best precision and minimum loss of efficiency. With particle rates on the target of up to 10^8/sec, the optimum solution is the construction of triggered, pipelined front-end electronics with maximum trigger-rate capability between 100 and 200 kHz and dead time of 2-3 %. These requirements allow the usage of the well-performing APV25 ASIC for all micro pattern gas and silicon detectors, as well as for the RICH detector. Since many modern ASICs feature triggerless readout, the desired goal of a triggerless readout solution exists for every detector type. The newly developed FPGA-based TDC (iFTDC) has a time resolution down to 100 ps. It is planned to equip all detectors with new modern FEE and to use the same kind where possible. This will allow a single expert to intervene on various equipments.

The architecture of the readout system is shown in Fig. 38. The number of channels and the data rates are estimated using the performance of the COMPASS setup and COMPASS DAQ [134]. The front-end boards including digitizers will be placed near the detectors and will be equipped with two high-speed serial interfaces. One interface will transmit untriggered hit information and can be connected to the digital trigger module. The second link will transmit triggered information only to the DAQ. All high-speed serial interfaces within the DAQ and digital trigger will employ the UCF protocol [135], which features to transmit trigger and event identification information, slow control messages, and data via single serial link.

The DAQ will consist of two stages of data processing. At the first stage, the data will be buffered at the local SDARM and then merged into sub-events. At the second stage, complete events will be assembled and distributed between online PCs via 10 Gb Ethernet. The maximum data rate expected during a spill will be 5 GB/s, while the sustained rate will be 2 GB/s. The system is designed to handle sustained-data rates of 5 GB/s.

6.1.2 Large-area PixelGEM detectors

New large-area PixelGEM detectors will be designed and ten such detectors will be built by 2021 as replacement and spares for the existing large-area GEMs [**?**] in the COMPASS setup. Each detector will have 4,096 channels. The periphery will be read out with strip readout from both sides. The center will consist of hexagonal pads of 1.5 mm outer radius and will be equipped with pixel readout. The active area of each detector will be between 30.7 cm × 30.7 cm and up to 40 cm × 40 cm, about a factor of 10 larger than the existing COMPASS PixelGEM detectors [**?**]. The new PixelGems will be equipped with new Front-End Electronics allowing for higher rates and self-triggering.

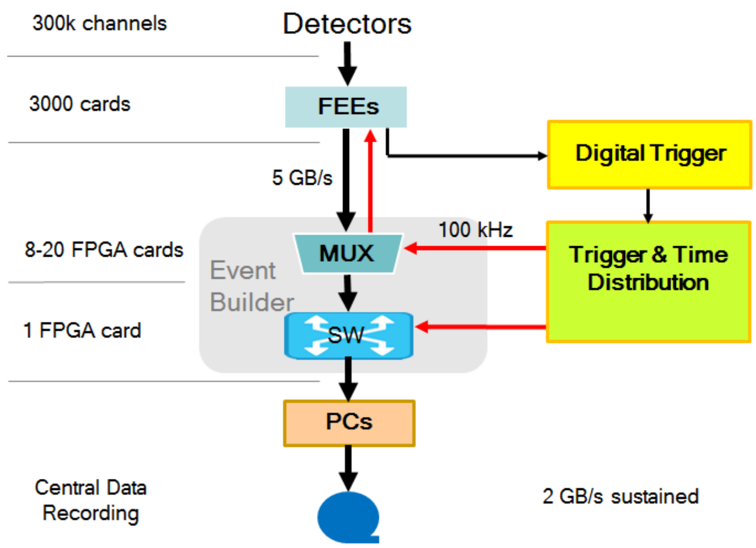

Figure 38: The DAQ architecture of the new experiment.

6.1.3 Large-area multi-pattern gaseous detectors (MPGD)

New MPGDs will be designed and developed to replace the existing ageing 14 MWPC tracking stations in the COMPASS setup. The new detectors will be based on large-area GEM or MicroMega technology. Each station will have an active area of $\sim$1.5 m^2 , with two or three coordinates planes and $\sim$2 mm pitch. The new detectors will be equipped with a new front-end electronics with a rate capability of $\sim$1 MHz per channel. The total number of channels will be about 28,000.

6.1.4 CEDARs at high rates

The purpose of the CEDAR is the identification of the beam particle on an event-by-event basis. Two 6 m-long CEDAR stations are located in the M2 beam line 30 m upstream of the COMPASS target. They are filled with helium gas at a pressure of approximately 10.5 bar. The emerging Cherenkov photons are focused by a mirror and detected by eight PMTs arranged in a ring around the center. The pion, kaon, or proton ring is selected by tuning the diaphragm and the pressure.

The existing CEDARs are in winter 2017/2018 being upgraded for better rate- and thermal stability in preparation of the 2018 COMPASS pion-beam run. The project is carried out in collaboration of CERN and representatives from COMPASSṄew PMTs (fast Hamamatsu R11263-203 with pulses width of 2-3 ns), a new gain monitoring system, a new readout system, and a new thermalization system are contained in the upgrade package. A conceptual sketch of the upgraded system is shown in Fig. 39.

The decision whether further upgrades of the CEDAR system will be necessary during LS2 for the future hadron-beam programs (as described for standard beams in Sec. 4 and for RF-separated beams in Sec. 5 will be based on the experience collected with the upgraded CEDARs during the 2018 COMPASS Drell-Yan run with high-intensity pion beam ($\sim 8 \cdot 10^7$/sec. The possibility of a tracking system for the CEDARs is considered that would correct the beam-track trajectories. One option could be the XBPF upgrade, a new SciFi-based instrumentation developed at the CERN North Area to measure beam profiles and momenta [**?**].

6.1.5 Hadron PID perspectives: RICH

RICH-1 [136] [137] [138] [139] is the backbone for hadron PID in the COMPASS setup. RICH-1 is a large acceptance ($\pm$200 mrad in the vertical plane, $\pm$250 mrad in the horizontal plane) Cherenkov imaging counter using C4F10 as heavy and low-chromaticity radiator gas, where image focalization is provided by

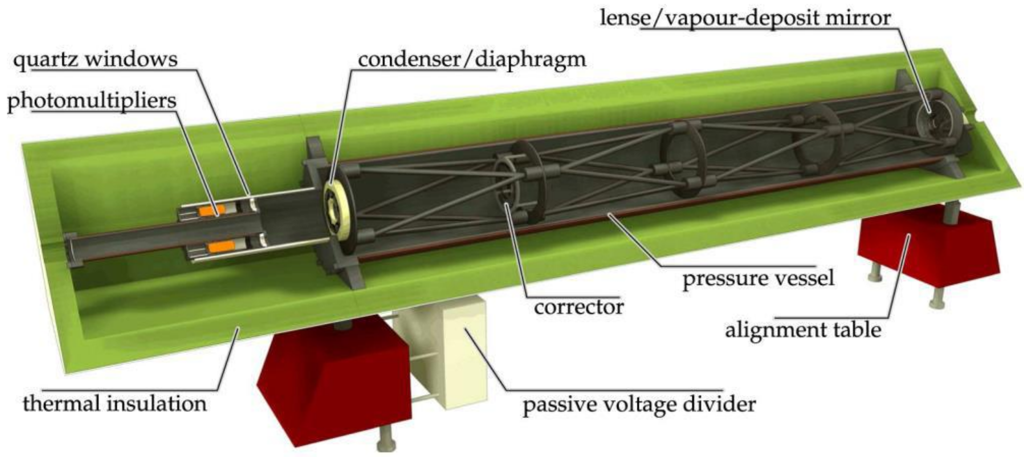

Figure 39: CEDAR 2018 upgrade for better rate- and thermal stability.

a wall of spherical UV mirrors. Presently, the photon detection system is formed by MAPMTS coupled to individual fused silica-lens telescopes in the central region, covering 25% of the instrumented surface, where the rate is higher, and gaseous detectors in the peripheral region. Two types of gaseous detectors are in use, both equipped with CsI photoconverter: MWPCs and novel ones, based on a hybrid MPGD architecture with two THick GEM (THGEM) layers followed by a MICROMEGAS multiplication stage, where the first THGEM also acts as photoconverter substrate. RICH-1 provides hadron PID in the range from 3 to 60 GeV/c, where 3 GeV/c is the effective threshold for pion identification and pions-kaons can be separated at 90% confidence level at 60 GeV/c [139].

For the future physics program at the M2 beamline, RICH-1 can be complemented by counters that enlarge the momentum range for positive hadron identification both at lower and higher momenta. For low momenta (referred to as "RICH-0" here, a DIRC counter enriched with a focusing system [140] with horizontal radiator bars arranged in a planar configuration can be used in order to separate hadrons in the range 0.2 GeV/c up to 5-6 GeV/c. Fused silica bars are the default choice, while the use of Plexiglas bars [141] is an alterative option to be analyzed. The default readout sensors are MAPMTs, while other fast, pixelized photon detectors as MCP-PMTs can be considered. A relevant feature is the reduced physical length of such a detector that can require no more than a 20 cm space-slot along the beam line.

6.2 Specific upgrades

6.2.1 Overview

- Proton radius (more in Sec. 6.2.2): high-pressure active TPC target (similar to A2 at MAMI) or hydrogen tube surrounded by SciFis; SciFi trigger system on scattered muon; silicon trackers to veto on straight tracks (kink trigger).

- GPD E in DVCS (more in Sec. 6.2.3): 3-layer silicon detector inside the existing but modified PT (NH_3 ↑) at very low temperature, for tracking of the recoil proton in DVCS and PID via dE/dx. Alternatively: SciFis.

- Anti-matter cross section for cosmic ray studies: recoil TOF detector (see Fig. 21, called "RPD" there); targets: LH2 and LHe.

- Spectroscopy with low-energy antiprotons (more in Sec. 6.2.4): target spectrometer (tracking, barrel calorimeter) similar to WASA at COSY [76]; target: LH2, foil, wire.

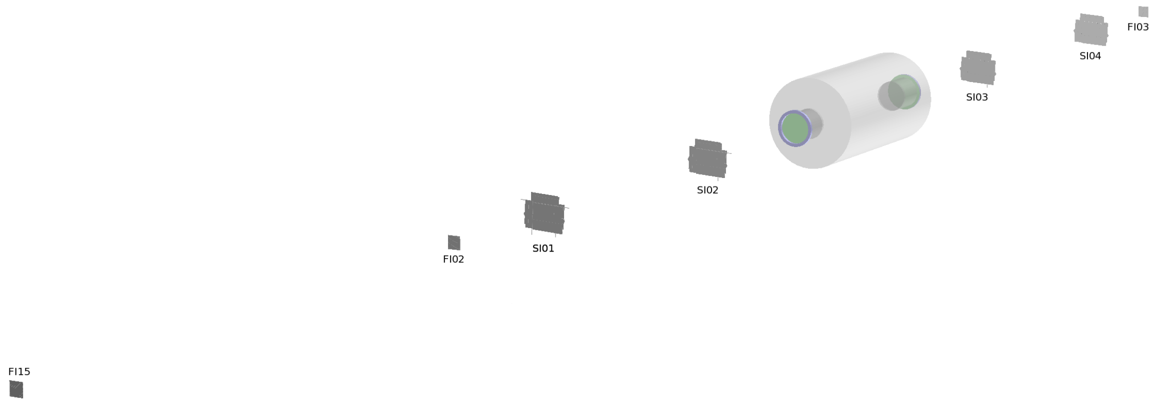

Figure 40: Rendering of the target region of the COMPASS $\mu - p$ set-up.

– Drell Yan general: high-purity and -efficiency di-muon trigger; dedicated precise luminosity measurement; dedicated vertex-detection system; beam trackers; targets: ^{6}LiD$\uparrow$, and C/W.

– Drell-Yan RF-separated beams (more in Sec. 6.2.5): due to the lower beam energy, a wide aperture will be needed (up to $\pm$300 mrad): a "magnetized spectrometer" (active absorber) is under consideration. It could possibly be similar to Baby MIND at JParc [145] ("3-in-1" detector, spectrometer magnet, absorber).

– Prompt Photon Production: 20-30 cm steel absorber upstream of the target; new hodoscope upstream of the existing electromagnetic calorimeter ECal0; transparent setup with as little material as necessary.

– Spectroscopy with K^-: uniform acceptance; existing electromagnetic calorimeters; recoil TOF detector (see Fig. 21, called "RPD" there).

RICH-1, RICH-0, and CEDARs are skipped in this list. See Table 5 for this information.

6.2.2 High-pressure hydrogen TPC for proton-radius measurement

The experimental set-up for the proton radius measurement using elastic muon-proton scattering (Sec. 3.1) is depicted in Fig. 40. The active hydrogen target (ICAR [20]) is based on an existing set-up used for an experiment at GSI, which is shown in Fig. 41. Such a system was developed by the Gatchina group (PNPI) and was employed for multiple radius measurements in the past.

6.2.2.1 Proton recoil measurement The proton recoil measurement can be achieved using a double target scenario. For small values of Q^2 and proton kinetic energies up to a few MeV, a high-pressure hydrogen TPC, operated as ionisation chamber, can be used. The energy loss for incoming and outgoing muons is about 2 keV/cm and thus small compared to the proton energy loss even for proton kinetic energies of 10 MeV, as long as the path length traversed is smaller than 10 cm. For $Q^2 = 10^{-4}\,(\mathrm{GeV}/c)^2$, the kinetic energy of recoil protons is 50$-$60 keV. This value corresponds to the energy resolution obtained by [19] in an experiment measuring πp scattering in the Coulomb-nuclear interference region. This roughly determines the scale for the lowest value of Q^2 in the experiment.

At higher values of Q^2, when the recoiling protons are no longer stopped inside the hydrogen volume, one may envisage to surround the central part of the active target with a barrel made from scintillating fibres. Consecutive layers are arranged in a relative stereo angle of 6°. A possible set-up is shown in Fig. 42. The scintillation light from the fibres is detected on one side by SiPM of high pixel density (Hamamatsu S13360-3025 or KETEK PM3325) to reduce saturation effects. The backend opposing

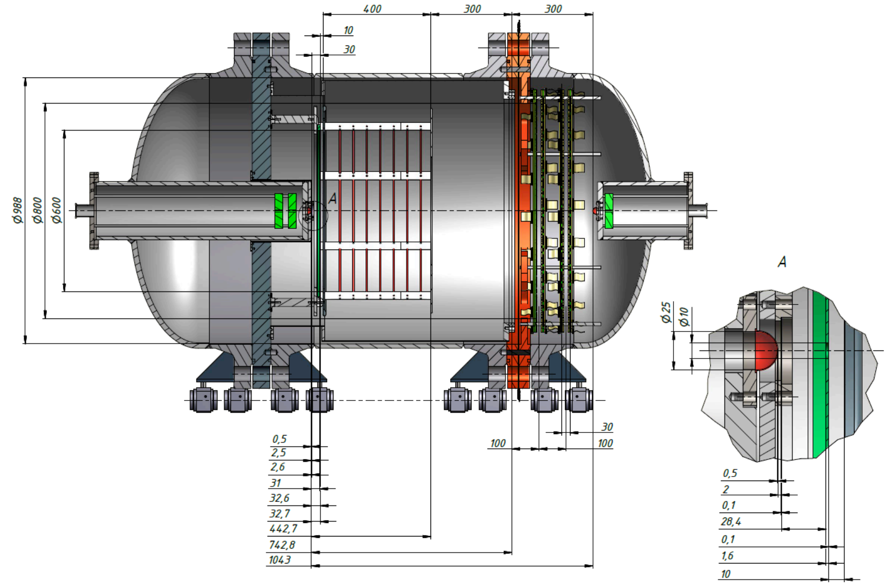

Figure 41: Sketch of the target TPC with pressure vessel as conceived for an elastic $e^{-}p$ scattering experiment at MAMI. The forward tracker system on the right side of the vessel will not be installed for the M2 measurement.

the SiPM is aluminised. In the model used for simulation we assumed 10 layers of scintillating fibres, summing up to $2-3$ cm thickness. In order to perform a combined $(dE/dx,\ E)$ analysis, we intend to surround the fibre tracker by 8 plates of scintillator, similar to the proton recoil detector surrounding the liquid hydrogen target of COMPASS in 2009. With this, we should be able to stop protons up to 100 MeV. By reconstructing the Bragg curve we can obtain energy resolutions of the order of a few percent (Fig. 43). We have performed test measurements on energy resolution up to energies of about 50 MeV at PSI using various fibre material and models of SiPM. Results from the analysis are expected soon.

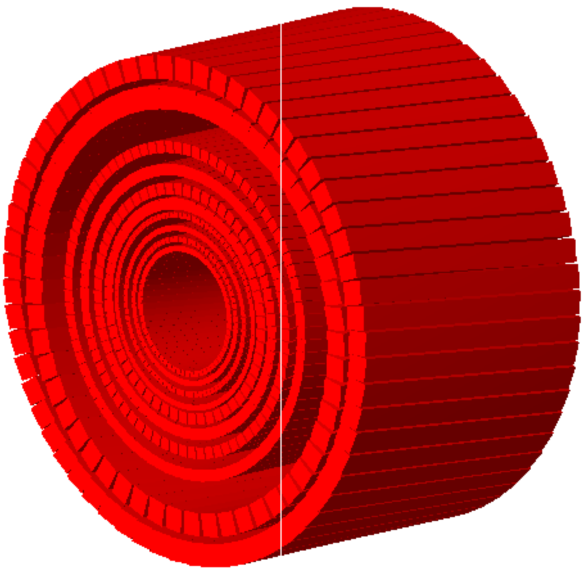

Figure 42: Layout of the recoil proton detector used for the high Q^2 range.

As the range of low energy protons in the SciFi material is low we need to keep the fibre thickness small

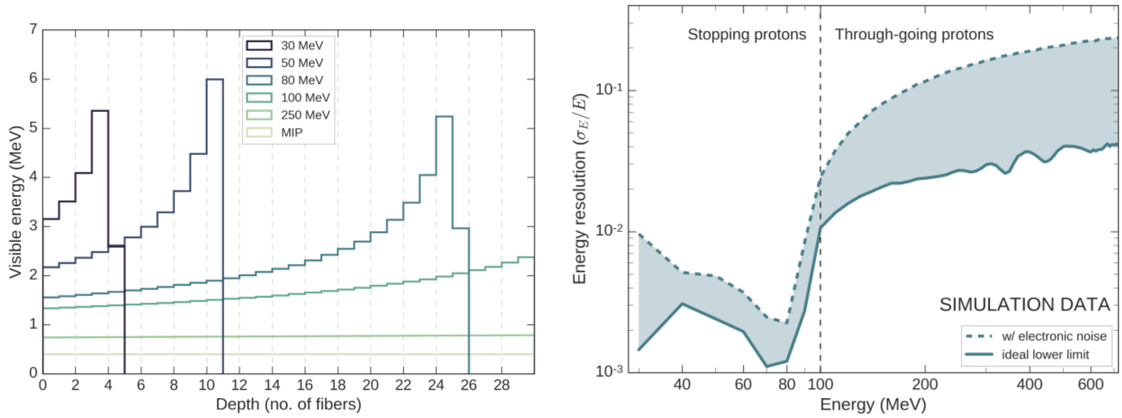

Figure 43: Left: Expected energy loss in individual fibres traversed by recoil protons for different proton energies. Right: energy resolution obtained by Bragg-curve fitting using simulation data. Work in progress and data are still very preliminary.

in the inner layers ($2 \times 2\,\mathrm{mm}^2$ or thinner). A requirement for the recoil proton of crossing at least 2 fibres to determine a 3D impact point imposes a lower limit for the kinetic energy of recoil protons of about 15-20 MeV. This corresponds to a lower value of $Q^2 > 0.03 - 0.04\,(\mathrm{GeV}/c)^2$. The fibre cross-section for the outer layers may grow to $4 \times 4\,\mathrm{mm}^2$ and $8 \times 8\,\mathrm{mm}^2$.

The geometry of the scintillator barrel has not yet been optimised in terms of geometry, fibre cross sections and number of channels. However, the arrangement sketched up is feasible and has a reasonably flat acceptance across Q^2. Optimisation should allow to further reduce an unwanted Q^2 dependence of the acceptance and allow to obtain an effective threshold of $Q^2 > 0.3\,(\mathrm{GeV}/c)^2$.

6.2.2.2 Muon measurement The scattered muon can be identified using the COMPASS setup including the present muon identification system. The energy transfer in the reaction is very small and falls within the energy resolution of the spectrometer. However, COMPASS has demonstrated excellent angular resolution in the context of a measurement scattering pions of 190 GeV energy off the electromagnetic field of heavy nuclei like Pb or Ni [23]. Despite the presence of a solid target of thickness $\mathrm{d} = 20\% X_0$, COMPASS obtained a Q^2-resolution of $\Delta Q^2 = 2 \cdot 10^{-4}\,(\mathrm{GeV}/c)^2$. This was achieved by means of two silicon telescopes placed upstream and downstream of the solid target. The position resolution of each silicon station was about $\Delta x \approx 4\,\mu$m. In the future set-up, it is intended to position the silicon stations within a telescope much further apart (1 m providing a longer lever arm). It is assumed that the angular resolution can be improved such as to achieve a resolution of $\Delta Q^2 = 1.4 \cdot 10^{-4}\,(\mathrm{GeV}/c)^2$ by:

1. replacing the thick solid target with a pressurised gaseous hydrogen target;

2. increasing the spacing of the layers of the silicon telescope in order to roughly match multiple scattering effects in the silicon itself.

6.2.2.3 Trigger One of the challenges of this experiment will be the trigger. A trigger on the proton signal inside the TPC will require a trigger latency of the order of $20\,\mu$s owing the the drift time. This is not compatible with the current COMPASS readout scheme. We envisage two different approaches to circumvent this limitation.

The approach compatible with current front-ends is the development of a trigger on a kink of the muon track. Two scintillating fiber detectors upstream of the target (labelled *FI15* and *FI02* in Fig. 40) predict a straight track, a deviation from this straight track observed in a third scintillating fiber detector downstream of the target (labelled *FI03* in Fig. 40) is a sign for an interaction inside the target. To surpress deviations from the straight line caused by multiple scattering, the distance between the predicted and measured position should be adjustable for this trigger.

The more advance approach is based on the development of a triggerless readout scheme requiring the development or integration of new front-end electronics for the silicon strip detectors and the TPC.

6.2.3 Recoil detector with polarized target

The major technical challenge for the measurement of the $\mu p^{\uparrow} \rightarrow \mu\gamma p$ reaction (Sec. 3.2) is the detection of the recoil particles ejected from a solid-state transversely polarized target. The detection of the recoil particles, whose momentum needs to be determined with a precision of 10% or better, is key to ensuring the exclusivity of the reaction. Missing-mass techniques cannot be employed in the COMPASS case due to the experimental resolution, which is not better than 2 GeV. Two solutions can be envisaged to minimize the amount of material crossed by the recoil particles before being detected, and therefore to optimize the minimum value of $|t|$ accessible by the experiment:

1. The recoil particle detector is placed outside of low-mass polarized target system, with a thin super-conducting dipole located close to the target cells and enclosed inside a thin-walled cryostat.
2. The recoil particle detector is inserted in the cryogenic vacuum volume surrounding the target cell and inside a large dipole magnet.

The first solution is technically very challenging, particularly from the point of view of the construction of a super-conducting dipole magnet with a low material budget. Moreover, it would require an additional external high-field solenoid magnet to re-polarize the target material every few days.

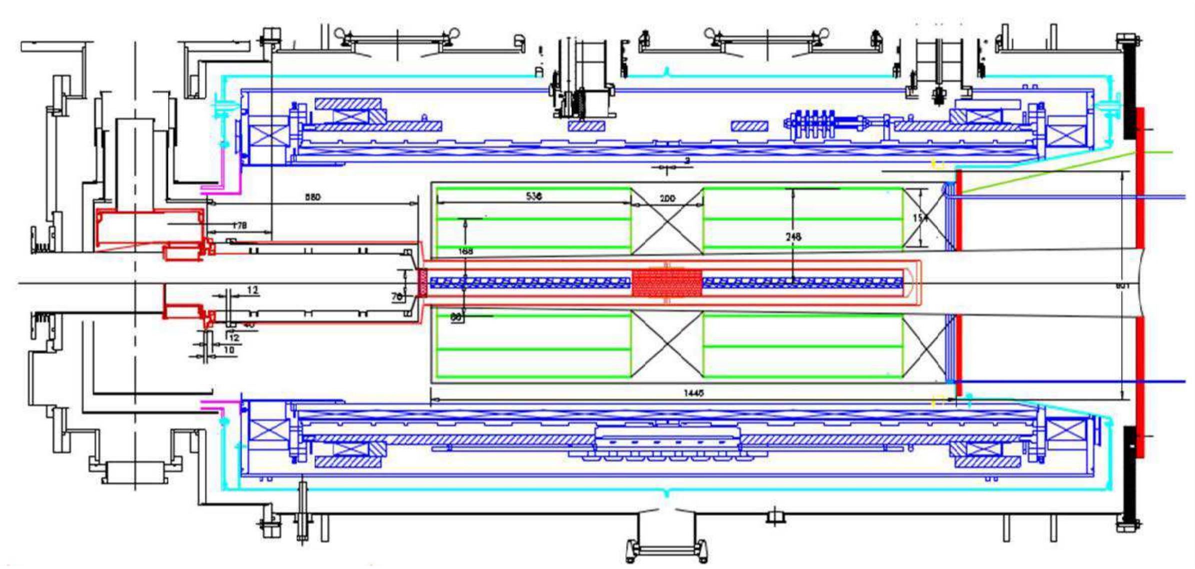

Figure 44: Conceptual view of the COMPASS polarized target coupled with silicon detectors for tracking and identification of recoil particles.

The feasibility of the second solution is currently under study, re-using the existing COMPASS polarized-target system, see Fig. 44. In this scenario, the shape of the micro-wave (MW) cavity is modified and decoupled from the remainder of the inner target magnet volume, while sharing the same vacuum. The cylindrical part of the cavity consists of a 0.2-0.4 mm thick copper foil to avoid distortion of the MW field by the presence of silicon detectors. Recoil-particle detection is based on two or three concentric barrels of silicon pixel detectors (Fig. 45) in the empty space between the target cell and the superconducting magnets to measure particle trajectories and energy loss (dE/dx). Alternatively it is considered to use scintillating fiber detectors instead of silicon detectors. SciFi detectors can be accommodated more easily in the target magnet with less challenging signal transport out of the magnet.

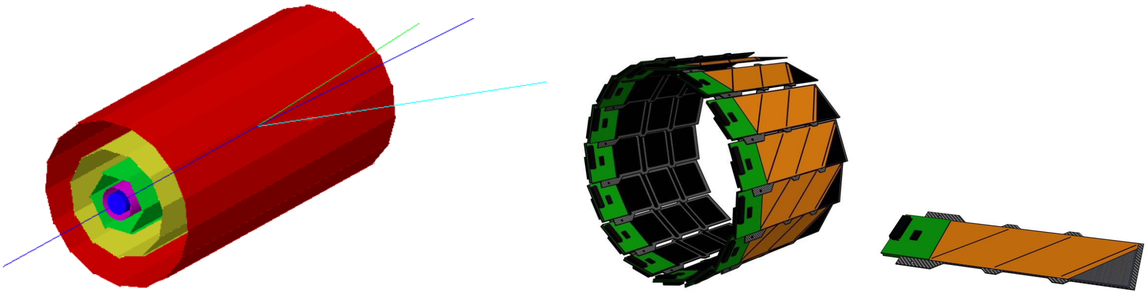

Figure 45: Left: 3-layer silicon detector (SD) surrounding the polarized target, with trajectories of particles emerging from an exclusive DVCS event: proton (light blue), photon (green), muon (blue). From inside to outside: target, MV cavity, inner SD, middle SD, outer SD. Each layer is 300 μm thick. Middle: conceptual design of outer SD layer with 300 mm diameter, right: SD ladder design.

Performance of silicon detectors at low temperatures. Silicon detectors are capable of working (i) in a magnetic field (longitudinal or transversal) of about 0.5-2 T, (ii) in low temperatures of about 5-10 K [146], (iii) in presence of a MW field, and (iv) in a vacuum of about 10^{-8} bar. Modifications of the inner volume of the existing target magnet are necessary in order to minimize the influence of the MW radiation on the silicon performance and to provide space for input/output connections. The MW cavity is cooled by circulation of liquid ^{4}He. Part of this flow also cools a mesh surrounding the silicon-detector volume, keeping it at uniform temperature. This prevents decrepitation of the silicon wavers and dissipates the heat from their readout electronics.

Double-sided Si-microstrip detectors developed at the Laboratory of High Energy Physics (LHEP) at the Joint Institute for Nuclear Research (JINR) meet the main requirements to serve as recoil detector inside a COMPASSlike polarized-target magnet. The LHEP JINR silicon detector is comparatively inexpensive. It has been tested in an experimental environment close to that of the present COMPASS polarized-target system. Tests with multi-layered flexible boards are under preparation with participation of LED Technologies of Ukraine (LTU / Kharkiv) [147].

PID and momentum reconstruction of recoil particles. Simulations based on the silicon geometry in Fig. 45 were carried out with the GEANT 4.6.10 package using the HepGen generator for DVCS protons, and Pythia for SIDIS protons and pions. The dE/dx technique for Particle IDentification (PID) distinguishing protons, kaons, and pions requires detectors that are capable of measuring: (i) space coordinates of the recoil particles with a precision of about 1 mm at least in 3 space points, (ii) momentum reconstruction in the range $\sim$100-1000 MeV with a precision of about 5-10%, and (iii) dE/dx for each recoil particle with precision of $\sim$10%. The particle momentum is determined from the reconstruction of its trajectory in the magnetic field, which requires at least 3 space points. Figure 46 shows the expected momentum distributions and resolutions of recoil protons and the PID performance.

6.2.4 Target spectrometer for spectroscopy with low-E antiprotons

The exclusive measurements in spectroscopy with low-energy antiprotons (Sec. 4.2) require additional coverage of charged-particle tracking and calorimetry around the target. Figure 47 shows as an example the setup of experiment E836 at Fermilab [71], split into a barrel part and a forward part. The PANDA experiment was designed in a similar way, with improved calorimetry and charged-particle tracking also

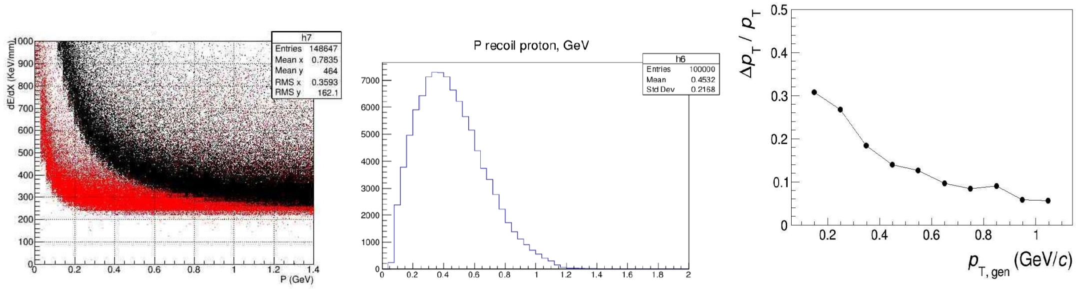

Figure 46: Simulations with silicons around the polarized target. Left: energy loss versus momentum in silicon pions (red) and protons (black), middle: momentum distribution for DVCS recoil protons, right: momentum resolution for protons.

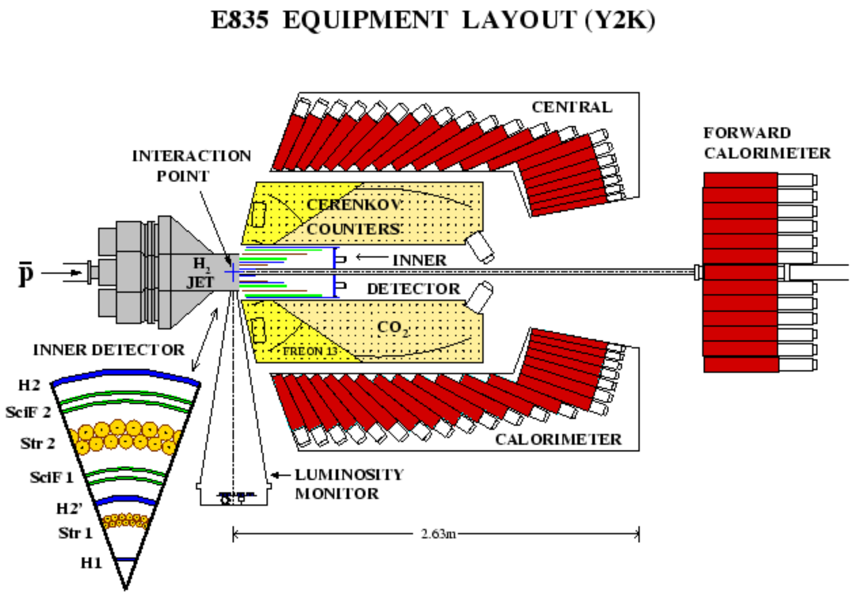

Figure 47: Schematic view of the E835 setup at Fermilab [71].

in the forward detector. With components for PANDA not yet being fully available, a possible option which we are investigating at the moment is to re-use parts of the barrel spectrometer of the WASA detector [76]. It consists of an electromagnetic calorimeter made up of 1012 CsI(Na) scintillating crystals with a thickness corresponding to $16X_0$. It can measure photons, electrons, and positrons with energies up to 800 MeV at a very low threshold of 2 MeV. In its original shape, it covers scattering angles from $20°$ up to $169°$. Figure 48 shows the geometry and angular acceptance of the WASA calorimeter.

In order to maximize the acceptance for antiproton annihilations at the M2 beamline, it could be envisaged to rotate it by $180°$, such that the coverage in forward direction increases and matches the acceptance of the first forward calorimeter ECal0 (up to $\sim 17°$). Charged-particle tracking is performed in a 1.3 T solenoid magnetic field provided by a superconducting coil located inside the calorimeter. The originally used Straw tubes for charged-particle tracking will have to be replaced by a new tracking detector because of ageing. One option could be a continuously operating GEM-TPC as originally developed for PANDA and built and tested in FOPI [77].

The forward-going particles will be detected by the existing COMPASS detectors, including ECal0. With this scenario, a high and uniform acceptance for charged and neutral particles will be achieved even at the low momenta foreseen for the antiproton beam.

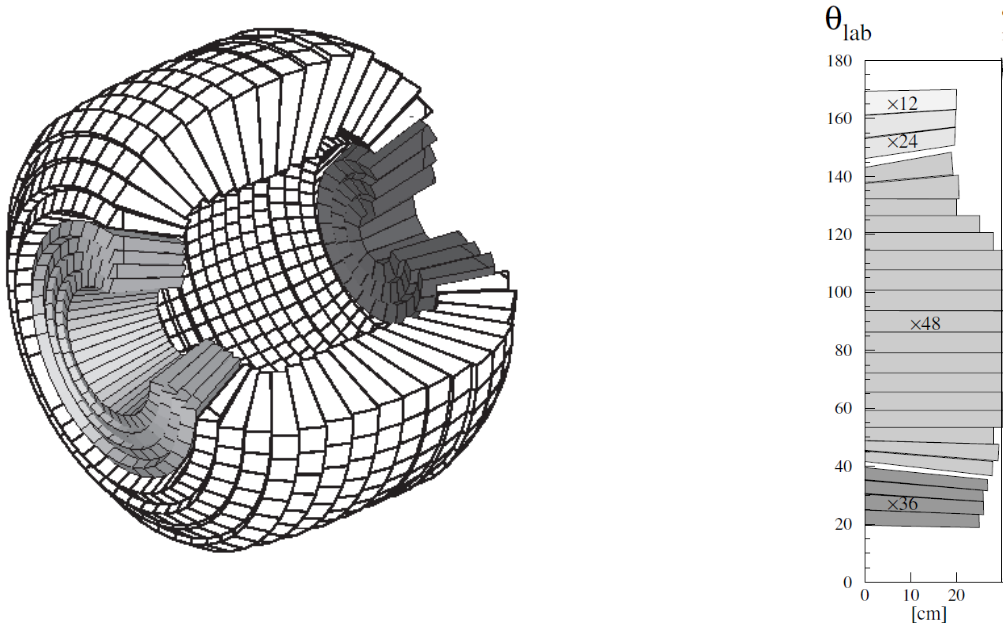

(a) (b)

Figure 48: The scintillating electromagnetic calorimeter (SEC) of the WASA detector [76]. (a) Geometry of the crystals. In the WASA at COSY setup, the beam was coming from the right side, while at the M2 beamline, we envisage to rotate the detector by 180° such that it would come from the left side. (b) Angular coverage in the laboratory system (the curves on the right hand side correspond to WASA at COSY and are not relevant here).

6.2.5 Active absorber for Drell-Yan with RF-separated hadron beams

For Drell-Yan physics with high-intensity kaon and antiproton beams (Sec. 5.3), *text to be added, work in progress.*

7 Schedule

References

[1] J. Dudek, R. Ent, R. Essig, K. Kumar, C. Meyer, et al., Physics Opportunities with the 12 GeV Upgrade at Jefferson Lab, Eur. Phys. J. A48 (2012) 187. (Cited in Sec. 3.2.2.)

[2] A. V. Belitsky, D. Mueller, A. Kirchner, Theory of deeply virtual compton scattering on the nucleon, Nucl. Phys. B629 (2002) 323–392. (Cited in Sec. 3.2.3.)

[3] M. Vanderhaeghen, P. A. M. Guichon, M. Guidal, Deeply virtual electroproduction of photons and mesons on the nucleon: Leading order amplitudes and power corrections, Phys. Rev. D60 (1999) 094017. (Cited in Secs. 3.2.3 and 4.)

[4] S. V. Goloskokov, P. Kroll, Transversity in hard exclusive electroproduction of pseudoscalar mesons, Eur. Phys. J. A47 (2011) 112. (Cited in Secs. 3.2.3 and 4.)

[5] A. Airapetian, et al., Measurement of Azimuthal Asymmetries With Respect To Both Beam Charge and Transverse Target Polarization in Exclusive Electroproduction of Real Photons, JHEP 06 (2008) 066. (Cited in Secs. 5 and 3.2.4.)

[6] F. Gautheron, et al., COMPASS-II proposal, CERN-SPSC-2010-014, SPSC-P-340 (March 2010). (Cited in Sec. 5.)

[7] R. Hofstadter, R. W. McAllister, Electron Scattering From the Proton, Phys. Rev. 98 (1955) 217–218. (Cited in Sec. 3.1.)

[8] J. C. Bernauer, P. Achenbach, C. Ayerbe Gayoso, R. Böhm, D. Bosnar, L. Debenjak, M. O. Distler, L. Doria, A. Esser, H. Fonvieille, J. M. Friedrich, J. Friedrich, M. Gómez Rodríguez de la Paz, M. Makek, H. Merkel, D. G. Middleton, U. Müller, L. Nungesser, J. Pochodzalla, M. Potokar, S. Sánchez Majos, B. S. Schlimme, S. Širca, T. Walcher, M. Weinriefer, High-precision determination of the electric and magnetic form factor s of the proton, Phys. Rev. Lett. 105 (2010) 242001.
URL https://link.aps.org/doi/10.1103/PhysRevLett.105.242001 (Cited in Sec. 3.1.)

[9] J. C. Bernauer, Precise form factors from elastic electron scattering, J. Phys. Conf. Ser. 381 (2012) 012006. (Cited in Sec. 3.1.)

[10] R. Pohl, et al., The size of the proton, Nature 466 (2010) 213–216. (Cited in Secs. 3.1 and 3.1.1.)

[11] R. Pohl, The Lamb shift in muonic hydrogen and the proton radius puzzle, Hyperfine Interact. 227 (1-3) (2014) 23–28. (Cited in Secs. 3.1 and 3.1.1.)

[12] A. Antognini, et al., Experiments towards resolving the proton charge radius puzzle, EPJ Web Conf. 113 (2016) 01006. (Cited in Secs. 3.1 and 3.1.1.)

[13] A. H. Gasparian, The New Proton Radius Experiment at Jefferson Lab, JPS Conf. Proc. 13 (2017) 020052. (Cited in Sec. 3.1.1.)

[14] R. Pohl, et al., Deuteron charge radius and Rydberg constant from spectroscopy data in atomic deuterium, Metrologia 54 (2017) L1. (Cited in Sec. 3.1.1.)

[15] F. Biraben, et al., Proposal for an experiment at PSI: Lamb shift in muonic helium (2017).
URL https://www.ethz.ch/content/dam/ethz/special-interest/phys/particle-physics/precisionphysicsatlowenergy-dam/Research/Proposal_muHe_pdf.pdf (Cited in Sec. 3.1.1.)

[16] R. Gilman, et al., Studying the Proton "Radius" Puzzle with μp Elastic Scattering . (Cited in Sec. 3.1.1.)

[17] B. S. Henderson, et al., Hard Two-Photon Contribution to Elastic Lepton-Proton Scattering: Determined by the OLYMPUS Experiment, Phys. Rev. Lett. 118 (9) (2017) 092501. (Not cited.)

[18] T. Suda, Electron scattering experiment off proton at ultra-low q^2 (2016).
URL http://www2.yukawa.kyoto-u.ac.jp/~min2016/slides/Suda_MIN2016.pdf, talkpresentedatMesoninNucleusconference (Cited in Sec. 3.1.)

[19] A. A. Vorobyov, G. A. Korolev, V. A. Schegelsky, G. Ye. Solyakin, G. L. Sokolov, Yu. K. Zalite, A method for studies of small-angle hadron-proton elastic scattering in the coulomb interference region, Nucl. Instrum. Meth. 119 (1974) 509–519. (Cited in Secs. 3.1.1 and 6.2.2.1.)

[20] S. Ilieva, et al., Nuclear-matter density distribution in the neutron-rich nuclei 12,14 Be from proton elastic scattering in inverse kinematics, Nucl. Phys. A875 (2012) 8–28. (Cited in Secs. 3.1.1 and 6.2.2.)

[21] A. Vorobyov, Proton radius status and perspective, incl.: Proposal for high precision measuremens of the *ep* differential cross sections at small t values with the recoiled proton detector (2016).
URL https://indico.cern.ch/event/544849/contributions/2213665/attachments/1301151/1942517/Vorobyev_ep_report_27_june_2016.pdf (Cited in Sec. 3.1.1.)

[22] M. Mihovilovič, et al., First measurement of proton's charge form factor at very low Q^2 with initial state radiation, Phys. Lett. B771 (2017) 194–198. (Cited in Sec. 3.1.1.)

[23] C. Adolph, et al., Measurement of the charged-pion polarizability, Phys. Rev. Lett. 114 (2015) 062002. (Cited in Secs. 5.5.1 and 6.2.2.2.)

[24] C. Roberts, Perspective on the Origin of Hadron Masses, Few Body Syst. 58. (Cited in Sec. 4.1.1.)

[25] X. Ji, Parton Physics on a Euclidean Lattice, Phys. Rev. Lett. 110. (Cited in Sec. 4.1.1.)

[26] J. X. J. L. Zhang, J.-H., L. H.-W., Pion Distribution Amplitude from Lattice QCD, Phys. Rev. D 95. (Cited in Sec. 4.1.1.)

[27] A. Abdel-Rehim, et al., Nucleon and pion structure with lattice QCD simulations at physical value of the pion mass, Phys. Rev. D 92. (Cited in Sec. 4.1.1.)

[28] S.-i. Nam, Parton-distribution functions for the pion and kaon in the gauge-invariant nonlocal chiral-quark model, Phys. Rev. D86 (2012) 074005. (Cited in Sec. 4.1.1.)

[29] P. T. P. Hutauruk, I. C. Cloet, A. W. Thomas, Flavor dependence of the pion and kaon form factors and parton distribution functions, Phys. Rev. C94 (3) (2016) 035201. (Cited in Sec. 4.1.1.)

[30] A. Watanabe, C. W. Kao, K. Suzuki, Meson cloud effects on the pion quark distribution function in the chiral constituent quark model, Phys. Rev. D94 (11) (2016) 114008. (Cited in Sec. 4.1.1.)

[31] B. Pasquini, P. Schweitzer, Pion TMDs in light-front constituent approach, and Boer-Mulders effect in the pion-induced Drell-Yan process, Phys.Rev. D90 (2014) 014050. (Cited in Sec. 4.1.1.)

[32] T. Nguyen, A. Bashir, C. D. Roberts, P. C. Tandy, Pion and kaon valence-quark parton distribution functions, Phys. Rev. C83 (2011) 062201. (Cited in Sec. 4.1.1.)

[33] C. Chen, L. Chang, C. D. Roberts, S. Wan, H.-S. Zong, Valence-quark distribution functions in the kaon and pion, Phys. Rev. D93 (7) (2016) 074021. (Cited in Secs. 4.1.1, 5.3.2 and 5.3.4.)

[34] J. Badier, et al., Experimental Determination of the pi Meson Structure Functions by the Drell-Yan Mechanism, Z. Phys. C18 (1983) 281. (Cited in Secs. 4.1.1, 4.1.2 and 6.)

[35] B. Betev, et al., Observation of Anomalous Scaling Violation in Muon Pair Production by 194-GeV/$c\pi^-$ Tungsten Interactions, Z. Phys. C28 (1985) 15. (Cited in Secs. 4.1.1 and 4.1.2.)

[36] J. S. Conway, et al., Experimental study of muon pairs produced by 252-gev pions on tungsten, Phys. Rev. D39 (1989) 92–122. (Cited in Secs. 4.1.1 and 4.1.2.)

[37] A. Bordner, et al., Experimental information on the pion gluon distribution function, Z. Phys. C72 (1996) 249–254. (Cited in Sec. 4.1.1.)

[38] S. Chekanov, et al., Leading proton production in e+ p collisions at HERA, Nucl. Phys. B658 (2003) 3–46. (Cited in Sec. 4.1.1.)

[39] F. D. Aaron, et al., Measurement of Leading Neutron Production in Deep-Inelastic Scattering at HERA, Eur. Phys. J. C68 (2010) 381–399. (Cited in Secs. 4.1.1 and 4.1.6.)

[40] R. E. Glueck, M., A. Vogt, Pionic Parton Distributions, Z.Phys. C 53. (Cited in Sec. 4.1.1.)

[41] M. Corden, et al., Production of muon pairs in the continuum region by 39.5 GeV/c $\pi^{\pm}$, K$^{\pm}$, p and $\bar{p}$ beams incident on a tungsten target . (Cited in Sec. 4.1.2.)

[42] P. J. Sutton, A. D. Martin, R. G. Roberts, W. J. Stirling, Parton distributions for the pion extracted from Drell-Yan and prompt photon experiments, Phys. Rev. D45 (1992) 2349–2359. (Cited in Secs. 4.1.2 and 5.3.3.)

[43] M. Gluck, E. Reya, A. Vogt, Pionic parton distributions, Z. Phys. C53 (1992) 651–656. (Cited in Sec. 4.1.2.)

[44] M. Gluck, E. Reya, I. Schienbein, Pionic parton distributions revisited, Eur. Phys. J. C10 (1999) 313–317. (Cited in Sec. 4.1.2.)

[45] M. Bonesini, et al., High Transverse Momentum Prompt Photon Production by π^- and π^+ on Protons at 280-GeV/c, Z. Phys. C37 (1988) 535. (Cited in Secs. 4.1.2 and 5.4.2.)

[46] C. De Marzo, et al., Measurement of direct photon production at large transverse momentum in π^-p, π^+p, and pp collisions at 300 GeV/c, Phys. Rev. D 36 (1987) 8–15. (Cited in Sec. 4.1.2.)

[47] J. T. Londergan, G. Q. Liu, E. N. Rodionov, A. W. Thomas, Probing the pion sea with pi D Drell-Yan processes, Phys. Lett. B361 (1995) 110–114. (Cited in Sec. 4.1.2.)

[48] J. Badier, et al., Experimental J/psi Hadronic Production from 150-GeV/c to 280-GeV/c, Z. Phys. C20 (1983) 101. (Cited in Secs. 4.1.2, 4.1.3 and 4.1.3.)

[49] J. G. McEwen, et al., Measurement of the Gluon Structure Function of the Pion, Phys. Lett. 121B (1983) 198–202. (Cited in Sec. 4.1.3.)

[50] C. Akerlof, et al., ψ production and $\bar{p}N$ and π^-N interactions at 125-GeV/c and a determination of the gluon structure functions of the $\bar{p}$ and the π^-, Phys. Rev. D48 (1993) 5067–5080. (Cited in Sec. 4.1.3.)

[51] R. Gavai, D. Kharzeev, H. Satz, G. A. Schuler, K. Sridhar, R. Vogt, Quarkonium production in hadronic collisions, Int. J. Mod. Phys. A10 (1995) 3043–3070. (Cited in Sec. 4.1.3.)

[52] G. T. Bodwin, E. Braaten, G. P. Lepage, Rigorous QCD analysis of inclusive annihilation and production of heavy quarkonium, Phys. Rev. D51 (1995) 1125–1171, [Erratum: Phys. Rev.D55,5853(1997)]. (Cited in Sec. 4.1.3.)

[53] R. Vogt, The x(F) dependence of ψ and Drell-Yan production, Phys. Rev. C61 (2000) 035203. (Cited in Secs. 4.1.3 and 5.3.4.)

[54] J. J. Aubert, et al., The ratio of the nucleon structure functions $F2_n$ for iron and deuterium, Phys. Lett. 123B (1983) 275–278. (Cited in Sec. 4.1.4.)

[55] D. F. Geesaman, K. Saito, A. W. Thomas, The nuclear EMC effect, Ann. Rev. Nucl. Part. Sci. 45 (1995) 337–390. (Cited in Sec. 4.1.4.)

[56] O. Hen, G. A. Miller, E. Piasetzky, L. B. Weinstein, Nucleon-Nucleon Correlations, Short-lived Excitations, and the Quarks Within, Rev. Mod. Phys. xx (2017) xxxxx. (Cited in Sec. 4.1.4.)

[57] J. Seely, et al., New measurements of the EMC effect in very light nuclei, Phys. Rev. Lett. 103 (2009) 202301. (Cited in Sec. 4.1.4.)

[58] P. Paakkinen, K. J. Eskola, H. Paukkunen, Applicability of pion-nucleus drell-yan data in global analysis of nuclear parton distribution functions, Physics Letters B 768 (2017) 7 – 11. URL http://www.sciencedirect.com/science/article/pii/S0370269317300990 (Cited in Secs. 4.1.4 and 9.)

[59] I. Cloet, W. Bentz, A. Thomas, Isovector EMC effect explains the NuTeV anomaly, Phys.Rev.Lett. 102 (2009) 252301. (Cited in Sec. 4.1.4.)

[60] D. Dutta, J. C. Peng, I. C. Cloet, D. Gaskell, Pion-induced Drell-Yan processes and the flavor-dependent EMC effect, Phys. Rev. C83 (2011) 042201. (Cited in Sec. 4.1.4.)

[61] P. Paakkinen, K. J. Eskola, H. Paukkunen, Pion-nucleus drell-yan data as a novel constraint for nuclear pdfs, Proceedings of Science, DIS2017 (2017) 205 – 2010. URL https://pos.sissa.it/297/205/pdf (Cited in Sec. 4.1.4.)

[62] A. Camsonne, et al., Measurement of Tagged Deep Inelastic Scattering (TDIS), JLAB proposal C12-14-010 . (Cited in Sec. 4.1.6.)

[63] J. Arrington, et al., Sea Quest, http://www.phy.anl.gov/mep/SeaQuest/ . (Cited in Sec. 4.1.6.)

[64] S. Riordan, et al., The EMC PVDIS Experiment: A Constraint on Isovector Dependent Nuclear Modification Effects Using Parity-Violating Deep Inelastic Scattering, JLAB proposal C12-14-007 . (Cited in Sec. 4.1.6.)

[65] I. C. Cloet, W. Bentz, A. W. Thomas, Parity-violating DIS and the flavour dependence of the EMC effect, Phys. Rev. Lett. 109 (2012) 182301. (Cited in Sec. 4.1.6.)

[66] S. L. Olsen, T. Skwarnicki, D. Zieminska, Non-Standard Heavy Mesons and Baryons, an Experimental Review . (Cited in Secs. 4.2.1 and 11.)

[67] C. Adolph, et al., Observation of a New Narrow Axial-Vector Meson $a_1(1420)$, Phys. Rev. Lett. 115 (8) (2015) 082001. (Cited in Secs. 4.2.1 and 5.2.3.)

[68] B. Ketzer, Hybrid Mesons, PoS QNP2012 (2012) 025. (Cited in Sec. 4.2.1.)

[69] L. Liu, G. Moir, M. Peardon, S. M. Ryan, C. E. Thomas, P. Vilaseca, J. J. Dudek, R. G. Edwards, B. Joo, D. G. Richards, Excited and exotic charmonium spectroscopy from lattice QCD, JHEP 07 (2012) 126. (Cited in Sec. 12.)

[70] E. Aker, et al., The Crystal Barrel spectrometer at LEAR, Nucl. Instrum. Meth. A321 (1992) 69–108. (Cited in Sec. 4.2.1.)

[71] G. Garzoglio, et al., Experiment E835 at Fermilab, Nucl. Instrum. Meth. A519 (2004) 558–609. (Cited in Secs. 4.2.1, 6.2.4 and 47.)

[72] D. Bettoni, The E835 experiment at Fermilab, Hyperfine Interact. 194 (1-3) (2009) 225–231. (Cited in Sec. 4.2.1.)

[73] M. Lutz, et al., Physics Performance Report for PANDA: Strong Interaction Studies with Antiprotons . (Cited in Sec. 4.2.1.)

[74] H. W. Atherton, C. Bovet, N. T. Doble, L. Piemontese, A. Placci, M. Placidi, D. E. Plane, M. Reinharz, E. Rossa, G. Von Holtey, Precise measurements of particle production by 400 GeV/c protons on beryllium targets, CERN Yellow Reports: Monographs, CERN, Geneva, 1980.
URL http://cds.cern.ch/record/133786 (Cited in Secs. 4.2.2 and 14.)

[75] J. Van de Wiele, S. Ong, Study of associated charmonium J/Ψ production in $\bar{p}p \to \pi^0$ + J/Ψ, Eur. Phys. J. C73 (12) (2013) 2640. (Cited in Sec. 4.2.3.)

[76] H. H. Adam, et al., Proposal for the wide angle shower apparatus (WASA) at COSY-Julich: WASA at COSY . (Cited in Secs. 6.2.1, 6.2.4 and 48.)

[77] M. Berger, et al., A Large Ungated TPC with GEM Amplification, Nucl. Instrum. Meth. A869 (2017) 180–204. (Cited in Sec. 6.2.4.)

[78] P. Bernard, P. Lazeyras, H. Lengeler, V. Vaghin, Particle separation with two-and three-cavity RF separators at CERN, CERN Yellow Reports: Monographs, CERN, Geneva, 1968.
URL http://cds.cern.ch/record/275757 (Cited in Sec. 5.1.)

[79] K. Olive, Review of Particle Physics, Chinese Physics C 40 (10) (2016) 100001. (Cited in Secs. 5.2.1 and 28.)

[80] D. Ebert, R. N. Faustov, V. O. Galkin, Mass spectra and Regge trajectories of light mesons in the relativistic quark model, Physical Review D 79 (11) (2009) 114029. (Cited in Secs. 5.2.1 and 28.)

[81] S. Godfrey, N. Isgur, Mesons in a relativized quark model with chromodynamics, Physical Review D 32 (1) (1985) 189–231. (Cited in Sec. 5.2.1.)

[82] A. J. Bevan, et al., The Physics of the B Factories, The European Physical Journal C 74 (11) (2014) 3026. (Cited in Sec. 5.2.1.)

[83] A. Palano, M. R. Pennington, $K\pi$ $I = 1/2$ S-wave from η_c decay data at BaBar and classic Meson-Meson scattering from LASS . (Cited in Sec. 5.2.1.)

[84] S. Descotes-Genon, B. Moussallam, The $K_0^*(800)$ scalar resonance from Roy-Steiner representations of πK scattering . (Cited in Sec. 5.2.1.)

[85] J. R. Batley, et al., Precise tests of low energy QCD from K_{e4} decay properties, The European Physical Journal C 70 (3) (2010) 635–657. (Cited in Sec. 5.2.1.)

[86] R. García-Martín, R. Kamiński, J. Peláez, J. Ruiz de Elvira, Precise determination of the $f_0(600)$ and $f_0(980)$ pole parameters from a dispersive data analysis, Phys. Rev. Lett. 107 (2011) 072001. (Cited in Sec. 5.2.1.)

[87] G. F. Bertsch, et al., Review of Particle Physics, Physics Letters B 239. (Cited in Sec. 5.2.1.)

[88] B. Aubert, et al., Improved measurement of the CKM angle γ in $B^{\mp} \to D^{(*)}K^{(*)\mp}$ decays with a Dalitz plot analysis of D decays to $K^0_S\pi^+\pi^-$ and $K^0_S K^+K^-$, Physical Review D 78 (3) (2008) 034023. (Cited in Sec. 5.2.1.)

[89] The Belle Collaboration, A. Poluektov, A. Bondar, B. D. Yabsley, Evidence for direct CP violation in the decay $B^- \to D^{(*)}K^{\pm}$, $D \to K^0_s\pi^+\pi^-$ and measurement of the CKM phase ϕ_3, Physical Review D 81 (11) (2010) 112002. (Cited in Sec. 5.2.1.)

[90] R. Aaij, et al., Measurement of CP violation and constraints on the CKM angle γ in $B^{\pm} \to DK^{\pm}$ with $D \to K^0_S\pi^+\pi^-$ decays, Nuclear Physics B 888 (2014) 169–193. (Cited in Sec. 5.2.1.)

[91] A. Etkin, et al., Measurement and partial-wave analysis of the reaction $K^-p \to K^0_S\pi^+\pi^-n$ at $6\,\mathrm{GeV}/c$, Physical Review D 22 (1) (1980) 42–60. (Cited in Sec. 5.2.2.)

[92] G. Otter, et al., Evidence for structure in the 1^+ state of the Q region, Nuclear Physics B 106 (1976) 77–94. (Cited in Sec. 5.2.2.)

[93] J. Vergeest, et al., Partial-wave analysis in the Q region of $(\bar{K}\pi\pi)^-$ systems produced in K^-p reactions at $4.2\,\mathrm{GeV}/c$, Nuclear Physics B 158 (2-3) (1979) 265–279. (Not cited.)

[94] C. Daum, et al., Diffractive production of strange mesons at 63 GeV, Nuclear Physics B 187 (1) (1981) 1–41. (Cited in Sec. 5.2.2.)

[95] M. Baubillier, et al., A partial-wave analysis of the $K\pi\pi$ system produced in the reaction $K^-p \to \bar{K}^0\pi^+\pi^-n$ at $8.25\,\mathrm{GeV}/c$, Nuclear Physics B 202 (1) (1982) 21–42. (Not cited.)

[96] T. Armstrong, et al., A partial-wave analysis of the $K^-\pi$ system produced in the reaction $K^-p \to K^+K^-K^-p$ at $18.5\,\mathrm{GeV}/c$, Nuclear Physics B 221 (1) (1983) 1–15. (Cited in Sec. 5.2.2.)

[97] G. W. Brandenburg, et al., Observation of Two Strangeness-One Axial-Vector Mesons, Physical Review Letters 36 (13) (1976) 703–706. (Cited in Sec. 5.2.2.)

[98] D. Aston, et al., The strange meson resonances observed in the reaction $K^-p \to \bar{K}^0\pi^+\pi^-$ at $11\,\mathrm{GeV}/c$, Nuclear Physics B 292 (1987) 693–713. (Not cited.)

[99] D. Aston, et al., A study of $K^-\pi^+$ scattering in the reaction $K^-p \to K^-\pi^+n$ at $11\,\mathrm{GeV}/c$, Nuclear Physics B 296 (3) (1988) 493–526. (Not cited.)

[100] D. Aston, et al., Evidence for two $J^P = 2^-$ strange meson states in the $K_2(1770)$ region, Physics Letters B 308 (1-2) (1993) 186–192. (Cited in Sec. 5.2.2.)

[101] P. K. Jasinik, Analysis of Diffractive Dissociation of K^- into $K^-\pi^+\pi^-$ on a Liquid Hydrogen Target at the COMPASS Spectrometer, Ph.D. thesis, Johannes Gutenberg Universität Mainz (2012). (Cited in Sec. 5.2.2.)

[102] C. Adolph, et al., Resonance Production and $\pi\pi$ S-wave in $\pi^- + p \to \pi^-\pi^-\pi^+ + p_{recoil}$ at 190 GeV$/c$, Phys. Rev. D95 (3) (2017) 032004. (Cited in Sec. 5.2.3.)

[103] S. Paul, The spectrum of light isovector mesons with $C = +1$ from the COMPASS experiment, in: Proceedings of the 14th International Conference on Meson-Nucleon Physics and the Structure of the Nucleon (MENU2016), Journal of the Physical Society of Japan, 2017. (Cited in Sec. 5.2.3.)

[104] F. Krinner, Light-Meson Spectroscopy at Compass, EPJ Web of Conferences 137 (2017) 05012. (Cited in Sec. 5.2.3.)

[105] P. Abbon, et al., The COMPASS Setup for Physics with Hadron Beams, Nucl. Instr. Meth. A 779 (2015) 69–115. (Cited in Sec. 2.)

[106] D. M. Asner, et al., Resonance structure of $\tau^- \to K^-\pi^+\pi^-\nu_\tau$ decays, Physical Review D - Particles, Fields, Gravitation and Cosmology 62 (2000) 1–11. (Cited in Sec. 5.2.5.)

[107] D. Epifanov, et al., Study of $\tau^- \to K_S\pi^-\nu_\tau$ decay at Belle, Physics Letters B 654 (3-4) (2007) 65–73. (Cited in Sec. 5.2.5.)

[108] J. Link, et al., Dalitz plot analysis of the $D^+ \to K^-\pi^+\pi^+$ decay in the FOCUS experiment, Physics Letters B 653 (1) (2007) 1–11. (Cited in Sec. 5.2.5.)

[109] R. Aaij, et al., Studies of the resonance structure in $D^0 \to K^0_S K^\pm \pi^\pm$ decays, Physical Review D 93 (5) (2016) 052018. (Cited in Sec. 5.2.5.)

[110] M. Dugger, et al., A study of meson and baryon decays to strange final states with GlueX in Hall D (2012) 1–20.
URL http://www.gluex.org/docs/pac38_proposal.pdf (Cited in Sec. 5.2.5.)

[111] G. Amaryan, M. J. anothers, Strange Hadron Spectroscopy with a Secondary K_L Beam at GlueX .
URL http://arxiv.org/abs/1707.05284 (Cited in Sec. 5.2.5.)

[112] H. Fujioka, et al., Extension of the J-PARC Hadron Experimental Facility - summary report - , Committee for the study of the extension of the Hadron Experimental Facility (2017) 1–22. (Cited in Sec. 5.2.5.)

[113] C. D. Roberts, priv. communication . (Cited in Sec. 31.)

[114] J. Badier, et al., Measurement of the K^-/π^- Structure Function Ratio Using the Drell-Yan Process, Phys. Lett. B93 (1980) 354–356. (Cited in Sec. 5.3.2.)

[115] J. T. Londergan, G. Q. Liu, A. W. Thomas, Kaon - nucleus Drell-Yan processes and kaon structure functions, Phys. Lett. B380 (1996) 393–398. (Cited in Sec. 5.3.3.)

[116] K. Park, Measurement of Kaon Structure Function through Tagged Deep Inelastic Scattering (TDIS), JLAB proposal C12-15-006A . (Cited in Sec. 5.3.5.)

[117] C. D. Roberts, Perspective on the origin of hadron masses, Few-Body Systems 58 (2017) 5. (Cited in Sec. 5.4.1.)

[118] J.-H. Zhang, J.-W. Chen, X. Ji, L. Jin, H.-W. Lin, Pion Distribution Amplitude from Lattice QCD, Phys. Rev. D95 (9) (2017) 094514. (Not cited.)

[119] A. Abdel-Rehim, et al., Nucleon and pion structure with lattice QCD simulations at physical value of the pion mass, Phys. Rev. D92 (11) (2015) 114513, [Erratum: Phys. Rev.D93,no.3,039904(2016)]. (Not cited.)

[120] W. Detmold, W. Melnitchouk, A. W. Thomas, Parton distribution functions in the pion from lattice QCD, Phys. Rev. D68 (2003) 034025. (Not cited.)

[121] R. Horsley, R. Millo, Y. Nakamura, H. Perlt, D. Pleiter, P. E. L. Rakow, G. Schierholz, A. Schiller, F. Winter, J. M. Zanotti, A Lattice Study of the Glue in the Nucleon, Phys. Lett. B714 (2012) 312–316. (Not cited.)

[122] R. M. Davidson, E. Ruiz Arriola, Parton distributions functions of pion, kaon and eta pseudoscalar mesons in the NJL model, Acta Phys. Polon. B33 (2002) 1791–1808. (Not cited.)

[123] C. Avila, J. C. Sanabria, J. Magnin, Pion and kaon parton distribution functions in a meson cloud model, Phys. Rev. D67 (2003) 034022, [Erratum: Phys. Rev.D68,079902(2003)]. (Not cited.)

[124] A. Batunin, A. Likhoded, V. Kiselev, Are the gluon distributions different in π and K-mesons?, Report IFVE-OTF–88-67 (1988). (Not cited.)

[125] P. Aurenche, R. Baier, M. Fontannaz, D. Schiff, Prompt Photon Production at Large p(T) Scheme Invariant QCD Predictions and Comparison with Experiment, Nucl. Phys. B297 (1988) 661–696. (Cited in Sec. 5.4.1.)

[126] A. Hanks, Measurements of Fragmentation Photons with the PHENIX Detector, Nucl. Phys. A830 (2009) 455C–458C. (Cited in Sec. 5.4.2.)

[127] G. Alverson, et al., Production of direct photons and neutral mesons at large transverse momenta by π^- and p beams at 500-GeV/c, Phys. Rev. D48 (1993) 5–28. (Cited in Sec. 5.4.2.)

[128] W. Vogelsang, M. R. Whalley, A Compilation of data on single and double prompt photon production in hadron hadron interactions, J. Phys. G23 (1997) A1–A69. (Cited in Sec. 5.4.3.)

[129] J. Gasser, M. A. Ivanov, M. E. Sainio, Revisiting gamma gamma —¿ pi+ pi- at low energies, Nucl. Phys. B745 (2006) 84–108. (Cited in Sec. 5.5.1.)

[130] F. Guerrero, J. Prades, Kaon polarizabilities in chiral perturbation theory, Phys. Lett. B405 (1997) 341–346. (Cited in Sec. 5.5.1.)

[131] M. A. Ivanov, T. Mizutani, Pion and kaon polarizabilities in the quark confinement model, Phys. Rev. D45 (1992) 1580–1601. (Cited in Sec. 5.5.1.)

[132] B. Pasquini, D. Drechsel, S. Scherer, Pion polarizabilities: No conflict between dispersion theory and ChPT, PoS CD09 (2009) 037. (Cited in Sec. 5.5.1.)

[133] G. Backenstoss, et al., K- mass and k- polarizability from kaonic atoms, Phys. Lett. 43B (1973) 431–436. (Cited in Sec. 5.5.1.)

[134] Y. Bai, M. Bodlak, V. Frolov, V. Jary, S. Huber, I. Konorov, D. Levit, J. Novy, D. Steffen, M. Virius, Overview and future developments of the fpga-based daq of compass, Journal of Instrumentation 11 (02) C02025. (Cited in Sec. 6.1.1.)

[135] D. Gaisbauer, Y. Bai, S. Huber, I. Konorov, D. Levit, S. Paul, D. Steffen, Unified communication framework, Real Time Conference (RT), 2016 IEEE-NPSS . (Cited in Sec. 6.1.1.)

[136] Status and characterisation of compass rich-1, Nuclear Instruments and Methods in Physics Research Section A: Accelerators, Spectrometers, Detectors and Associated Equipment 553 (1) (2005) 215 – 219, proceedings of the fifth International Workshop on Ring Imaging Detectors. (Cited in Sec. 6.1.5.)

[137] Read-out electronics for fast photon detection with compass rich-1, Nuclear Instruments and Methods in Physics Research Section A: Accelerators, Spectrometers, Detectors and Associated Equipment 587 (2) (2008) 371 – 387. (Cited in Sec. 6.1.5.)

[138] P. Abbon, M. Alexeev, H. Angerer, R. Birsa, P. Bordalo, et al., Design and construction of the fast photon detection system for COMPASS RICH-1, Nucl. Instr. Meth. A 616 (2010) 21–37. (Cited in Sec. 6.1.5.)

[139] P. Abbon, M. Alexeev, H. Angerer, G. Baum, R. Birsa, et al., Particle identification with COMPASS RICH-1, Nucl. Instr. Meth. A 631 (2011) 26–39. (Cited in Sec. 6.1.5.)

[140] B. Dey, M. Borsato, N. Arnaud, D. W. G. S. Leith, K. Nishimura, D. A. Roberts, B. N. Ratcliff, G. Varner, J. Va'vra, Design and performance of the Focusing DIRC detector, Nucl. Instrum. Meth. A775 (2015) 112–131. (Cited in Sec. 6.1.5.)

[141] Prototype tests for a dirc detector for the wasa-at-cosy experiment, Nuclear Instruments and Methods in Physics Research Section A: Accelerators, Spectrometers, Detectors and Associated Equipment 639 (1) (2011) 185 – 189, proceedings of the Seventh International Workshop on Ring Imaging Cherenkov Detectors. (Cited in Sec. 6.1.5.)

[142] A. Papanestis, The LHCb RICH system; detector description and operation, Nucl. Instrum. Meth. A766 (2014) 14–18. (Not cited.)

[143] T. C. Collaboration, Proposal . (Not cited.)

[144] M. Blatnik, et al., Performance of a Quintuple-GEM Based RICH Detector Prototype, IEEE Trans. Nucl. Sci. 62 (6) (2015) 3256–3264. (Not cited.)

[145] M. Antonova, et al., Baby MIND: A Magnetised Spectrometer for the WAGASCI Experiment, in: Proceedings, Prospects in Neutrino Physics (NuPhys2016): London, UK, December 12-14, 2016. (Cited in Sec. 6.2.1.)

[146] K. N. Gusev, Y. B. Gurov, S. L. Katulina, V. N. Pavlov, V. G. Sandukovsky, A study of the performance characteristics of silicon and germanium semiconductor detectors at temperatures below 77 k, Instruments and Experimental Techniques 50 (2) (2007) 202–206. (Cited in Sec. 6.2.3.)

[147] M. Protsenko, Activities of ltu for high energy physics experiments, talk given at the DAQ/FEE/Trigger for COMPASS beyond 2020 workshop, November 9-11, 2017, Prague, Czech Republic.
URL https://indico.cern.ch/event/673073/contributions/2770450/attachments/1556738/2448475/DAQFEET_LTUProtsenko_2017Nov-11.pdf (Cited in Sec. 6.2.3.)